UNIVERSITÀ DEGLI STUDI DI MILANO

Scuola di Dottorato in Fisica, Astrofisica e Fisica Applicata
Dipartimento di Fisica

Corso di Dottorato in Fisica, Astrofisica e Fisica Applicata
Ciclo XXXIII

Critical phenomena
in
Random Dimer Models

Settore Scientifico Disciplinare FIS/02

Supervisore: Professor Sergio CARACCIOLO

Coordinatore: Professor Matteo PARIS

Tesi di Dottorato di:
Riccardo FABBRICATORE

Anno Accademico 2020/2021

Contents

Introduction

Why bother with critical models?

This thesis, as so many works by other physicists, is in a sense about the search for universal laws. After all, theory's purpose has never been to merely mimic the experimental results, but to give a deeper understanding, embedding them into a universal picture of nature.

Being raised by old-fashioned Russian field theorists, during my master I knew very well what every physicist should work on: Grand Unified Theory models, and if we value being taken seriously, they ought to be supersymmetric. Being a judicious student, I knew by hearth both graphs upon which the modern understanding of physics is based: the one where three lines intersect (at one single point, if seriousness is held in esteem) and the one with an ethnic hat. Being young and full of ideals, at the time I thought these concepts arose purely from the study of nature at incredible scales, where it shines the brightest, behaving in an intricate and yet simple way. As it turns out, Quantum Field Theory, the Standard Model, and what's beyond may be based on the very peculiar behaviour of nature at vanishing scales, but the struggle for a unified description of vastly different systems begun, unknowingly, more than a century and a half ago from the study of unsuspicious phenomena.

In the 1860s, while a picture of the atomic structure of matter was absent and physicists were still debating the existence of atoms, Thomas Andrews discovered a strange point in the pressure-temperature graphic of carbon dioxide, where the properties of the liquid and the vapour above it became indistinguishable and the new fluid became opalescent. It was the first time a critical point was observed. Van der Waals' doctoral thesis contained a first explanation of the phenomena based on the interactions between molecules that bear his name and showed that the difference between vapour and liquid's specific volume vanishes as a power of the temperature. Some thirty years after Andrews, Pierre Curie discovered the ferromagnetic-paramagnetic transition in iron and realized the similarity of the two phenomena, both governed by critical exponents. After forty years, in 1937, when the quantum mechanical description of matter was well understood, Lev Landau was the first one to propose a general framework that provided a unified explanation of these phenomena. His model gave a good qualitative description of the transitions in fluids and magnets, yielding the values of critical exponents. For the first time, the concepts of broken symmetry were used to justify different phases. Parallel to all this, in 1924 the first abstract model of a magnet, to put it as John Cardy said, "the one we have in the back of our minds", was formulated and solved in its one-dimensional variant by Ernst Ising. Some other ten years later, in 1947, Onsager's solution of the two-dimensional Ising model, in which there can be phase transitions, showed that Lev Landau's model is not quantitatively exact. Physicists started studying condensed matter models and in the early 60's several scaling relations among critical exponents were derived. A deeper understanding of the scaling importance came from Leo

Kadanoff's "block-spin" renormalization group. A general understanding was reached when the scaling ideas were reconsidered in the renormalization-group framework by Kenneth Wilson. Within this new framework, it was possible to explain the critical behaviour of most of the systems and their universal features. For instance, why fluids and uniaxial antiferromagnets behave quantitatively in an identical way at the critical point, despite having no apparent common Hamiltonian. Since then, critical phenomena have been the object of extensive studies and many new ideas have been developed in order to understand the critical behaviour of increasingly complex systems. The concepts that first appeared in condensed matter physics have been applied to different areas, such as high energy physics, where the whole "spontaneous symmetry breaking" mechanism is a cornerstone of the Standard Model and, as my education showed, the struggle for the reconstruction of broken symmetries drove physicists' imagination.

The traditional approach of theoreticians, going back to the formulation of quantum mechanics, is to consult Schrödinger's equation when a problem arises in atomic or solid-state physics. We define the Hamiltonian, hoping we have included everything relevant, then we make some approximations, or rather some pseudo-guesses, and then proceed to find for the energy levels, eigenstates and the rest. However, for truly complicated systems, this is a hopeless task.

One could argue that the task of the theorist is to understand what is going on and to elucidate which are the crucial features of the problem. Furthermore, we are met by a dilemma when dealing with many-body systems. Even if we had a large enough computer to solve Schrödinger's equation for the immense system, we would still have no understanding of the reasons behind the emerging behaviour. As Michael Fisher said: "A good theoretical model of a complex system should emphasize those features which are most important and should downplay the inessential details. Now the only snag with this advice is that one does not really know which are the inessential details until one has understood the phenomena under study." The rational consequence is the need to investigate the widest possible range of models and as I will try to prove to you, that even the simplest model of scattered points joined by lines can be analysed with incredibly sophisticated theories, yielding a stream of beautiful connections between vastly different mathematical concepts.

Critical Phenomena

1.1 Introduction

1.1.1 A first encounter

The theory of Critical Phenomena is a great endeavour which started more than a century ago and has seen active discovery up to very recent years. In the 1860s Thomas Andrews carried out experiments with carbon dioxide Andrews (1869). Imagine a sealed transparent tube containing CO_2 at an overall density of about 0.5 g/cm^2 and a pressure of about 72 atm. When heated at 29°C it exhibits a sharp meniscus separating liquid from vapour. We can follow the behaviour of liquid and vapour densities inserting two solid spheres of densities slightly above and below 0.48 g/cm^2 respectively. In this state, the spheres are both lying on the meniscus, floating onto the liquid. If we heat the system to 30°C, the two objects will separate, the lighter will float up to the top of the tube, while the heavier will sink to the bottom. This can only mean that the densities of the two phases have become incredibly close one to another, but the meniscus is still visible, meaning that there still is a difference between them. At 31°C we start seeing fog inside the tube, a phenomenon known as *Critical Opalescence*. An attentive observer will notice how its colour changes, depending on where the light source is: bluish if viewed from a direction normal to the illumination, reddish if illuminated from behind. Finally, if we heat a bit more, all differences between the two phases disappear, leaving a transparent homogeneous fluid at all temperatures above $T_c \simeq 31.04$°C.

If we were to sketch the system's state on a pressure-temperature phase diagram as in 1.1, we could draw curves separating different phases. The discussed phenomena will be at points a, b and c. At (T_c, p_c), the so called *Critical Point*, we will have critical opalescence, the two densities ρ_{liq} and ρ_{vap} will match and the vapour pressure curve will terminate. The fact that it terminates means that one can convert a liquid to a gas continuously, without crossing the phase transition line, as is indicated by the dotted path. In this sense, there is no fundamental difference between the liquid and gaseous phases. This is clearly portrayed in a density-temperature phase diagram 1.2, where the two phases merge at T_c. It has been found out that this behaviour is not peculiar only to carbon dioxide, but it's also present in gasses such as argon, krypton, nitrogen, oxygen, etc. If for each gas we normalize their pressure and temperature by their critical values T_c and ρ_c, we will get curves on the density-temperature plane that nearly fit the same values, as shown in fig. 1.3. The existence of a quantity $\rho_{liq} - \rho_{vap}$, which is non-zero below the critical temperature and zero above it, is a common feature associated with the critical points of a variety of physical systems and Its dependence on T is one of the focuses of the theory of critical phenomena.

The previous attentive observer would have pointed out that the dependence of the tinge from light's angle is similar to how the atmosphere behaves under the sun's light.
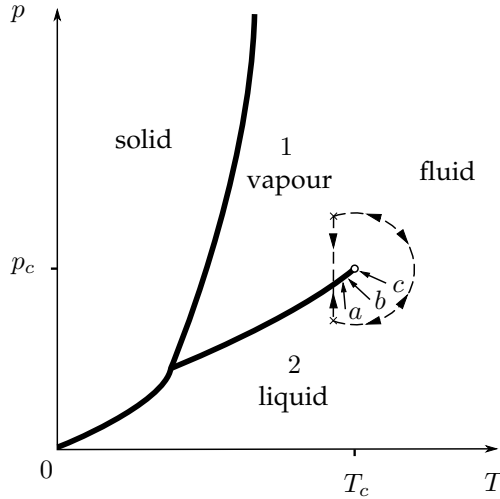
Figure 1.1: $P - T$ phase portrait for Carbon Dioxide. a, b, c are the three points described above

The colour of the sky was shown by A. Einstein (1910) to be caused by Rayleigh scattering on the small particles in the atmosphere, scattering light with intensity $\sim \lambda^{-4}$. This gives us the bluish tinge if we observe from a direction normal to the one of the source, where scattering is prominent, otherwise shifting towards the red simply because shorter wavelengths dissipate faster. We will explain the connection with critical opalescence after introducing some useful concepts.

A first explanation of the critical behaviour can be found in van der Waals' doctoral thesis van der Waals (1873). Van der Waals equation of state can be written in terms of critical temperature, pressure and volume introducing

$$\mathbf{T} = \frac{T}{T_c}, \quad \mathbf{p} = \frac{p}{p_c}, \quad \mathbf{V} = \frac{V}{V_c}. \tag{1.1}$$

We can then write a "universal" equation, independent of the nature of the fluid being considered.

$$\left(\mathbf{p} + \frac{3}{\mathbf{V}^2}\right)\left(\mathbf{V} - \frac{1}{3}\right) = \frac{8}{3}\mathbf{T} \tag{1.2}$$

It follows that for T close enough to T_c, the difference between the gas's and the liquid's specific volume vanishes as a power of $|T - T_c|$

$$V_{liq} - V_{vap} = |T - T_c|^\beta \tag{1.3}$$

From the van der Waals equation we can get that $\beta = 1/2$. Experimentally, it has been observed that this exponent is closer to $1/3$ than to $1/2$. As said before, the value of this exponent is apparently the same for several different fluids as can be seen in figure 1.3 .

1.1.2 A striking analogy

The profundity of this relation goes beyond its application to gasses, as it was noted by Pierre Curie Curie (1895) when he discovered the ferromagnetic transition in iron at the critical (Curie after him) point. At any $T < T_c$, the magnet has a *magnetization* **M** that one
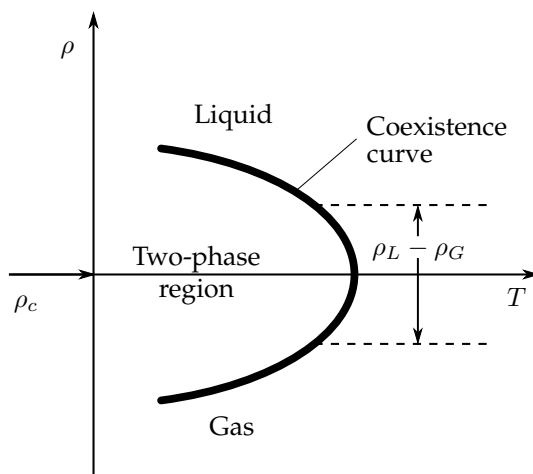
Figure 1.2: $\rho - T$ diagram

can temper with if one applies a strong enough *external magnetic field* **H**, spending some energy to bring the system to a new state **M**′, following the hysteresis curve. At $T \sim T_c$ the magnetization vanishes and so does the hysteresis, meaning one can exert a very weak external magnetic field **H** and then cool the magnet to reach a new magnetization, effectively going around the critical point as we did for gasses. Above T_c all the phases coexist since thermal fluctuations are strong enough to bring the system to ergodicity. If we had to draw an analogy between gasses and magnets, we could argue that overall magnetization **H** needs to be the analogue of pressure p, and the $H - T$ phase portrait has a curve analogous to the one in $P - T$. The quantity, which vanishes at T_c is the magnetization **M**. Fig 1.4 shows how far this analogy can be taken.

There is one difference though. In this case, we are dealing with vector fields and solids instead of scalars and fluids and this actually helps us understand what's happening. The overall magnetization is just the sum of a solid's constituents' magnetization vectors in quantum as in classical theory and for simplicity, we will use the term spin for these vectors. The phases of a magnet differ only because of the prevailing direction of their spins' alignment, and heating makes the latter randomly fluctuate. According to Landau's classification, in fact, phase transitions, in general, are a result of a change in symmetry. When we transition from above T_c to below, we pass from a symmetry group G to a subgroup $G' \subset G$, thus restricting the freedom and bringing some *order*. In the case of magnets, it's simpler to portray the symmetries Landau et al. (1980). Both $\Delta\rho$ and **M** differ from zero only below T_c, thus signalling the presence of order in the system, hence they are called *order parameters*.
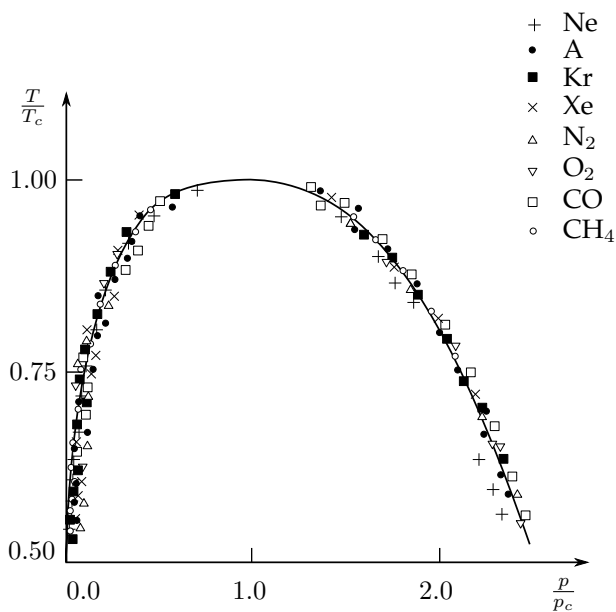
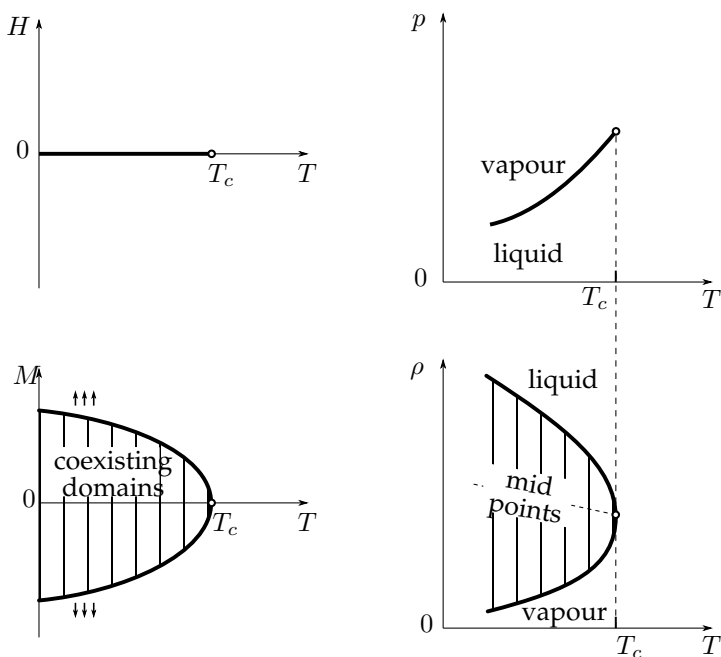**Figure 1.3:** The universal behaviour of fluids following van der Waals' equation is confirmed experimentally

Figure 1.4: The analogy between ferromagnets and gasses is clearly visible in phase portraits

1.2 Order parameters

As we have seen, the order in the system is responsible for its phases. This description is more natural in magnets and we will focus on them hoping to get greater insights on critical phenomena in general, given the broad analogies discovered so far. We can try quantifying the order of our system by introducing an order parameter as we just saw. A non-zero value of the order parameter will correspond to the breaking of a symmetry. In our magnetic example, the broken symmetry is the symmetry under rotations and the order parameter is the magnetization vector **M**. In the high-temperature phase the system is invariant under rotations around all three axes. We can intuitively imagine how spins randomly point in all directions and rotating all of them around a given axis will still yield randomly pointing spins. When **M** is non-zero, in the low-temperature phase, the symmetry breaks to a smaller one: it remains invariant only under rotations around one axis, namely that of **M**. Following Landau we will distinguish phase transitions by the behaviour of the order parameter. In phase portrays like 1.2, the phase transitions away from critical points are followed by a discontinuity of the order parameter. These are phase transitions of the *first order*. At critical points however, the order parameter is a continuous function of the temperature and the discontinuity is in its slope. This is what distinguishes the two phenomena, and the latter will be called phase transition of the *second order*.

Having established all of this, it becomes clear that to understand phase transitions and the peculiar behaviour of systems at critical point, it will be wise to investigate order parameters. If we assume the parameter to be an enough smooth function of the temperature, then we can expand it around T_c. Naming $t = \frac{T-T_c}{T_c}$, if the limit

$$\lim_{t \to 0+} \frac{\ln f(t)}{\ln t} = \lambda. \tag{1.4}$$

exists, then we say that λ is the *critical exponent* of that function and we write $f(x) \sim x^\lambda$ as a shorthand meaning that near T_c the function can be approximated as a power law with exponent λ. It does not mean that $f(t) = Ax^\lambda$, in fact, in general, we find that there are correction terms and the full expansion reads

$$f(x) = Ax^\lambda(1 + Bx^y + ...), \quad y > 0. \tag{1.5}$$

Nonetheless, in the proximity of the critical point, the behaviour of the leading terms dominates as is experimentally observed by log-log plots of the parameters. The slope of this straight-line region is all we need to know:

$$\Delta\rho \sim (T - T_c)^\beta, \text{ as } T \to T_c \tag{1.6}$$

$$\mathbf{M} \sim (T - T_c)^{\beta'}, \text{ as } T \to T_c \tag{1.7}$$

The order parameter is not the only observable we can take. Let's say we define the *Helmholtz free energy* for our magnet:

$$dF(T, M) = -SdT - MdH. \tag{1.8}$$

Then we can define quantities such as the *specific heat* C, our usual magnetization M or the *magnetic susceptibility* χ :

$$C = -T\frac{\partial^2 F}{\partial T^2}, \quad M = -\frac{\partial F}{\partial H}, \quad \chi = \frac{\partial M}{\partial H}. \tag{1.9}$$
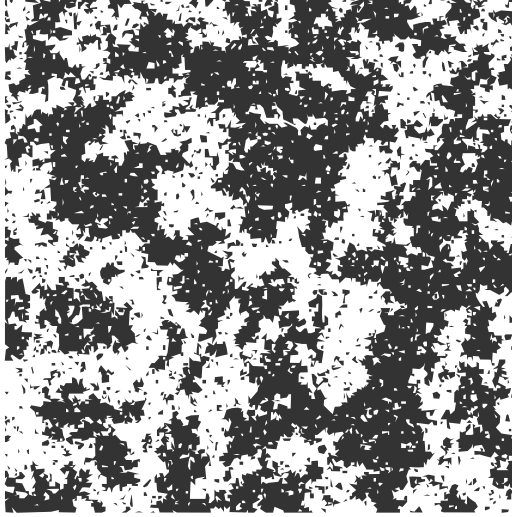
Figure 1.5: Kadanoff's droplet picture. A ferromagnet at T_c exhibits droplets of aligned spins inside other droplets in a fractal way.

All these quantities behave as power laws near the critical point, with critical exponents

$$C \sim |T - Tc|^{-\alpha}, \quad H = 0 \tag{1.10}$$

$$M \sim (T_c - T)^{\beta}, \quad T \leq T_c, H = 0 \tag{1.11}$$

$$\chi \sim |T - Tc|^{-\gamma}, \quad H = 0 \tag{1.12}$$

Furthermore, we can introduce a two-point correlation function as

$$G(r) = G(i, j) = \langle \sigma_i \sigma_j \rangle - \langle \sigma_i \rangle \langle \sigma_j \rangle \tag{1.13}$$

where σ_i is the local value of the magnetization, or spin, and $\langle . \rangle$ is the mean value over all the system, then away from criticality and at large distances, it will behave as

$$G(r) \sim r^{-\tau} e^{-r/\xi}, \quad T \neq T_c, H = 0. \tag{1.14}$$

$\xi = \xi(T, H)$ is the so called *correlation length*. At critical temperature, the system can fluctuate between the slightly more ordered phase and the slightly less since for a phase transition of the second-order there is no discontinuity. This means that small fluctuations will lead to the appearance of locally ordered regions, which will have an extension of the order of the correlation length ξ. As we have seen with carbon dioxide, the emergence of opalescence means that density fluctuations extend for a length comparable with the wavelength of light $\lambda \sim \xi$. The same phenomenon appears in magnets, if we were to take a picture of the magnet's local magnetization, we would see the so-called Kadanoff's droplet picture 1.5 . In other words, the correlation length diverges at the critical point and its behaviour is described by the exponent

$$\xi \sim |T - Tc|^{-\nu}, \quad H = 0. \tag{1.15}$$

This means correlations appear at all lengths, and the droplets actually ought to have a fractal structure. The whole correlation function at large distances behaves as

$$G(r) \sim r^{-d+2-\nu}, \quad T = T_c, H = 0. \tag{1.16}$$

which is a power law instead of an exponential decay.

What is remarkable is that such behaviour, though singular, has some very simple characteristics. The critical exponents do not assume just any values. Different systems, undergoing the most varied kinds of transitions, can be assigned to a small number of classes, each specified by a certain set of values of the exponents. Moreover one observes between the critical exponents some very simple relations like $\alpha + 2\beta + \gamma = 2$ called scaling laws, whose degree of universality is even greater.

1.3   Scaling and Universality

Let's take a step back. The divergence of the correlation length creating the beautiful fractal structure of the droplet picture seems to be the signature of criticality. As we have seen, near the critical point the range of correlations greatly increases and all the details of the local iterations in the system become unimportant to the long-wavelength behavior of the fluctuations measured by G. This gives us some insight about the remarkable universality we noticed. Clearly, the only important differences between different fluids can be found in the shapes and short range interactions of their constituent molecules. Near the critical point, fluctuations are taking place on the scale beyond any intermolecular distance, so the differences are averaged over. We can understand in an intuitive way that universality is a consequence of the fact that the correlation length becomes very large so that triggers the emergence of effective interactions, which no longer take place on an atomic scale but rather on a semi-macroscopic scale set by G. On this level, the microscopic differences do not matter and one obtains universality. As systems move away from criticality and the correlation length becomes smaller, the differences start to matter.

Now that we have established this picture, let's see how it can be used to derive information about the critical parameters and their exponents. All our functions depend on T and H which differ for every system. To render their form universal, let's use the reduced variables $t = \frac{T-T_c}{T_c}$ and $h = \frac{H}{k_B T_c}$, where k_B is the Boltzmann constant. We previously saw how to define correlation functions. For the critical parameter density $\sigma(\mathbf{r})$ and the energy density $\varepsilon(\mathbf{r})$, the two-point functions read:

$$G_\sigma(\mathbf{r_1} - \mathbf{r_2}) = \langle \sigma(\mathbf{r_1})\sigma(\mathbf{r_2}) \rangle - \langle \sigma(\mathbf{r_1}) \rangle \langle \sigma(\mathbf{r_2}) \rangle \tag{1.17}$$

$$G_\varepsilon(\mathbf{r_1} - \mathbf{r_2}) = \langle \varepsilon(\mathbf{r_1})\varepsilon(\mathbf{r_2}) \rangle - \langle \varepsilon(\mathbf{r_1}) \rangle \langle \varepsilon(\mathbf{r_2}) \rangle \tag{1.18}$$

Where we have already used knowledge from our picture to impose translation invariance, which holds for distances $a \ll r \ll \xi$. Let's now apply the scale invariance implied by the fractal picture:

$$G_\sigma(\mathbf{r}; t, h) = b^{-2x_\sigma} G_\sigma(\mathbf{r}/b; tb^{y_t}, hb^{y_h}) \tag{1.19}$$

$$G_\varepsilon(\mathbf{r}; t, h) = b^{-2x_\varepsilon} G_\sigma(\mathbf{r}/b; tb^{y_t}, hb^{y_h}) \tag{1.20}$$

This is the general form of a homogeneous function and the ansatz is known in literature as *scaling hypothesis*. In this way, at the critical point $t, h = 0$, our correlators are covariant under scale transformations. The exponents x_σ and x_ε are the so-called *scaling exponents*

for the *scaling operators* σ and ε, a hint that these observables are often studied in a quantum picture. The variables h and t are known as *scaling fields* conjugated to σ and ε. Each has its own exponent y_σ and y_ε. These correlators are related to the susceptibility and specific heat through the fluctuation-dissipation theorems:

$$\chi = \frac{1}{T} \sum_r G_\sigma\,(\mathbf{r}) \approx \frac{1}{T} \int G_\sigma\,(\mathbf{r})\,d^d\mathbf{r} \tag{1.21}$$

$$C = \frac{1}{T^2} \sum_r G_\varepsilon\,(\mathbf{r}) \approx \frac{1}{T^2} \int G_\varepsilon\,(\mathbf{r})\,d^d\mathbf{r} \tag{1.22}$$

Integrating, we get the scaling of the susceptibility per site

$$\chi\,(t,h) = b^{d-2x_\sigma} \chi\,(tb^{y_t}, hb^{y_h}) \tag{1.23}$$

As we previously saw, this quantity is related to the *free energy density* $f = F/N$ by $\chi = -\partial^2 f/\partial h^2$. Therefore, integrating twice with respect to h, we arrive at the scaling of the free energy density

$$f(t,h) = b^{d-2x_\sigma-2y_h} f\,(tb^{y_t}, hb^{y_h}) \tag{1.24}$$

The same can be done for the specific heat, since $C = -\partial^2 f/\partial t^2$ to obtain

$$f(t,h) = b^{d-2x_\varepsilon-2y_t} f\,(tb^{y_t}, hb^{y_h}) \tag{1.25}$$

Comparing the two results gives us a relation between the scaling exponents: $x_\sigma + y_h = x_\varepsilon + y_t$. A similar relationship in the scaling of the free energy could be derived for any pair of scaling operators coupled to their conjugate scaling fields. Since the free energy should scale simply as

$$f(t,h) = b^{-d} f\,(tb^{y_t}, hb^{y_h}), \tag{1.26}$$

where the factor b^{-d} results simply from the fact that the number of sites N which appears in the definition of f is reduced by a factor b^{-d}. We can see how $x_a + y_b = d$ for all the conjugate operators and fields a and b. We can perform the rescaling multiple times, getting

$$f(t,h) = b^{-nd} f\,(tb^{ny_t}, hb^{ny_h}). \tag{1.27}$$

The dilatation factor can be eliminated by fixing $b^{y_t} t = K$, obtaining

$$f(t,h) = K^{-d/y_t} t^{d/y_t} f\left(K, K^{-y_h/y_t} t^{y_h/y_t} h\right), \tag{1.28}$$

or

$$f(t,h) = \left|\frac{t}{t_0}\right|^{d/y_t} W_\pm\left(\left(\frac{h}{h_0}\right)\left(\frac{t}{t_0}\right)^{-y_h/y_t}\right) \tag{1.29}$$

Where $W_\pm$ are universal homogeneous functions and the index $\pm$ refers to $t > 0$ or $t < 0$ respectively. From here we can easily recover the critical exponents, in fact

$$C = -\partial^2 f/\partial t^2 \sim |t|^{d/y_t-2} \tag{1.30}$$

Hence, $\alpha = 2 - d/y_t$. The exponents β and γ are found analogously from $M = -\partial f/\partial h$ and $\chi = -\partial^2 f/\partial h^2$, yielding

$$\alpha = 2 - d/y_t \tag{1.31}$$

$$\beta = (d - y_h)/y_t \tag{1.32}$$

$$\gamma = (2y_h - d)/y_t \tag{1.33}$$

From where we can recover the previous remarkable relation between critical exponents!

$$\alpha + 2\beta + \gamma = 2. \tag{1.34}$$

If we eliminate in the same way the scaling factor from the correlation function G_σ, we have

$$G_\sigma \sim t^{2x_\sigma/y_t}, \tag{1.35}$$

thus

$$\xi \sim t^{-1/y_t}, \quad h = 0. \tag{1.36}$$

which gives $\nu = 1/y_t$, while at $t \to 0$, $G_\sigma(r) \sim r^{-2x_\sigma}$, or $\eta = 2x_\sigma + 2 - d$. This can be combined with $\gamma = (d - 2x_\sigma)/y_t$ to find another relation:

$$\gamma = \nu(2 - \eta). \tag{1.37}$$

As we saw, imposing translation invariance and scaling covariance allowed us to find the remarkable relations between critical exponents that were mentioned in the previous paragraph. Scale covariance seems to be the footprint of criticality and we are going to see how it can be obtained from general assumptions.

1.4　The renormalization group argument

Although our previous scaling hypothesis was sound, it was motivated by ad hoc reasoning over the phenomenological behaviour of magnets at critical temperature, with the fractal droplet picture given by fluctuations of the symmetry. We can actually construct a more general line of reasoning from basic elements. In order to establish a general formalism, we need to introduce some objects defined for a vast class of systems. For every system, we can introduce a Hamiltonian, or at least we can try to guess one. For our magnets let's consider a Hamiltonian $H[\sigma; t, h]$. Let's now say our spin variables σ_i are located on the sites i of a regular grid, divided into cells each of a volume $b \times b \times ... \times b = b^d$, where b is the spacing between them. Each cell contains a number of spins. Now let's average on them to find a new *block spin*, leading to a new Hamiltonian $H[\sigma'; t', h']$, where in general the couplings t, h are also transformed. This will lead to the creation of interactions between the new block spins which are not present in the original Hamiltonian. We can neglect this for now since we are not trying to obtain the whole picture. Now let's consider the case at critical temperature $t = 0$ and perform a scale transformation or *dilatation*.

$$\mathbf{r} \to \mathbf{r}' = \mathbf{r}/b \tag{1.38}$$
$$h \to h' = hb^y \tag{1.39}$$

Now the mean value of σ can be found knowing the Hamiltonian simply by the partition function defined as

$$Z = \sum_{\{\sigma\}} \exp\left(\frac{1}{T}H\right) \tag{1.40}$$

Since h is conjugate to the spin σ, the mean value is

$$
\begin{aligned}
\langle \sigma(\mathbf{r}) \rangle =& \frac{1}{NZ} \frac{\partial Z}{\partial h(\mathbf{r})} \\
=& \frac{1}{N} \frac{1}{Z'} \frac{\partial Z'}{\partial h(\mathbf{r})} \\
=& \frac{1}{N' b^d} \frac{1}{Z'} \frac{\partial h'(r')}{\partial h(r)} \frac{\partial Z'}{\partial h'(\mathbf{r}')} \\
=& b^{y-d} \langle \sigma'(\mathbf{r}') \rangle
\end{aligned}
\tag{1.41}
$$

We can now define the scaling dimension of the spin operator as $x_\sigma = y - d$ and write

$$
\langle \sigma(\mathbf{r}) \rangle_h = b^{-x_\sigma} \langle \sigma'(\mathbf{r}') \rangle_{h'}
\tag{1.42}
$$

The spin correlation function inherits the same factors:

$$
G_\sigma (\mathbf{r}_1 - \mathbf{r}_2) = \langle \sigma(\mathbf{r}_1) \sigma(\mathbf{r}_2) \rangle = \frac{1}{N^2 Z} \frac{\partial^2 Z}{\partial h(\mathbf{r}_1) \partial h(\mathbf{r}_2)}
\tag{1.43}
$$

and therefore

$$
G(\mathbf{r}) = b^{-2x_\sigma} G(\mathbf{r}').
\tag{1.44}
$$

Other correlators can be treated similarly.

We see how for each scaling operator ϕ, the scaling dimension is

$$
x_\phi = d - y_\phi
\tag{1.45}
$$

and we retrieve the conjugation between the scaling operator and the scaling field. This ideas are the basis of what is known as *Renormalization Group*. One last important observation we can make about this technique, is that the introduced scaling exponents for fields and conjugated operators lead to a sharp distinction between them. As we proceed with the rescaling, averaging over more and more spins, some operators are greatly enhanced by their prefactor b^{nx_ϕ} and others are dumped, depending on the sign of the exponent. This reflects the very same idea about correlations at criticality that we wanted to implement. At criticality, when the fields are equal to zero, any small perturbation will be greatly enhanced, leading the system away from criticality, or greatly diminished, leading it towards criticality. This is a prescription to find which operators will be *relevant* to our new, renormalized, system and which are *irrelevant*, which is exactly what we wanted to find when we realized that at criticality information about local details will be lost by an averaging over a vast quantity of constituents. For further information on this important subject, we strongly recommend the historical review by the very same Wilson (1975) as well as texts such as Fisher (1983) or books Stanley (1987), Pfeuty and Toulouse (1976) or Uzunov (1993).

We have thus seen that scale invariance, as implemented by the renormalization group, yields relations between the critical exponents, but without fixing their numerical value. In addition, the correlation functions transform covariantly under a dilatation, at the critical point. One cannot help but wonder if we have guessed the right symmetry to impose and what will happen if we change it. After all, symmetry is the muse of physicists.

Conformal Field Theory

In the last chapter, we were able to derive part of the phenomenology of systems at the critical point by imposing scale invariance (covariance to be precise) on our microscopic observables. The correctness of the ansatz was verified a posteriori since the predictions seem to fit empirical observations. Of course, we have not proved the uniqueness of this assumption and it is natural to loosen them, generalizing the scale invariance to a broader symmetry. The following chapter is meant to be a concise introduction to how Conformal Field Theory can be used to obtain results about observables in critical systems, for further reading about this beautiful subject we recommend a few classical texts such as Di Francesco et al. (1997), Henkel (1999).

2.1 Scale and conformal invariance

Scale invariance is a *global symmetry*, meaning that every point of our space is acted on in the same way

$$\mathbf{r} \to a\mathbf{r}, \quad a = const > 0, \tag{2.1}$$

and the whole region we are acting on just dilate (or shrunk for $a < 1$). Any field theorist knows that things start getting interesting when we consider local symmetries. The self-similarity requirement we used in the previous chapter can be expressed as the requirement to maintain proportions, and thus angles. Although rescaling does the trick, in general, our requirement can be expressed as

$$dS^2(\mathbf{r}) \to dS'^2 = \Lambda(\mathbf{r})dS^2, \tag{2.2}$$

where $dS^2(\mathbf{r})$ is the interval defining the metric at point $\mathbf{r}$ for our space of arbitrary dimension. We see that if $\Lambda(\mathbf{r})$ is smooth enough, we can rescale differently at every point and still get a self similar picture. This self-similarity is called *conformal symmetry* , from Latin conformalis, meaning of the same form or shape. Intuitively the set of all such transformation is composed solely by dilatation and rotations (at least in 2d where intuition works). This set forms a group and it has the Poincaré group as a subgroup since the latter corresponds to the case $\Lambda(\mathbf{r}) \equiv 1$. Some examples of conformal transformations are shown in fig. 2.1. Steven Weinberg in the introduction of *"Gravitation and Cosmology"* famously asks if Middle Earth is flat. We can now say that although the mapping from the flat chart to the shape of the word is not a global rescaling (in which case flatness would be preserved), it is at least a locally conformal map.

Let's study how coordinates must transform in order to satisfy 2.2. We will denote as $g_{\mu\nu}(\mathbf{r})$ the metric tensor yielding the interval $dS^2(\mathbf{r}) = g_{\mu\nu}(\mathbf{r})d\mathbf{r}^\mu d\mathbf{r}^\nu$. Any infinitesimal
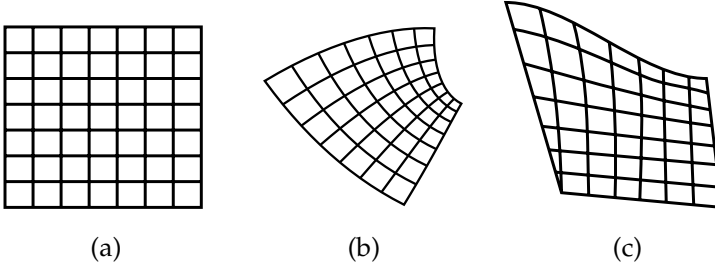
(a)   (b)   (c)

Figure 2.1: Coordinate transformations. The transformation from the square lattice in (a) onto the lattice in (b) is conformal, while the transformation onto the lattice in (c) is not because angles are not locally preserved.

transformation can be expressed as $\mathbf{r}^\mu \to \mathbf{r}'^\mu = \mathbf{r}^\mu + \epsilon^\mu(\mathbf{r})$ and the transformed metric can be written as a function of it:

$$
\begin{aligned}
g'_{\mu\nu} &= \frac{\partial \mathbf{r}^\alpha}{\partial \mathbf{r}'^\mu}\frac{\partial \mathbf{r}^\beta}{\partial \mathbf{r}'^\nu}g_{\alpha\beta} \\
&= (\delta_{\alpha\mu} - \partial_\mu \epsilon^\alpha)(\delta_{\beta\nu} - \partial_\nu \epsilon^\beta)g_{\alpha\beta}
\end{aligned}
$$

and thus neglecting terms $o(\partial\epsilon^2)$ we arrive at

$$
g_{\mu\nu} \to g_{\mu\nu} - (\partial_\mu \epsilon_\nu + \partial_\nu \epsilon_\mu) . \tag{2.3}
$$

To be a conformal transformation, the last term must still be of the form

$$
\partial_\mu \epsilon_\nu + \partial_\nu \epsilon_\mu = f(x)g_{\mu\nu} \tag{2.4}
$$

and we can obtain information of $f(x)$ by taking the trace of both sides:

$$
f(x) = \frac{2}{d}\partial_\rho \epsilon^\rho, \tag{2.5}
$$

where for simplicity we are supposing a flat d dimensional real space $\mathbb{R}^d$ with metric $\eta_{\mu\nu}$. Returning to 2.4 we can simplify the left-hand side by applying a derivative ∂_ρ, permuting indices and taking the linear combination in order to obtain

$$
2\partial_\mu \partial_\nu \epsilon_\rho = \eta_{\mu\rho}\partial_\nu f + \eta_{\nu\rho}\partial_\mu f - \eta_{\mu\nu}\partial_\rho f, \tag{2.6}
$$

which can be contracted with $\eta^{\mu\nu}$ to become

$$
2\partial^2 \epsilon_\mu = (2 - d)\partial_\mu f. \tag{2.7}
$$

If we now apply ∂_ν to this expression and ∂^2 to 2.2, we find

$$
(2 - d)\partial_\mu \partial_v f = \eta_{\mu\nu}\partial^2 f. \tag{2.8}
$$

Finally, after contracting with $\eta^{\mu\nu}$, we end up with

$$
(d - 1)\partial^2 f = 0. \tag{2.9}
$$

From these equations, we can derive the explicit form of conformal transformations in d dimensions. The two final equations impose that $\partial_\mu \partial_\nu f = 0$, meaning f is of the form

$$
f(x) = A + B_\mu x^\mu \quad (A, B_\mu \text{ constant}) \tag{2.10}
$$

thus $\partial_\mu \partial_\nu \epsilon_\rho$ is constant and so ϵ_μ is at most quadratic in the coordinates. We can therefore write the general expression

$$\epsilon_\mu = \mathbf{a}_\mu + b_{\mu\nu}\mathbf{r}^\nu + c_{\mu\nu\rho}\mathbf{r}^\nu\mathbf{r}^\rho \qquad c_{\mu\nu\rho} = c_{\mu\rho\nu}. \tag{2.11}$$

We can treat each power of the coordinate separately since 2.2 holds for all $\mathbf{r}$. This means $\mathbf{r}_\mu$ is free of constraints and it amounts for infinitesimal translation. The linear term behaves as

$$b_{\mu\nu} + b_{v\mu} = \frac{2}{d}b^\lambda_\lambda \eta_{\mu\nu} \tag{2.12}$$

Which implies that $b_\mu\nu$ is the sum of an anti-symmetric tensor and a pure trace:

$$b_{\mu\nu} = \alpha\eta_{\mu\nu} + m_{\mu\nu} \qquad m_{\mu\nu} = -m_{v\mu} \tag{2.13}$$

The pure trace part is responsible for infinitesimal scale transformations, whereas the anti-symmetric part is an infinitesimal rotation. The quadratic terms have the constraints

$$c_{\mu v\rho} = \eta_{\mu\rho}b_v + \eta_{\mu v}b_\rho - \eta_{v\rho}b_\mu \quad \text{where} \quad b_\mu \equiv \frac{1}{d}c^\sigma_{\sigma\mu} \tag{2.14}$$

and the corresponding infinitesimal transformation is

$$\mathbf{r}'^\mu = \mathbf{r}^\mu + 2(\mathbf{r}\cdot\mathbf{b})\mathbf{r}^\mu - \mathbf{b}^\mu\mathbf{r}^2, \tag{2.15}$$

which is known in literature as *special conformal transformation* (SCT). The finite transformations corresponding to the above are the following:

Translation	$r'^\mu = r^\mu + a^\mu$
Dilatation	$r'^\mu = \alpha r^\mu$
Rotation	$r'^\mu = M^\mu_v r^\nu$
SCT	$r'^\mu = \frac{r^\mu - b^\mu r^2}{1 - 2\mathbf{b}\cdot\mathbf{r} + b^2 r^2}$

The geometric meaning of the special transformation becomes clear when rewriting it as

$$\frac{x'}{x'^2} = \frac{x}{x^2} - b \tag{2.16}$$

Which is the combination of an inversion $\mathbf{r} \to \mathbf{r}' = \mathbf{r}/\mathbf{r}^2$ followed by a translation $-\mathbf{b}$ and again an inversion.

Since the transformations generate independent groups, we can write the generators for each one:

Translation	$P_\mu = -i\partial_\mu$
Dilatation	$D_\mu = -ix^\mu\partial_\mu$
Rotation	$L_{\mu\nu} = i(x_\mu\partial_\nu - x_\nu\partial_\mu)$
SCT	$K_\mu = -i(2x_\mu x^\nu\partial_\nu - x^2\partial_\mu)$

It is well known that in 2 dimensions *holomorphic functions* are conformal mappings. In 2 dimensions condition 2.2 becomes

$$\partial_1 \epsilon_1 = \partial_2 \epsilon_2 \qquad \partial_1 \epsilon_2 = -\partial_2 \epsilon_1. \tag{2.17}$$

If we define standard complex coordinates

$$\begin{aligned}
z &= x_1 + ix_2, \quad \bar{z} = x_1 - ix_2 \\
\epsilon(z) &= \epsilon_1 + i\epsilon_2, \quad \bar{\epsilon}(\bar{z}) = \epsilon_1 - i\epsilon_2
\end{aligned} \tag{2.18}$$

The conformal transformations we introduced are easily rewritten. A translation is $z \to z' = z+a$, a rotation by the angle α is $z \to z' = ze^{i\alpha}$ and a dilatation becomes $z \to z' = bz$, where α and b are both real. For the special transformations, let $a = a_1 - ia_2$ then we get

$$z' = \frac{z + \bar{a}z\bar{z}}{1 + \bar{a}\bar{z} + az + a\bar{a}z\bar{z}} = \frac{z(1 + \bar{a}\bar{z})}{(1+az)(1+\bar{a}\bar{z})} = \frac{z}{1+az} \tag{2.19}$$

The same expressions are obtained for the transformation of $\bar{z}$. Through the rest of our discussion, we will use this notation when working in a 2d space.

2.2   Conformal covariance of operators

Now that we have seen how the underlying space is transformed conformally, we can proceed to analyse the behaviour of correlation functions of operators such as ε or σ introduced in the previous chapter, when conformal covariance is requested. We remind that covariance under a global rescaling imposed on our correlators the form

$$\begin{aligned}
G_\sigma\left(\mathbf{r}; t, h\right) &= b^{-2x_\sigma} G_\sigma\left(\mathbf{r}/b; tb^{y_t}, hb^{y_h}\right) \\
G_\varepsilon\left(\mathbf{r}; t, h\right) &= b^{-2x_\varepsilon} G_\sigma\left(\mathbf{r}/b; tb^{y_t}, hb^{y_h}\right)
\end{aligned} \tag{2.20}$$

And the critical exponents are related by the equations

$$x_\sigma = d - y_h = \frac{\beta}{v}, \quad x_\varepsilon = d - y_\tau = \frac{1-\alpha}{v} \tag{2.21}$$

Now we will consider generic scaling operators $\phi_a(\mathbf{r})$ with the requirement of $\langle \phi_a(\mathbf{r}) \rangle = 0$ and study correlators $G_{ab}(\mathbf{r}_a, \mathbf{r}_b) = \langle \phi_a(\mathbf{r}_a)\phi_b(\mathbf{r}_b) \rangle$. If our previous rescaling factor b is now space dependent $b(\mathbf{r})$, a natural generalization of covariance is

$$\phi(\mathbf{r}) \mapsto \phi'(\mathbf{r}) = J(\mathbf{r})^{x_\phi/d} \phi(\mathbf{r}/b(\mathbf{r})) \tag{2.22}$$

where $J(x)$ is the Jacobian of the transformation $\mathbf{r} \to \mathbf{r}' = \mathbf{r}/b(\mathbf{r})$ and x_ϕ the scaling dimension of ϕ.

It will be helpful for us to redefine the mean value of an observable A in terms of a continuous probability distribution.

$$\langle A \rangle = \frac{1}{Z} \sum_{\{\sigma\}} A[\{\sigma\}] e^{-H[\{\sigma\}]/T} = \frac{1}{Z} \int D\phi A[\phi] e^{-S[\phi]} \tag{2.23}$$

Where $Z = \sum_{\{\sigma\}} e^{-H[\{\sigma\}]/T} = \int D\phi e^{-S[\phi]}$ is the partition function and $D\phi = \prod_x \int d\phi(x)$ is a shorthand for the functional integration. This can be done rigorously for instance by

a Hubbard-Stratonovich transformation, but intuitively can be thought of as a simple continuum limit without losing the physical meaning of the operation. A generic coordinate transformation will not be conformal, hence it will contain shear components which will drive the system away from its critical point, such that the action transforms as $S^*[\phi] \to S^*[\phi] + \delta S[\phi]$.

We impose that in general n point correlators transform covariantly if

$$\langle \phi_1'(\mathbf{r}_1) \dots \phi_n'(\mathbf{r}_n) \rangle_{S^*} = J(\mathbf{r}_1)^{x_1/d} \dots J(\mathbf{r}_n)^{x_n/d} \langle \phi_1(\mathbf{r}_1') \dots \phi_n(\mathbf{r}_n') \rangle_{S^*+\delta S} \tag{2.24}$$

Where S^* is the action at a fixed point, in our case the critical point. For the conformal invariance to hold, we need the variation to be zero:

$$\sum_{p=1}^{n} \langle \phi_1(\mathbf{r}_1) \dots \delta_{\text{total}} \phi_p(\mathbf{r}_p) \dots \phi_n(\mathbf{r}_n) \rangle = 0 \tag{2.25}$$

Where $\delta_{\text{total}} = \delta_1 + \delta_2$ is the sum of all variations induced by the coordinate change. From the Jacobian we get the variation for a single operator

$$\delta_1 \phi(\mathbf{r}) = \left(\frac{x_\phi}{d} \nabla \cdot \varepsilon(\mathbf{r}) + \varepsilon(\mathbf{r}) \cdot \nabla \right) \phi(\mathbf{r}) \tag{2.26}$$

Beside this, for an infinitesimal transformation $\mathbf{r}^\mu \to \mathbf{r}'^\mu = \mathbf{r}^\mu + \varepsilon^\mu(\mathbf{r})$, the variation of the action, up to the first order, can be written as

$$\delta_2 S = -\alpha \int d^d \mathbf{r} \, \partial^\mu \varepsilon^\nu(\mathbf{r}) T_{\mu\nu}(\mathbf{r}) \tag{2.27}$$

Where $T_{\mu\nu}$ is the *energy-momentum tensor*, i.e. the Noether current generating infinitesimal coordinate transformation. Variating the action affects mean values

$$\langle A \rangle_{S^*+\delta S} \simeq \frac{1}{Z} \int D\phi A[\phi](1 - \delta S[\phi]) e^{-S^*[\phi]} = \langle A(1 - \delta_2 S) \rangle_{S^*} \tag{2.28}$$

And so the total variation of an n point correlator can be written as

$$\sum_{p=1}^{n} \left\langle \phi_1(\mathbf{r}_1) \dots \left(\varepsilon(\mathbf{r}_p) \cdot \nabla + \frac{x_p}{d} \nabla \cdot \varepsilon(\mathbf{r}_p) \right) \phi_p(\mathbf{r}_p) \dots \phi_n(\mathbf{r}_n) \right\rangle$$

$$+ \alpha \int d\mathbf{r} \langle \phi_1(\mathbf{r}_1) \dots \phi_n(\mathbf{r}_n) T_{\mu\nu}(\mathbf{r}) \rangle \partial^\mu \varepsilon^\nu(\mathbf{r}) = 0 \tag{2.29}$$

This is the requirement that selects the operators in order to have conformal covariance. It is known in literature as *conformal Ward identity* and it's the fundamental equation for a confolmal field theory.

It turns out that in 2d the Ward identity can be expressed in a more compact form. Since we are dealing with holomorphic functions, we can use powerful tools such as Cauchy's integral formula. The second part of 2.29 simplified by Gauss' theorem to

$$\oint_{\partial D} \frac{dz}{2\pi i} \varepsilon(z) \langle T(z) \phi_1(z_1, \bar{z}_1) \dots \phi_n(z_n, \bar{z}_n) \rangle + \text{c.c} =$$

$$= \sum_{j=1}^{n} \oint_{C_j} \frac{dz}{2\pi i} \varepsilon(z) \langle T(z) \phi_1(z_1, \bar{z}_1) \dots \phi_n(z_n, \bar{z}_n) \rangle + \text{c.c.} \tag{2.30}$$

Where the integration was first performed on the boundary ∂D of a region, and subsequently substituted by small contours around singularities that can occur at $z = z_j$. We split the holomorphic and antiholomorphic parts since they turn out to be independent, and the same can be done for the first part of 2.29, which on the other hand can also be rewritten using Cauchy's formula

$$
\Delta \varepsilon'(z_1) \phi(z_1, \bar{z}_1) + \varepsilon(z_1) \partial \phi(z_1) =
$$
$$
= \frac{1}{2\pi i} \oint_{C_1} dz \varepsilon(z) \left(\frac{\Delta}{(z - z_1)^2} \phi(z_1, \bar{z}_1) + \frac{1}{z - z_1} \partial_{z_1} \phi(z_1, \bar{z}_1) \right), \tag{2.31}
$$

where $\Delta + \bar{\Delta} = x_\phi$, the scaling dimension of the operator ϕ.

Thus joining the two halves and discarding the integral over same contours, we obtain the *local conformal Ward identity*

$$
\langle T(z) \phi_1(z_1, \bar{z}_1) \ldots \phi_n(z_n, \bar{z}_n) \rangle
$$
$$
= \sum_{p=1}^{n} \left(\frac{\Delta_p}{(z - z_p)^2} + \frac{1}{z - z_p} \frac{\partial}{\partial z_p} \right) \langle \phi_1(z_1, \bar{z}_1) \ldots \phi_n(z_n, \bar{z}_n) \rangle. \tag{2.32}
$$

Clearly, an analogous form holds true for $\bar{T}(z)$, and can be obtained from the above expression by replacing $z \to \bar{z}$, $z_p \to \bar{z}_p$ and $\Delta_p \to \bar{\Delta}_p$.

The Ward identity shows the effects of a conformal transformation on operators in the group's representation. The transformation on $T(z)$ on itself can be interpreted as its two-point correlator $\langle T(z) T(z') \rangle$ and in the local form its value is

$$
T(z) T(z') =
$$
$$
= \frac{c/2}{(z - z')^4} + \frac{2}{(z - z')^2} T(z') + \frac{1}{z - z'} \frac{\partial}{\partial z'} T(z') + \text{ regular terms} \tag{2.33}
$$

The constant c will turn put to be the most important information we need to characterise a conformal field theory. It's known in literature as the *central charge*.

We can now proceed to study the effects of conformal transformations, generated by $T_{\mu\nu}$, on operators ϕ. Eq 2.32 can be rewritten as

$$
T(z) \phi(z_1) = \left(\frac{\Delta}{(z - z_1)^2} + \frac{1}{z - z_1} \frac{\partial}{\partial z_1} \right) \phi(z_1) + \text{ regular terms}
$$
$$
= \sum_{n \in \mathbb{Z}} \frac{L_n(z_1)}{(z - z_1)^{n+2}} \phi(z_1) \tag{2.34}
$$

through Laurent expansion $T(z) = \sum_{n=-\infty}^{\infty} L_n z^{-n-2}$, where L_n are the generators of the group, i.e. they are the content of the associated algebra:

$$
[L_n, L_m] = (n - m) L_{n+m} + \frac{c}{12} \left(n^3 - n \right) \delta_{n+m,0}
$$
$$
[L_n, \bar{L}_m] = 0 \tag{2.35}
$$
$$
[\bar{L}_n, \bar{L}_m] = (n - m) \bar{L}_{n+m} + \frac{c}{12} \left(n^3 - n \right) \delta_{n+m,0}
$$

called the *Virasoro Algebra*. Simple comparison in eq. 2.34 gives

$$
\begin{aligned}
L_{-1}\left(z_{1}\right) \phi\left(z_{1}\right) &= \frac{\partial}{\partial z_{1}} \phi\left(z_{1}\right) \\
L_{0}\left(z_{1}\right) \phi\left(z_{1}\right) &= \Delta \phi\left(z_{1}\right) \\
L_{n}\left(z_{1}\right) \phi\left(z_{1}\right) &= 0 \quad \text{for all } n > 0,
\end{aligned}
\tag{2.36}
$$

which are the algebraic equivalent of the Ward identities.

The reason we need this supplementary abstraction is that we are not going to obtain the correlators by cumbersome functional derivation. Instead, we are going to linearise the picture by introducing states in the *Hilbert space* the same way it's done in quantum mechanics, so that we can now study the object $\langle \phi(z_{1}) \phi(z_{2}) \rangle = \langle 0 | \phi(z_{1}) \phi(z_{2}) | 0 \rangle$.

We finally see why ϕ were called operators from the beginning! We postulate that $|0\rangle$ is conformally invariant, i.e. $L_{n}|0\rangle = 0$ for all $n \geq -1$. Then let's define the *highest-weight state* as

$$
|\Delta\rangle := \lim_{z \to 0} \phi(z)|0\rangle.
\tag{2.37}
$$

We can impose conformal covariance with our new algebraic Ward identities: A scaling operator ϕ will be conformal if and only if (i) $L_{n}|0\rangle = 0$ fro all $n \geq -1$ and (ii) $L_{0}|\Delta\rangle = \Delta\rangle$. These are known in literature as *primary operators*.

Different states can be built according to

$$
|\Delta; n_{1}, \ldots, n_{k}\rangle := L_{-n_{k}} \ldots L_{-n_{1}} |\Delta\rangle
\tag{2.38}
$$

The L_{0} generator acts as a counting operator

$$
L_{0} |\Delta; n_{1}, \ldots, n_{k}\rangle = (n_{k} + \cdots + n_{1} + \Delta) |\Delta; n_{1}, \ldots, n_{k}\rangle
\tag{2.39}
$$

The last ingredient we need in order to reconstruct the picture in an algebraic language is the unitarity of the representation since we need states to have real positive norm $\|L_{n}|\Delta\rangle\|^{2} = \langle \Delta | L_{n}^{\dagger} L_{n} | \Delta \rangle \geq 0$, where $L^{\dagger}$ is the correspondent hermitian conjugate operator. In other words, we need to construct dual states $\langle \Delta |$. A natural way to do so in the complex plane is to use the duality

$$
z \mapsto z' = -\frac{1}{z}
\tag{2.40}
$$

and from the Laurent expansion, we get the expression for the hermitian conjugate operators for a *unitary representation*:

$$
L_{n}^{\dagger} = L_{-n}
\tag{2.41}
$$

Any state at the origin can be mapped to a desired point z_{1} by the expansion in Taylor series $\phi(z_{1})|0\rangle = e^{z_{1} L_{-1}} |\Delta\rangle$. Since under the duality transformation a primary operator becomes $\phi(z') = z^{2\Delta} \phi(z)$, the dual states located at infinity are constructed as

$$
\langle \Delta | := \lim_{z_{1} \to \infty} \langle 0 | \phi(z_{1}) z_{1}^{2\Delta}
\tag{2.42}
$$

By applying the identity

$$
\langle \Delta | (L_{1})^{n} (L_{-1})^{m} |\Delta\rangle = \delta_{n,m} n! \frac{(2\Delta - 1 + n)!}{(2\Delta - 1)!}
\tag{2.43}
$$

we can easily get the new expression for the 2 point correlator

$$\langle 0|\phi(z_1)\,\phi(z_2)\,|0\rangle = (z_1 - z_2)^{-2\Delta} = \langle \phi(z_1)\,\phi(z_2)\rangle \tag{2.44}$$

We see that the correlator of primary operators behaves exactly as the correlator of scaling operators at critical point, thus qualitatively a conformal field theory seems to describe observables at criticality.

The beauty of our algebraic approach is that now all states can be constructed using just eq. 2.38. The full content of operators or states can be constructed by acting with generators. For each maximum value n of $L_{-n} \in \{L\}$, we are going to have a different representation of the Virasoro algebra, describing different primary operators. At level 1 we have a single state $L_{-1}|\Delta\rangle$ with norm

$$\|L_{-1}|\Delta\rangle\|^2 = \langle \Delta\,|L_1 L_{-1}|\,\Delta\rangle = 2\Delta. \tag{2.45}$$

We still must impose $\Delta \geq 0$ to obtain unitarity. Another simple condition is given by the two-point correlator of the energy-momentum tensor. Its norm is given by

$$\|T|0\rangle\|^2 = \langle 0\,|L_2 L_{-2}|\,0\rangle = \frac{c}{2} \tag{2.46}$$

Therefore $c > 0$ is necessary to ensure unitarity.

The picture becomes more complex at level 2, where we have two independent vectors $L_{-2}|\Delta\rangle$ and $L_{-1}^2|\Delta\rangle$. The unitarity condition requires that the determinant

$$
\begin{aligned}
\det{}_2(c,\Delta) &:= \begin{vmatrix} \langle \Delta\,|L_2 L_{-2}|\,\Delta\rangle & \left\langle \Delta\left|L_2\left(L_{-1}\right)^2\right|\Delta\right\rangle \\ \left\langle \Delta\left|\left(L_1\right)^2 L_{-2}\right|\Delta\right\rangle & \left\langle \Delta\left|\left(L_1\right)^2\left(L_{-1}\right)^2\right|\Delta\right\rangle \end{vmatrix} \\
&= \begin{vmatrix} 4\Delta + \frac{1}{2}c & 6\Delta \\ 6\Delta & 4\Delta(2\Delta + 1) \end{vmatrix} \\
&= 2\Delta\left(16\Delta^2 + 2(c - 5)\Delta + c\right)
\end{aligned}
\tag{2.47}
$$

called *Kac determinant* is positive definite. This is equivalent to the requirement that the matrix above is positive definite, which is true if and only if its eigenvalues are positive. An arbitrary choice of the conformal weight Δ and the central charge c may result in negative eigenvalues at level 2. The determinant computed in 2.47 at level 2 can be generalized to any level. At level n, Kac found the following formula bearing his name

$$\det{}_n(c,\Delta) = a_n \prod_{r,s=1;1\leq rs\leq n}^{n} (\Delta - \Delta_{r,s})^{p(n-rs)}, \tag{2.48}$$

Where we used the following parametrisation:

$$
\begin{aligned}
c = c_m &:= 1 - \frac{6}{m(m+1)} \\
\Delta_{r,s} = \Delta_{m-r,m+1-s} &:= \frac{[r(m+1) - sm]^2 - 1}{4m(m+1)}
\end{aligned}
\tag{2.49}
$$

A model is called *minimal* if m is a rational number. For each value of m, the table of possible conformal weights $\Delta_{r,s}$ with $r = 1, \ldots, m-1$ and $s = 1, \ldots, m$ is called the Kac table. The case $m = 3$, where $c = 1/2$, is shown below

$$r$$

2	1/2	1/16	0
1	0	1/16	1/2
	1	2	3	s

Now that we obtained the concrete values of dimensions for scaling operators, we can compare them to physical observables in order to establish or deny a connection. For our magnetic model, the most interesting observables, such a magnetisation density σ and energy density ε, are scalars under rotations so we can expect that $\Delta_{r,s} = \bar{\Delta}_{r,s}$. If we identify

$$\mathbf{1} = \phi_{1,1} = \phi_{2,3}, \qquad \sigma = \phi_{1,2} = \phi_{2,2}, \qquad \varepsilon = \phi_{2,1} = \phi_{1,3} \tag{2.50}$$

then we obtain the scaling dimensions

$$x_1 = 2\Delta_{1,1} = 0, \qquad x_\sigma = 2\Delta_{1,2} = \frac{1}{8}, \qquad x_\varepsilon = 2\Delta_{2,1} = 1. \tag{2.51}$$

If we use this information to complete equation 2.21 in order to obtain

$$x_\sigma = d - y_h = \frac{\beta}{\nu}, \qquad x_\varepsilon = d - y_\tau = \frac{1-\alpha}{\nu} \tag{2.52}$$

From which we can derive the values for the exponents $\alpha = 0$, $\beta = 1/8$, $\nu = 1$, which agree with the exponents of the two-dimensional Ising model!

Going back to the beginning of the discussion, we can now say that our observables may very well possess conformal invariance and for some models, it is proven that they can be described by a conformal field theory.

2.3 CFT on a cylinder

Even if conformal invariance seems to be generated by the absence of a length scale, its presence does not necessary break the symmetry and rather leads to corrections useful for extracting exponents, so we are going to briefly review what happens if we introduce a length scale in our geometry. The easiest way is to restrain the underlying space to an infinite strip of width L. We will, however, *compactify* the strip folding it to an infinite cylinder as shown in fig. 2.2 by mapping the plane points z to

$$w = \frac{L}{2\pi} \ln z. \tag{2.53}$$

This is a conformal map, we can write $w = t + iu$ and think of the coordinate t running along the cylinder as imaginary time, and u as space. CFT on the cylinder then corresponds to Euclidean QFT on a circle. The relation between the stress tensor on the cylinder and in the plane is given by

$$T(w)_{\text{cyl}} = (dz/dw)^2 T(z) + \frac{c}{12}\{z, w\} = (2\pi/L)^2 \left(z^2 T(z)_{\text{plane}} - \frac{c}{24}\right) \tag{2.54}$$
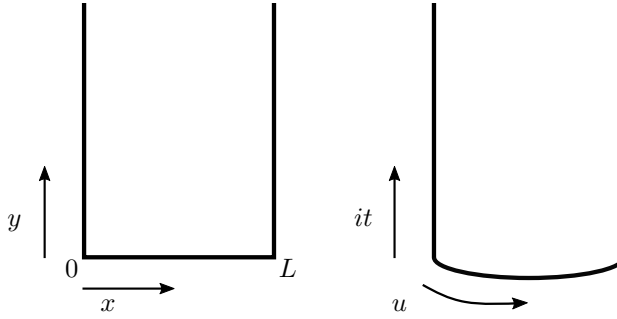
Figure 2.2: The compactification of the infinite strip of width L by folding it into an infinite cylinder.

The Hamiltonian $\hat{H}$ on the cylinder, which generates infinitesimal translations in t, can be written in the usual way as an integral over the time-time component of the stress tensor

$$\hat{H} = \frac{1}{2\pi} \int_0^L \hat{T}_{tt}(u)du = \frac{1}{2\pi} \int_0^L (\hat{T}(u) + \hat{\bar{T}}(u))du \tag{2.55}$$

Which in the plane corresponds to

$$\hat{H} = \frac{2\pi}{L}\left(\hat{L}_0 + \hat{\bar{L}}_0\right) - \frac{\pi c}{6L} \tag{2.56}$$

This is a remarkable equation that relates all of scaling operators in the theory to the spectrum of $\hat{H}$ on the cylinder!

In particular, the lowest eigenvalue, corresponding to the ground state energy, is

$$E_0 = -\frac{\pi c}{6L} + \frac{2\pi}{L}\left(\Delta_0 + \bar{\Delta}_0\right) \tag{2.57}$$

In all unitary CFTs, $\left(\Delta_0 + \bar{\Delta}_0\right) = 0$ and so we see how c can be measured from finite-size behaviour of the ground state energy.

E_0 also gives the leading term in the partition function $Z = Tr e^{-l\hat{H}}$ on a finite cylinder (or a torus) of length $l \gg L$. Equivalently, the free energy is

$$F = -\log Z \sim -\frac{\pi c \ell}{6L} \tag{2.58}$$

2.4 Boundary CFT

For now, we considered all fields living on $\mathbb{C}$, but it's well known from the behaviour of, say, electromagnetic fields, that the presence of a boundary affects them globally, and not just in the proximity of the surface. For instance, an electromagnetic wave will look very different if constrained to reflect between two surfaces: the electric and magnetic components' phases will be shifted by $\pi/4$.

How will conformal fields react to the presence of a boundary? As in general, boundary condition may vary. A natural requirement is that the off-diagonal component $T_{\parallel/\perp}$ of the stress tensor parallel/perpendicular to the boundary should vanish. This is the so-called *conformal boundary condition*.

Let's see what happens if our fields live in the upper-half complex plane $\mathbb{H}$ and the boundary is the real axis. The conformal boundary condition implies that $T(z) = \bar{T}(\bar{z})$ when 0 is on the real axis. This means that the correlators of $\bar{T}$ are those of T analytically continued into the lower half-plane. The conformal Ward identity now reads

$$
\left\langle T(z) \prod_j \phi_j\left(z_j, \bar{z}_j\right) \right\rangle =
$$

$$
\sum_j \left(\frac{\Delta_j}{\left(z - z_j\right)^2} + \frac{1}{z - z_j}\partial_{z_j} + \frac{\bar{\Delta}_j}{\left(z - \bar{z}_j\right)^2} + \frac{1}{z - \bar{z}_j}\partial_{\bar{z}_j} \right) \left\langle \prod_j \phi_j\left(z_j, \bar{z}_j\right) \right\rangle
$$

(2.59)

The integral expression for the algebra operators L now will have to be modified since we are going to integrate on semicircles centred on some point on the boundary, conventionally the origin. Now we have only one Virasoro algebra, and this is related to the fact, that conformal mappings that preserve the real axis correspond to real holomorphic functions. As before, the eigenstates of L_0 correspond to *boundary operators* $\phi(0)$ acting on the vacuum state $|0\rangle$. Fields on the boundary will have a different set of conformal weights. Although irrelevant for this chapter, BCFT will come handy at the end of the next one, where we will make use of this result.

Schramm Loewner Evolution

The divergence of correlation length is the reason for the formation of clusters of correlated values for observables. It is intuitive that the form of such clusters must hold some information about the universality class of the model since they too are the result of relevant operators. With this in mind, we will focus our attention on the study of geometrical shapes arising at criticality. The following chapter is based on the exposition of Cardy (2005), Cardy (2006), Bauer and Bernard (2006), Kager and Nienhuis (2004).

3.1 From spin to curves

Let's formalise our thoughts. Taking as an ideal abstraction the classical 2d Ising model, we will define each spin σ as a binary variable located at different points of the plane $(x, y) \in \mathbb{D} \in \mathbb{R}^2$. There are multiple ways to specify their locations, one of which is to say they are fixed at the *nodes* of a *graph* G. In abstract terms, a graph is a set of points with a given topology, but we have no need for such abstraction and will consider a Graph G(E,V) to be a set of vertices V connected by edges E, preferably along a recurrent path, i.e. a periodic tiling we cal *lattice*. We can see in 3.1 that such graphs are constructed by tiling the plane with a cell that can be a square, hexagonal, a triangular or even aperiodic, such as the beautiful Penrose tiling.
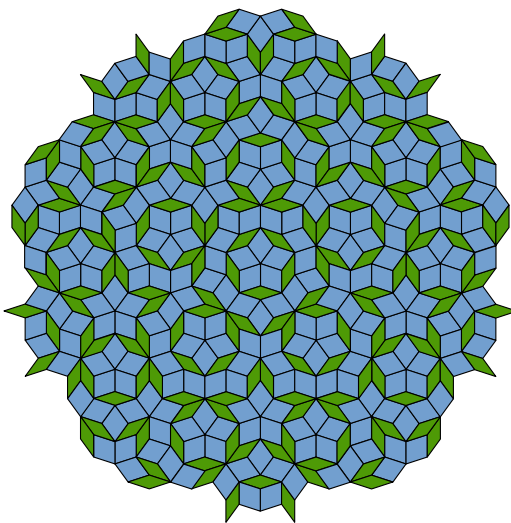
Figure 3.1: The beautiful Penrose aperiodic tiling

The Ising model on the triangular lattice is shown in fig 3.2 . Its partition function is equal to

$$Z = \sum_{\{\sigma\}} e^{-\beta \sum_{\langle ij \rangle} E_{ij}}, \tag{3.1}$$

where

$$E_{ij} = -J\sigma_i\sigma_j \tag{3.2}$$

and the sum $\sum_{\langle ij \rangle}$ means that we consider only interactions between adjacent spins, i.e. between vertices connected by an edge, while $\sum_{\{\sigma\}}$ si carried over all possible configurations.
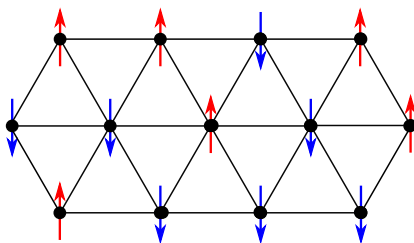
Figure 3.2: The Ising model on a triangular lattice

Any configuration can be mapped to a *loop model*. Suppose we define the model on a triangular lattice. We can introduce a *dual* lattice by introducing a vertex V' at the centre of each tile and connecting vertices of adjacent tiles by an edge E'. The lattice G'(V',E') is the graph formed by these elements. For a lattice forming a triangular tiling, the dual forms a hexagonal tiling of the plane as shown in fig. 3.3 . The reason we are interested in this object is that on it we can define surfaces containing our spins, as seen in picture 3.4.
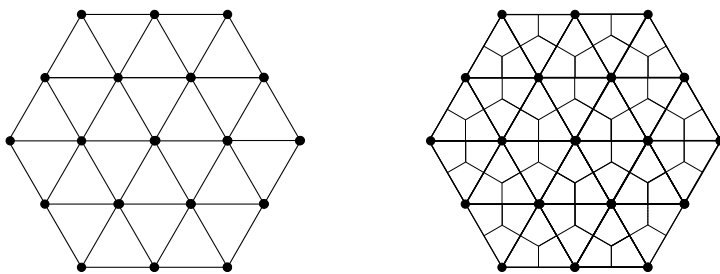
Figure 3.3: A triangular lattice and its dual hexagonal counterpart.

If now we decide to draw borders separating different spin values, the so-called *domain walls*, we end up with a picture containing a so-called *gas of loops* like in fig 3.5 . What is remarkable about this dual mapping, is that our partition function can also be mapped to one based on loop counting instead of configuration counting. We can easily show this on the triangular tiling, where domain walls are formed by tiles of the form 3.6 .

Instead of simply having a spin value on each vertex of the triangles, we are going to assign a value h that counts the enclosure of the loop within another, i.e. $h_2 = h_1 + 1$ if and only if loop 2 is enclosed in loop 1. We can interpret h_i as the values of a height
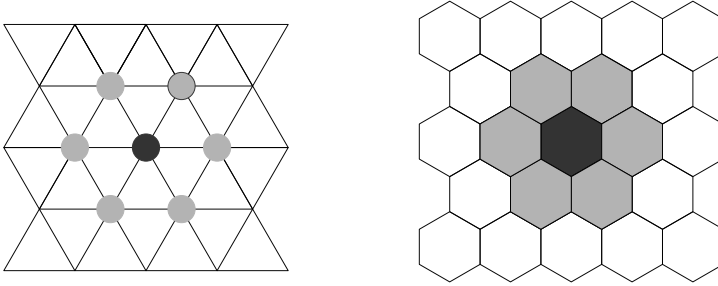
Figure 3.4: A spin portrayed in black on a triangular lattice with its neighbours coloured in grey. The same spins are mapped to hexagonal tiles in the dual lattice.
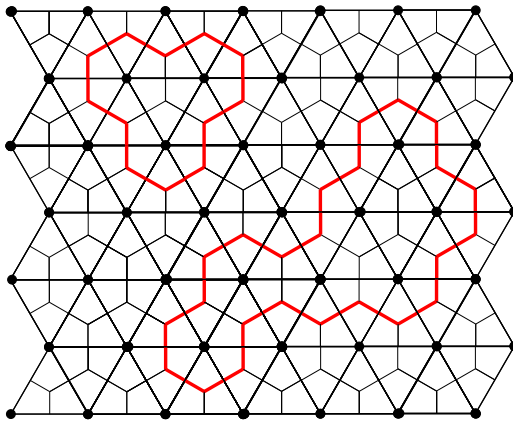

Figure 3.5: A triangular lattice and its dual hexagonal counterpart. The red curves separate different spin values

map, where domain walls are contours of equal height and the "hills" are the higher the more the loops are nested.

This is essential for counting loops. If now we assign to each triangle a weight

$$x(S_h/S_{h'})^{\frac{1}{6}}, \tag{3.3}$$

where S_h is a function of the height, to be made explicit later, and x is a positive temperature-like parameter, this *height model* can be mapped to a loop model as follows. Every time the heights in a given triangle are not all equal, we draw a segment of a curve through it, as shown in 3.6. These segments all link up, and if we demand that all the heights on the boundary are the same, they form a set of nested, non-intersecting closed loops on the dual honeycomb lattice, separating regions of constant height on the original lattice, as shown in fig 3.7 .

Consider a loop for which the heights just inside and outside are h and h' respectively. Since it's a loop it will have 6 more right (left) turns than the opposite, thus clarifying the exponent $1/6$ in the definition and yielding

$$x^{\text{length loop}}(S_h/S_{h'}). \tag{3.4}$$
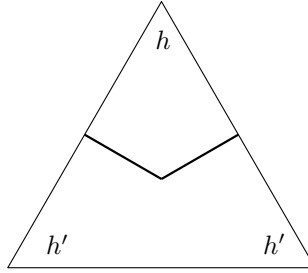
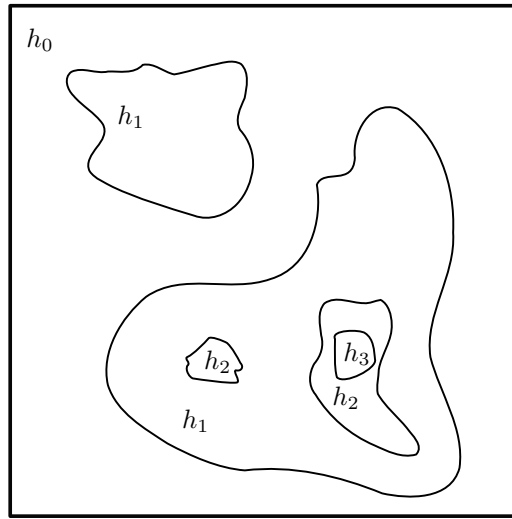**Figure 3.6:** Triangular cell with heights on its vertices

Figure 3.7: Nested loops and their heights.

Summing over all loops containing a given h' and with h outside can be expressed as

$$\sum_{h'} G_{h,h'}, \tag{3.5}$$

where $G_{i,j}$ is the *adjacency matrix* for the graph G, i.e. a matrix with values 1 if i is connected to j by a vertex and 0 otherwise. What we need to do is to sum the factor $(S_h/S_{h'})$ over all loops that are domain walls between h and h'. This can be done by taking the sum

$$\sum_{h'} G_{h,h'}(S_{h'}/S_h). \tag{3.6}$$

Since G is formed by ones and zeroes, by the *Perron-Frobenius theorem* it has a unique largest eigenvalue Λ and the corresponding eigenvector can be chosen to have strictly positive components. We are now going to define a posteriori $S_h > 0$ as the components of the unique eigenvector S with the largest eigenvalue Λ. The cumbersome expression now can be simplified obtaining

$$\sum_{h'} G_{h,h'}(S_{h'}/S_h) = \Lambda(S_h/S_h) = \Lambda. \tag{3.7}$$

What we end up with is a very simple formula for the partition function

$$Z = \sum_{\text{loop config.}} \Lambda^{\text{loops number}} x^{\text{total length}} \tag{3.8}$$

This partition function clearly will behave differently for different levels of x

$x \ll 1$ will describe a phase with few, small loops, we can identify with the ordered phase.

$x \gg 1$ will describe a phase very dense in loops, i.e. a disordered phase

We point out that the above decomposition in loops rather than in spin configurations can be obtained by algebraic manipulation starting from 3.1, defining $K = J\beta$ and expanding Z in power series of K and $1/K$ corresponding to low and high-temperature phases respectively.

In the high temperature phase (small K), we write

$$Z = \sum_{\{\sigma\}} \prod_{\langle ij \rangle} \cosh(K) \left(1 + \sigma_i \sigma_j \tanh(K)\right) \tag{3.9}$$

and expand the product on the r.h.s. into monomials. When summing over all $\sigma_i \in \{+1, -1\}$, the only monomials with a non-vanishing contribution are products of σ_i^2 only (a term σ_i sums $+1 - 1 = 0$). These monomials come from spins forming closed chains of neighbours. Hence, the sum over all spins can be replaced by a sum over all closed (possibly disconnected) loops on the lattice, namely

$$Z_{\text{high}} = [2\cosh(K)]^{NM} \sum_{\text{loops}} [\tanh(K)]^{\text{length}} \tag{3.10}$$

This is the so-called *high-temperature expansion* of the Ising model

In the low-temperature phase (large K), a given spin configuration is characterized by the borders of, say, all the spin +1 areas in a spin -1 background. Since the borders form loops, the sum 3.1 can be replaced by

$$Z_{\text{low}} = 2e^{NMK} \sum_{\text{loops}} e^{-2K(\text{ length })} \tag{3.11}$$

Where the contribution fo all down spin has been factored out of the sum. The factor 2 accounts for the degeneracy under reflection of all the spins. This is the *low-temperature expansion* of the Ising model.

We can see that the two phases are mapped into each other by the identification

$$e^{-2K} = \tanh K \tag{3.12}$$

which gives us

$$Z_{\text{low}}\ (K') = 2(\sinh 2K)^{-NM/2} Z_{\text{high}}\ (K) \tag{3.13}$$

and since both sides must become simultaneously singular, we have

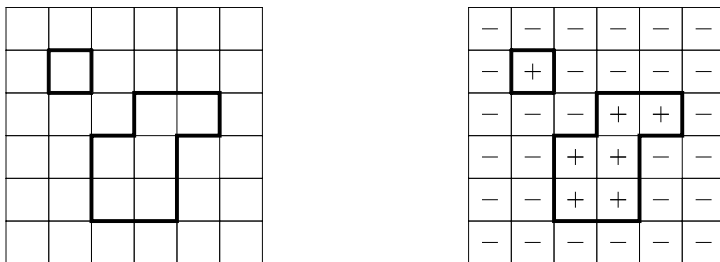$$K_c = -\frac{1}{2}\ln(\sqrt{2} - 1) \simeq 0.440686\ldots \tag{3.14}$$

Figure 3.8: A typical term in the high and low-temperature expansion for a square lattice. (a) A loop configuration in the high-temperature expansion with contribution $(2\cosh K)^{NM}(\tanh K)^{16}$. (b) a spin configuration corresponding to the same loop configuration in the low-temperature expansion, with contribution $e^{KNM}e^{-32K}$.

3.2 From global to local. Coulomb gas.

What we achieved is a description based on *global* variables for which a small local change in the configuration, i.e. the flip of one spin, will yield a huge change in the partition function since the new picture will correspond to a new loop configuration with a very different Boltzmann weight, as we can see in the example of fig. 3.9
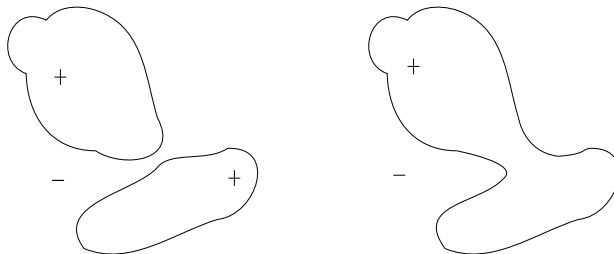
Figure 3.9: A single spin change can induce a huge change in the loop configuration

What we need is to find new *local* variables which can be used for the formulation fo a local field theory that can give us predictions on the criticality!

There is no ideal way of doing this, one solution is the so-called *Coulomb gas* method. The construction is the following: each loop will now be the sum of two oriented loops with total weight $\Lambda = e^{+i\chi} + e^{-i\chi}$, as schematically shown in fig. 3.10 .

This can be reformulated by assigning a weight $e^{\pm i\chi/6}$ at each vertex of the loops, choosing $e^{+i\chi/6}$ each time the loop turns to the right, and $e^{-i\chi/6}$ at each left turn (see fig. 3.11). Each loop will still correctly add up to $e^{\pm i\chi}$ since for it to be closed it will turn exactly 6 times to one direction more than to the other. We still have not said anything about how to choose orientation. Every loop will have the opposite orientation of the loop it is contained in. Now the heights h on the triangular lattice can be identified with a loop configuration since we can count line crossings, as shown in fig. 3.12

There is a one-to-one mapping between oriented loops and the values of h on the triangular lattice, with the restriction that the change of h between nearest neighbours
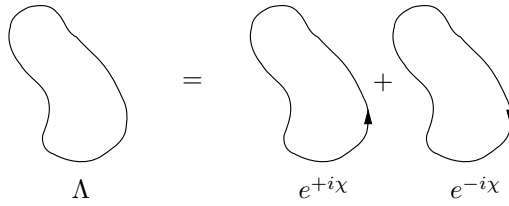
Figure 3.10: Any loop can be thought of as the sum of two oriented loops.
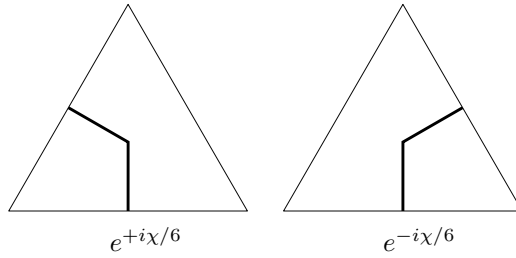

Figure 3.11: Weights assigned at each turn.

is restricted to $\|h_i - h_{i+1}\| \in \{-1, 0, +1\}$. Now our variables, the weights, are local and invariant under $h \to h + n$.

We are not going to prove the fact that under renormalization this picture will map to a CFT invariant under $h \to h + n$.

The best candidate for the continuum limit of the model is the Gaussian model:

$$S = \frac{g}{4\pi} \int (\nabla h)^2 d^2 r - \lambda \int \cos(2h) d^2 r \tag{3.15}$$

where the last term is added to constrain h to discrete values so that

$$
\begin{aligned}
h \in \mathbb{Z}\pi \qquad &, \lambda \to \infty \\
\text{Usual Gaussian model} \qquad &, \lambda \to 0
\end{aligned}
\tag{3.16}
$$

and we will redefine the heights to be multiples of π. For the usual free field theory, the height fluctuations grow logarithmically $\langle (h(r_1) - h(r_2))^2 \rangle \sim (2/g) \ln |r_1 - r_2|$, and the correlators of exponentials of the height decay with power laws:

$$\left\langle e^{iqh(r_1)} e^{-iqh(r_2)} \right\rangle \sim |r_1 - r_2|^{-2x_q}, \tag{3.17}$$

where $x_q = q^2/2g$.

The way we are going to obtain information about scaling dimensions with this model is to study it on a cylinder of circumference L and length $l \gg L$, where we have established in 2.58 that the partition function will go as

$$Z_G \sim e^{\frac{\pi c l}{6L}} \tag{3.18}$$

All loops not wrapping around on the cylinder will not feel the different topology, but the ones wrapping will have a wrong weight. To overcome this we can add two "electric charges" at the ends of the cylinder respectively equal to $e^{\pm i \chi h(\pm l/2)}$
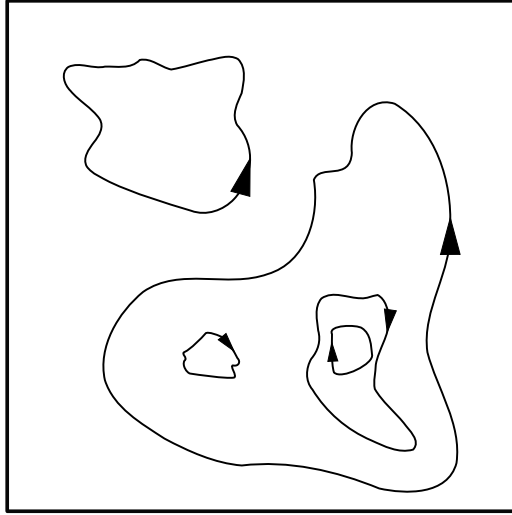
Figure 3.12: The height model is univocally mapped to oriented loops since we can count crossings.

Now that we compensated for the wrong counting, the new partition function will be

$$Z = Z_G \langle e^{-i\chi h(-l/2)} e^{+i\chi h(l/2)} \rangle \sim e^{\frac{\pi l}{6L}} e^{\frac{-2\pi l}{L} x_{q=\chi}} \tag{3.19}$$

Substituting $x_q = q^2/2g$ we find the effective value of $c/6 = 1/6 - (1/g)(\chi/\pi)^2$ Now any other correlator can be obtained by adding a corresponding charge, say $e^{\pm iqh(\pm l/2)}$ at both ends and taking the value of

$$\langle e^{-iqh(+l/2)} e^{+iqh(-l/2)} \rangle = \frac{\langle e^{i(q-\chi/\pi)h(l/2)} e^{-iq(-\chi/\pi)-h(l/2)} \rangle_{CG}}{\langle e^{iqh(-l/2)} e^{-iqh(l/2)} \rangle_{CG}} \tag{3.20}$$

$$\sim e^{\frac{-2\pi \tilde{x}_q}{L}}$$

Obtaining

$$\tilde{x}_q = \frac{1}{2g} \left((q - \frac{\chi}{\pi})^2 - (\frac{\chi}{\pi})^2 \right) \tag{3.21}$$

This is the scaling dimension in the model we started with, by the mapping to a Coulomb gas, described by a Gaussian model in the continuum limit. We still have too many parameters but we can express χ_2 by noticing that if the second part of 3.15 is needed to vanish at the continuum limit, λ has to be dimensionless and thus $\tilde{\chi}_2 = 2$ giving

$$g = 1 - \frac{\chi}{\pi} \tag{3.22}$$

If we now eliminate χ in 3.21 we get what essentially is the Kac formula.

Let's show another quick result we can obtain with the Coulomb gas formulation. Consider a cylinder of circumference 2π and a path propagating along it. What is the probability that it winds through an angle θ around the cylinder while it moves a distance $L \gg 1$ along the axis? This corresponds to a height difference $\Delta h = \pi(\theta/2\pi)$

between the ends of the cylinder, and therefore it adds to the free energy an additional term

$$P(\theta) \propto \exp\left(-g\theta^2/8L\right), \tag{3.23}$$

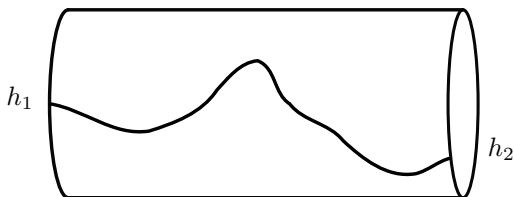and thus θ is normally distributed with variance $(4/g)L$.

Figure 3.13: The height difference $\Delta h = \pi(\theta/2\pi)$ for a path between the cylinders' borders

This all seems cumbersome and not at all mathematically rigorous. For the latter to be true, we would need a way to deal with smooth curves based on local variables. This mathematical description exists and is known as *Schramm Loewner Evolution*

3.3 The Loewner construction

So far we arrived at the conclusion that in order to study a critical model we can look at the interfaces between ordered phases which, as we saw, encode information about the exponents of the model. Ideally, we would like to have the probability distribution of loops in order to play with the partition function as we please. A first step towards this is the study of a segment of such loops, that can be created if for a region of our previous lattice we take two points on the border, thus partitioning it in right and left sides, and assign h and h' to each side, as shown in fig. 3.14 . Once we answered questions about this *chordal curve*, we can gain information about the statistics for loops in general.
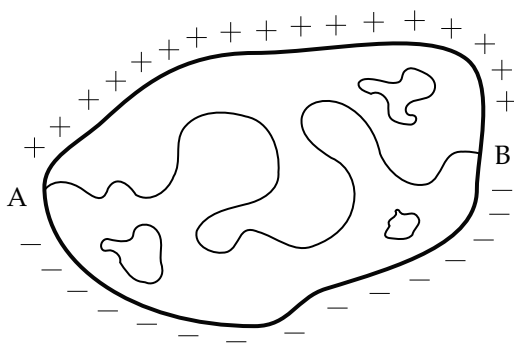

Figure 3.14: Boundary conditions $h = +, h' = -$ for a given region. Between points A and B a curve will always exist. Other loops do not concern us.

If we are going to claim conformity, then we can use (and even abuse) Riemann's theorem:

> **Riemann's Mapping Theorem:** *let D be a region in the complex plane* $\mathbb{C}$, z_0 *a point in D and* $U = \{w : \|w\| < 1\}$ *the unit disk in the w-plane. If D is simply connected and* $D \neq \mathbb{C}$, *then there exists exactly one conformal mapping* $f : z \to w = f(z)$ *from D onto U that satisfies* $f(z_0) = 0$ *and* $f'(z_0) > 0$.

This right away means that we can work on the upper-half complex plane $\mathbb{H}$ by mapping any simply connected region to it.

The strategy to describe such curves by one parameter is the *Loewner evolution*. Imagine a curve $\gamma(t)$ growing with time t, propagating upwards from in the half-plane starting from the origin as in fig. 3.15. By the same Riemann's theorem, there exists a map

$$\mathbb{H}/\gamma(t) \xrightarrow{g_t(z)} \mathbb{H} \tag{3.24}$$

that has the effect of "absorbing" back the curve into the origin, mapping the border of $\mathbb{H}/\gamma(t)$ to the real axis of $\mathbb{H}$. 3.15.
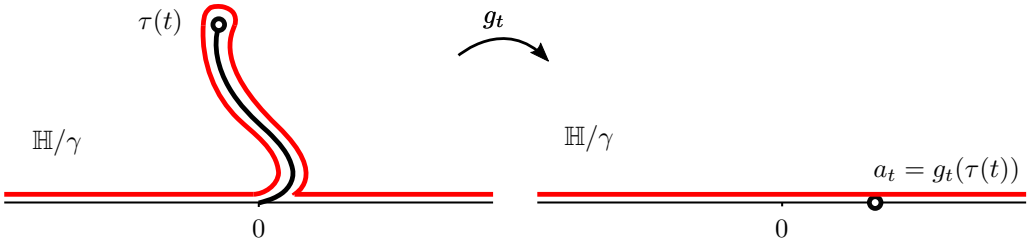
Figure 3.15: The curve γ is absorbed into the real axis by conformal mapping g_t

We can make this map unique by giving some additional constraints, such as saying what happens at infinity. It's clear that the further we distance from the curve, the lesser the space will be affected, yielding just a z term. There still would be corrections we can expand in $1/z$ obtaining:

$$g_t(z) \underset{z \to \infty}{\sim} z + 0 + \frac{c_1}{z} + \frac{c_2}{z^2} + \dots \tag{3.25}$$

where we set shifts equal to zero. This may look familiar to the reader if he/she had a good classical electrodynamics background. The solution for the potential of a charge distribution near an infinite conducting surface $\Delta\phi = -4\pi q\delta(\gamma(t) - z)$ yields a holomorphic (i.e. conformal) function ϕ in all the points of the space where $\Delta\phi = \partial_z\partial_{\bar{z}}\phi = 0$. This problem is notoriously solved by adding a mirroring charge distribution with the opposite sign on the other side of the conducting surface. At great distances, ϕ can be expressed in terms of a multipole expansion $q + d/z + \dots$ where q, the total charge, is zero and d is the dipole moment. It's clear than the latter will grow with the length of the curve and so we can express $c_1 = 2t$.

We made $g_t(z)$ unique, its behaviour at infinity will be:

$$g_t(z) \underset{z \to \infty}{\sim} z + \frac{t}{z} + o(1/z) \tag{3.26}$$

If we now look at how the tip of our curve $\tau(t)$ behaves, we find it to be mapped to the real axis at $a(t) = g(\tau(t))$.

The simplest example would be the map of a vertical segment of length $2i\sqrt{t}$. We can see that

$$g_t(z) = \left[z^2 + 4t\right]^2 \tag{3.27}$$

will map the tip to the origin. Any other point of the curve $z \in [0i, 2i\sqrt{t}]$ will be mapped to two points on the real axis on the left and right of the origin, thus mapping the border of $\mathbb{H}/\gamma(t)$ to the real axis of $\mathbb{H}$, as shown in fig. 3.16 .

Imagine now the curve $\gamma(t)$ has evolved in a generic way until time t. Starting from t, for an infinitesimal amount of time δt, the increment of the curve $\gamma'(t)$ can be approximated as a straight segment just like the slit we analysed. If $g_z(t)$ is the map for $\gamma(t)$, then $g_{t+\delta t}(z)$ will map $\gamma'(t)$ back to $\mathbb{H}$ is this way:

$$g_{t+\delta t}(z) = a(t) + [(g_t(z) - a(t))^2 + 4\delta t]^{\frac{1}{2}} \tag{3.28}$$

which is just the map of a vertical segment starting from $a(t)$ instead of the origin, since $g_t(z)$ will map $\tau(t)$ to $a(t)$.
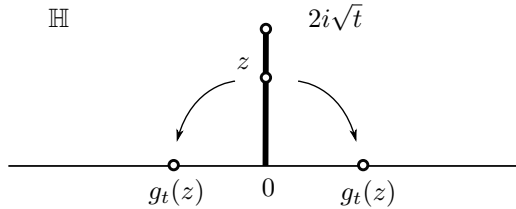
Figure 3.16: A segment of height $21\sqrt{t}$ is mapped back to the real axis.

Basically, we are saying that the final map is the composition $g_{t+\delta t} = g_{\delta t} \circ g_t$. Since it's not difficult to believe in the existence of the identity element, we can say that these maps form at least a semigroup.

It's not difficult now to take $\lim_{\delta t \to 0}(g_{t+\delta t} - g_t)/\delta t$ and obtain the differential equation

$$\frac{dg_t(z)}{dt} = \frac{2}{g_t(z) - a(t)} \tag{3.29}$$

This great result by Loewner means that now instead of needing two equations to define a curve on the plane $z(t) = x(t) + iy(t)$, we only need to know $a(t)$ to construct the whole curve!

The reader versed in analytical mechanics will not be amazed, even if she/he skipped electrodynamics. What we have done is in fact, analogous to a description of motion based on natural coordinates, i.e. tangent and normal velocities, where we constrained total velocity to be constant and $a(t)$ is the normal component of the acceleration.

The beauty of it lies in the fact that now we can classify continuous curves growing in the plane by just classifying continuous functions $a(t)$.

3.4 Schramm's theorem

The great contribution of Oded Schramm was to take $a(t)$ as a stochastic function and analyse what constraints are imposed on it by the requirement for $\gamma(t)$ to satisfy

- *Conformal invariance*, i.e. the self-similarity of the curve under conformal mappings.

- *Domain Markov property*, i.e. the curve needs to evolve at each point independently of its history up to it.

Which are requirements based on speculated properties of our interfaces.

Dividing a curve into two sections $\gamma_t(z)$ and $\gamma_s(z)$ as in fig. 3.17, after the mapping g_t, we will remain with the portion corresponding to time $s - t$. If the curves are *conformally invariant*, the remaining portion can be mapped by the same function except for the
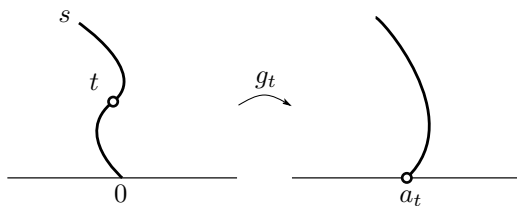
Figure 3.17: The curve divided into two parts and the remainder after the mapping g_t

starting point which gets shifted to $a(t) \equiv a_t$. This means that the law of $a_t - a_s$, given a_t, is the same as a_{s-t} given a_0. In particular, this implies that the increments $a_{(n+1)\delta t} - a_{n\delta t}$ are independent identically distributed random variables, for all $\delta t > 0$. The only process satisfying this is 1d Brownian motion, with a possible drift term:

$$a_t = \sqrt{k} B_t + \alpha t, \tag{3.30}$$

where $\langle B_t \rangle = 0$, $\langle (B_s - B_t)^2 \rangle = |s - t|$ and κ and α are constants. If the curve does not drift towards any direction, $\alpha = 0$.

Let's take a moment to remark what we achieved: we constructed a way of describing a vast family or 2d curves which possess conformal invariance and are generated by a stochastic process, by just one parameter κ!

We can now perform tests on the conformal curves generated by stochastic processes we started with, i.e. the loops describing interfaces in the Ising model, in order to classify them by a single parameter. It turns out that not only Ising but various models have in the continuum limit curves corresponding to different values of κ

- $\kappa = 6$: boundaries of percolation clusters Smirnov (2001)

- $\kappa = 3$: boundaries of Ising spin clusters Chelkak and Smirnov (2012)

- $\kappa = 4$: the harmonic explorer, and level lines of a gaussian field Schramm and Sheffield (2003)

- $\kappa = 8/3$: self-avoiding walk Lawler et al. (2011)

Some of these are rigorously proven while others still have not formal proof but are in accordance with numerical results.

3.5 Properties of SLE

3.5.1 Phases of SLE

The only parameter of SLE_κ is the variance of the generating Brownian motion. Any question we have about the behaviour of the curves will have an answer as a function of κ. Immediately we notice that the "winding" of the curve will increase with κ until it becomes enough winding that it intersects itself.

Let's try to evaluate the value of κ for which the so-called *double points* appear. A shown in fig. 3.18, close points of the curve will be torn apart by the reabsorption process if they do not coincide. On the other hand, if they coincide, everything between these two points needs to be mapped to a single point.
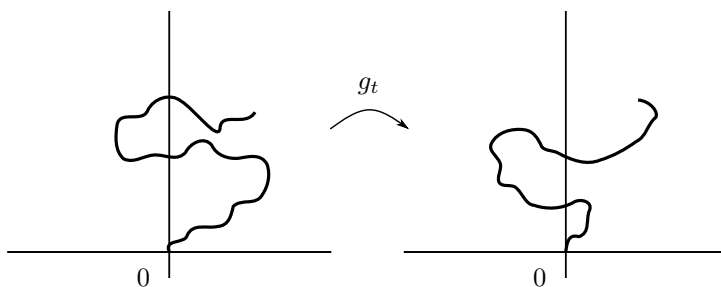
Figure 3.18: Close points are torn apart by the mapping g_t. Only coincident ones will map to the same point

We can simplify the picture by introducing the shifted mapping function $\hat{g}_t(z) \equiv g_t(z) - a_t$, which satisfies

$$d\hat{g}_t(z) = \frac{2dt}{\hat{g}_t(z)} - da_t. \tag{3.31}$$

This always maps the growing tip back to the origin and now the coincidence condition of two points becomes the condition that they are mapped to the origin. A point x_0 on the real axis gets mapped into $x_t = g_t(x_0)$ where

$$dx_t = \frac{2dt}{x_t} - \sqrt{\kappa}B_t. \tag{3.32}$$

The reader versed in stochastic processes will immediately recognise in it a Bessel process. It describes the motion of a particle repelled from the origin and also subject to Brownian noise. For small values of κ, the repulsive force always wins, and the particle goes off to infinity, while for large κ, eventually, random noise will cause the particle to reach the origin.

The critical value of κ can be found by equating the variance $\langle x^2 \rangle$ for the two cases. It turns out that for $\kappa \leq 4$ the curve almost surely does not have double points, while for $\kappa \geq 4$ the curve has double points, and in fact because of its self-similarity, it has infinitely many such points in any finite region.
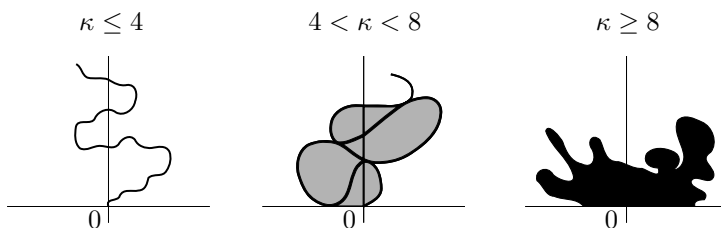

Figure 3.19: Three different phases for SLE curves

3.5.2   Fractal dimension

Fractal objects are not easy to study, they may have finite area encompassed by an infinitely long curve, so our usual definition of dimension falls apart. One way to define the *fractal dimension* of an object is to cover it with a large number of (overlapping) discs

of radius ϵ. Let $N(\epsilon)$ be the minimum such number. Then if $N(\epsilon) \sim \epsilon^{-d_f}$ as $\epsilon \to 0$, d_f is the fractal dimension.

An equivalent definition, for random fractals, is to ask for the probability $P(r, \epsilon)$ that the object intersects a disc of radius ϵ centred on r. If

$$P(r, \epsilon) \sim \epsilon^{D - d_f} f(r) \tag{3.33}$$

as $\epsilon \to 0$, where D is the embedding dimension (2 in our case), then d_f is again the fractal dimension. We will use this last definition and derive an equation for $P(r, \epsilon)$

Suppose the curve γ intersects a disc as in fig. 3.20 under the mapping $\hat{g}_\delta$, the first section of the curve is mapped onto the real axis, while the rest is mapped to a new curve starting from the origin. The disc itself is mapped to a new origin $g_{\delta t}(r)$ and its radius is slightly modified to $|\hat{g}'_{\delta t}(r)|\epsilon$.
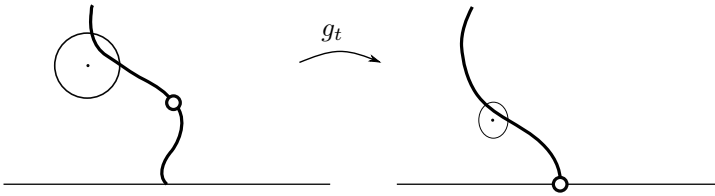

Figure 3.20: The curve intersecting a small disc, and its image under $g_{\delta t}$

By conformal invariance, the probability measure on this image should be the same as the one for the original curve. Equating the two, we can write the expression

$$P(x, y, \epsilon) = \left\langle P\left(x + \frac{2x\delta t}{x^2 + y^2} - \sqrt{\kappa}\delta B_t, y - \frac{2y\delta t}{x^2 + y^2}, \left(1 - \frac{2\left(x^2 - y^2\right)\delta t}{\left(x^2 + y^2\right)^2}\right)\epsilon\right)\right\rangle, \tag{3.34}$$

where the average is over the Brownian motion δB_t. Expanding to the first order in δt, while using $\langle B_t^2 \rangle = \delta t$, we get the partial differential equation

$$\left(\frac{2x}{x^2 + y^2}\frac{\partial}{\partial x} - \frac{2y}{x^2 + y^2}\frac{\partial}{\partial y} + \frac{\kappa}{2}\frac{\partial^2}{\partial x^2} - \frac{2\left(x^2 - y^2\right)}{\left(x^2 + y^2\right)^2}\epsilon\frac{\partial}{\partial \epsilon}\right)P = 0 \tag{3.35}$$

We can check that $P \sim \epsilon^{2 - d_f}$ is an eigenvalue of this differential operator. This is typical of SLE calculus, several critical exponents can be extrapolated by solving such eigenvalue problems.

We will not dwell into the methods for solving PDEs, but simply check that a solution can be

$$P \sim \epsilon^{1 - \kappa/8} y^{(\kappa - 8)^2/8\kappa} \left(x^2 + y^2\right)^{(\kappa - 8)/2\kappa} \tag{3.36}$$

from which we can obtain $d_f = 1 + \kappa/8$ for $\kappa \leq 8$

3.5.3 Left Passage Probability

Another greatly useful observable is the so-called *left passage probability* (LPP). consider a curve γ spanning the upper-half plane $\mathbb{H}$. Intuitively κ will parametrise how much the tip will deviate from the origin. If the curve propagates to infinity, every point in the domain will find itself on the left or on the right of the trace. If we average over a great

number of traces, we can find the probability that the curve passes, say on the left, of a given point.

This probability is well defined and as it turns out can be expressed again as a function of the sole parameter κ and the point's coordinates $z_0 = x_0 + iy_0$

$$\mathbb{P}\left[\gamma \text{ passes to the left of } z_0\right] = \frac{1}{2} + \frac{\Gamma(4/\kappa)}{\sqrt{\pi}\Gamma\left(\frac{8-\kappa}{2\kappa}\right)} \frac{x_0}{y_0} F_{2,1}\left(\frac{1}{2}, \frac{4}{\kappa}, \frac{3}{2}, \frac{-x_0^2}{y_0^2}\right), \tag{3.37}$$

where Γ is the gamma function and $F_{2,1}$ is the hypergeometric function (any reader will be excused for not being versed in it).

The proof is rather long, requires additional instruments and it is not vert illustrative, so we redirect the rider directly to Schramm et al. (2001) for supplementary information.

3.5.4 Winding angle

When discussing the Coulomb gas method applied to loops, we obtained the distribution of the winding angle, showing that its variance on a cylinder of length L is asymptotically $(4/g)L$. let's see if we can achieve the same result with our new SLE formalism.

We need to analyse the SLE growth in a semi-infinite cylinder of length L. Instead of working with this geometry, we can easily map conformally the cylinder in the unitary disk $\mathbb{D}$ by $w = e^{-z}$, so that the coordinates (u, v) become $(\rho = e^{-v}, \theta = \arg[e^{-iu}])$ as shown if fig 3.21
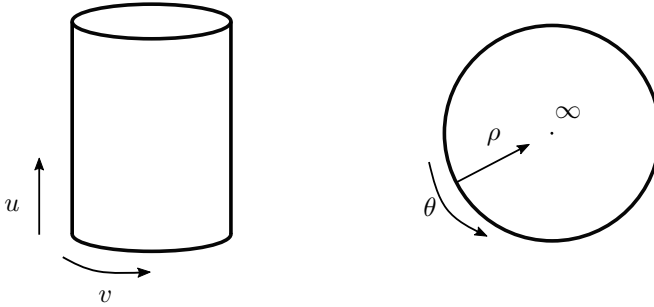

Figure 3.21: The map $(u, v) \to (\rho = e^{-v}, \theta = \arg[e^{-iu}])$

We now should reformulate the SLE in this domain, which will have a curve spanning from the boundary to the origin. This is, in fact, the original version of the Loewner equation and it's known as *radial* SLE. The radial Loewner equation is

$$\frac{dg_t(z)}{dt} = -g_t(z)\frac{g_t(z) + e^{i\theta_t}}{g_t(z) - e^{i\theta_t}} \tag{3.38}$$

What we need to understand in order to find the winding angle distribution, is how the tip $\gamma(\tau)$ behaves under the new mappings $g_t(z)$. In the previous case, the tip got mapped to a_t on the real axis, in this case, it gets mapped to a point on the boundary $e^{i\theta_t}$, with θ still normally distributed with variance κt. Asymptotically $\mathrm{Re}\, w \to \mathrm{Re}\, w - t$ under Loewner evolution, thus we can identify $L \sim t$ and write

$$\mathrm{Var}\, \theta \sim \kappa L, \tag{3.39}$$
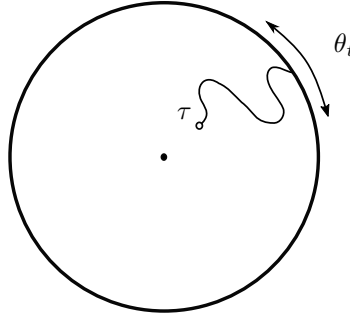
from which we can identify $\kappa = 4/g$.

Figure 3.22: The radial evolution of the curve. $\theta_t = g_t(\tau(t))$ is normally distributed with variance κt

3.6 SLE from BCFT

We can directly relate the parameter of SLE to the central charge of a boundary conformal field theory. Let's get back for a moment to the equation describing the evolution of γ on the real axis:

$$dx_t = \frac{2dt}{x_t} - \sqrt{\kappa}B_t. \tag{3.40}$$

This is equivalent to the description of the motion of a particle in a time-dependent vector field v such that

$$vdt = dt\frac{2}{z}\partial_z - d\xi_t\partial_z, \tag{3.41}$$

where $d\xi_t = \sqrt{\kappa}B_t$. We know that the 2d conformal group generators are $l_n := -z^{n+1}\partial_z$ so that

$$vdt = -2l_{-2}dt + l_{-1}d\xi_\xi \tag{3.42}$$

As discussed at the and of the previous chapter, a BCFT derives its properties by the fields on the boundary. The boundary conditions guarantee the existence, on the lattice, of a domain wall connecting the origin to infinity. We can always condition the spins in a region so that a domain wall is formed between two points of its boundary. We would like to impose conditions on the fields inside the region so that the existence of γ is guaranteed. We can condition the fields $\{\psi\}$ in the region Γ contributing to the path integral on the existence of γ_t, thus defining a state

$$|\gamma_t\rangle = \int [d\psi'_\Gamma] \int_{\psi_\Gamma = \psi'_\Gamma; \gamma_t} [d\psi]e^{-S[\psi]} |\psi'_\Gamma\rangle \tag{3.43}$$

The path integral, when conditioned on γ_t, gives a measure $d\mu(\gamma_t)$ on these curves. The state

$$|h\rangle = |h_t\rangle \equiv \int d\mu\,(\gamma_t)\,|\gamma_t\rangle \tag{3.44}$$

is independent of t, since it is just given by the path integral conditioned on there being a curve connecting the origin to infinity, as guaranteed by the boundary conditions. A conformal map on states will act with the generators of the Virasoro algebra L_n, but the

result is the same as in 3.42 . The conformal mappings $\hat{g}_t$ satisfying $d\hat{g}_t = 2dt/\hat{g}_t - da_t$ will act on the state as

$$|h_t\rangle = \exp\left(-\left(2L_{-2} - (\kappa/2)L_{-1}^2\right)t_1\right)|h_{t-t_1}\rangle, \tag{3.45}$$

thus the time independence translates to

$$\left(2L_{-2} - (\kappa/2)L_{-1}^2\right)|h\rangle = 0. \tag{3.46}$$

We recognize a representation of the Virasoro algebra of level 2. From this follows that if we act with L_1 and L_2, remember the commutators for the Virasoro algebra and use $L_1|h\rangle = L_2|h\rangle = 0$ while $L_0|h\rangle = h|h\rangle$, we can get

$$\begin{aligned} h = h_{2,1} &= \frac{6-\kappa}{2\kappa} \\ c &= \frac{(3\kappa - 8)(6 - \kappa)}{2\kappa}. \end{aligned} \tag{3.47}$$

We arrived at the fundamental relations between the parameter κ of SLE and the dimensions of a CFT! Note that the central charge c vanishes when $\kappa = 6$ or $\kappa = 8/3$. This corresponds to the continuum limit of percolation and self-avoiding walks respectively.

Critical model analysis

What we discussed so far needs to be put in practice. After all, the most sophisticated field theory means nothing if can't be applied to existing problems, in order to give us additional knowledge about them. We will dedicate this last introductory chapter to so far well-studied models which exhibit criticality with known exponents and are described by SLE in the continuum limit.

4.1 Discrete growth processes in 2d

In this section, we are going to describe examples of growth processes on lattices, which continuum limit we will explore at the end.

4.1.1 Percolation

Let us consider a hexagonal or honeycomb lattice on a portion of the plane. Let's describe the evolution of a pattern on the edges of such lattice. It starts at some point on the boundary, which in the example portrayed in figure 4.1 is chosen to be the top left-hand corner. The pattern, or walk, always grows by one edge from its tip. Each time the tip encounters the angle of a hexagon in front of it and chooses to turn to the left or to the right with equal probability.
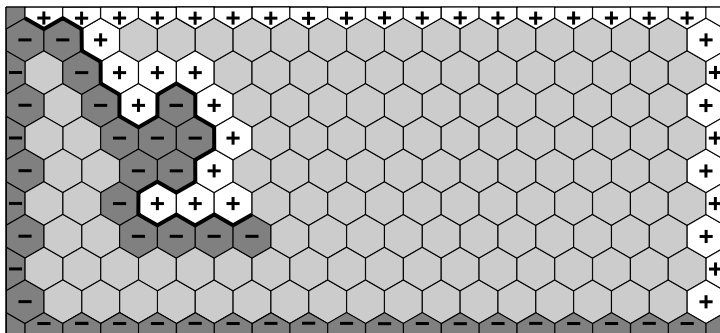
Figure 4.1: An example of percolation

Once it decides, we will mark the hexagon in front of the tip by + or -. As the walk grows, all the hexagons on its immediate left will be marked with -1, while all on its right will be marked +1. It may seem that if the walk curves enough, it may intersect itself. This is impossible since it will encounter a hexagon which has already been marked. The

marking procedure is chosen so that it has no choice: it will turn away from its previous trace.

We need one last thing: to specify what happens at the boundary. It will be easy to mark the hexagons at the boundary so that the walk never crushes on it. If we decide to mark half of the boundary with - (left bottom in fig 4.1) and the other half with + (top right), then the walk will be forced to end at the bottom right corner, even if, worst-case scenario, simply follows the border. It will never get stuck since at any intermediate time there is always at least one path from the growing tip to this final point which does not intersect the existing part of the walk. What we end up with is a *self-avoiding walk* on the lattice.

Since the number of paths on our discrete lattice is finite, we can always count them. The rules we have given determine the probability for a walk to emerge. In other words, we have a probability distribution, or measure, on the set of all such paths. However, since each hexagon's ± mark is extracted independently, we could have generated the same paths with the same probability distribution by simply marking all the interior hexagons independently with equal probability, leaving the border ones marked as before. This is the measure for independent site percolation. For each one of these configurations, there is exactly one path connecting the top left and bottom right corners, such that all the hexagons on one side are marked + and all those on the other are -. Note that the path is the boundary of the connected + cluster containing the upper right boundary of the whole domain, and that of the - cluster containing the lower-left boundary. Of course inside these clusters, there can be other markings and sub-clusters, but we are concerned only by the outermost cluster.

There is another important property of this measure: if, at a given step of the walk, we physically cut the lattice along the existing part of the path removing all the edges that formed the walk until that point, then the measure on the rest of the path is just the same as if we started the process from the tip, and defined it in the cut domain, with the left and right sides of the existing part of the path forming part of the boundary. This is the *Markov property* since defines independence of the probability measure from the path's history.

It's easy to see that we can generalise this problem by giving weights, or probabilities $p \in [0, 1]$ for each hexagon to be assigned a + ($1 - p$ for a -). We can easily identify p with a fictive temperature and its critical value will be clearly $p_c = 1/2$.

It has been rigorously proved by Smirnov (2001), that these curves possess a unique conformal invariant continuum limit with fractal dimension $d_f = 7/4$ and correspond to a SLE with parameter $\kappa = 6$ but with central charge $c = 0$.

4.1.2   Ising model

We don't need to change lattice to introduce a different model. By modifying the weights for this process we can obtain a new measure on paths. For instance, let's suppose that the marks $\pm$ now represent the possible values of an Ising spin $s(h) = \pm 1$ on each hexagon. If H is the hexagon just in front of the tip, mark it $\pm$ with probability $1/2(1 + m(H))$, where $m(H)$ is the mean magnetisation of an Ising spin at H in an Ising model defined in the whole of the cut domain, with the specified boundary conditions. That is

$$m(H) = \frac{\operatorname{Tr} s(H) e^{J \sum_{h,h'} s(h)s(h')}}{\operatorname{Tr} e^{J \sum_{h,h'} s(h)s(h')}} \tag{4.1}$$

where $-J \sum_{h,h'} s(h)s(h')$ is the usual Ising energy function in units of kT. If $s(H) =$

+1, the walk turns to the right, if -1, it turns to the left. If $J = 0$, which corresponds to the infinite temperature limit $T \to \infty$, we get back to the case of percolation. When $J \neq 0$ it will be difficult to simulate the walk since we would have to evaluate $m(H)$ at each step. We will prefer to simulate an equilibrium Ising model in the rectangle with the same boundary conditions as before, sample one configuration and draw the path connecting the top left and bottom right corners as before. Once again, the measure on curves we get this way is the same as that given by the growth process.

Looking now at the example of the Ising model, we can see the difference between walks here and in the percolation model. In percolation, if we modify the domain by distorting its boundary or taking out a piece of the interior, the measure on paths which do not intersect this remains unchanged. It's as the growing walk does not "feel" the region's boundary until it impacts on it. This is not true of the Ising model: the magnetisation of $s(H)$ depends on the shape of the whole region. This property is called *locality*.

This model also allows for a rigorous proof of its critical exponents and for the fractal dimension of cluster boundaries $d_f = 11/8$, which converge in the continuum limit to a SLE with $\kappa = 3$ and central charge $c = 1/2$, as it was definitively proven in Chelkak and Smirnov (2012) .

4.2   Disordered models

The question of whether interfaces in disordered systems are described by SLE or not is still unanswered. Intuitively the Domain Markov property does not hold as for ordered and it is unclear why it should hold for disordered systems. Moreover, conformal invariance is broken for a particular disorder realisation but may be restored after average over randomness! Recent numerical simulations provide evidence that interfaces in some random systems, frustrated or not, may be SLE curves.

4.2.1   Ising spin glasses

The *Edwards-Anderson model* of *spin glasses* Edwards and Anderson (1975) is defined by the Hamiltonian

$$H = -\sum_{(i,j)} J_{ij} \sigma_i \sigma_j \tag{4.2}$$

where the coupling constants J_{ij} are so-called *quenched* random variables, meaning that are constants that take different values for every *realisation of the disorder* or instance. Usually, they are chosen as random variables distributed normally with mean $\langle J \rangle = 0$ and variance $\langle J^2 \rangle =$ const. It is a well-known fact, that in 2d the correlation length ξ is divergent for $T = 0$.

Recent investigation about scaling behaviour of domain walls Melchert and Hartmann (2009) showed that their fractal dimension is $d_f \simeq 1.275$. Although conformal invariance is broken by the inhomogeneity of the couplings J_{ij}, it seems to be restored if we consider average quantities.

In a recent paper Amoruso et al. (2006) , a large-scale Monte Carlo simulation of the two-dimensional Ising spin glass provided evidence in that sense. To test specifically SLE, the authors extracted the driving function by using an algorithm that maps the simulated shape to $\mathbb{H}$ and then performs discrete mappings $g_{\Delta t}(z)$ for which the point of the curve on the real axis ξ_t needs to behave as a random variable with normal distribution and variance $\langle \xi_t^2 \rangle = \kappa$. Results are shown in fig. 4.2, they allow the estimation of $\kappa \simeq 2.1$ consistent with an estimate of $d_f \simeq 1.275$.
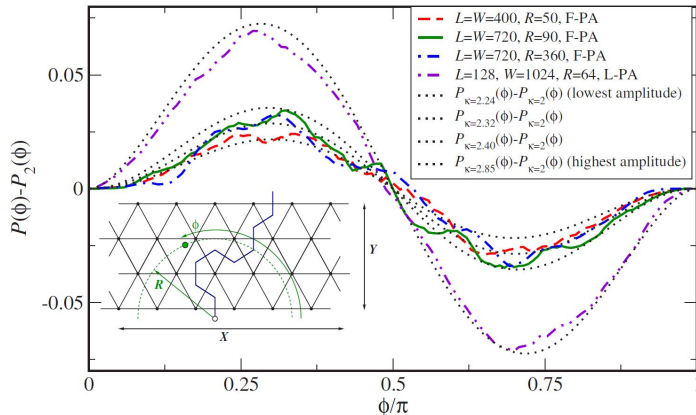
Figure 4.2: From Bauer and Bernard (2006):(Color online) Plots of $P(\phi, R) - P_2(\phi)$, where $P(\phi, R))$ is the probability for the domain wall to pass to the left of a point with polar coordinates (R, ϕ) (see inset). The magnitude of statistical errors (not shown) is consistent with the apparent fluctuations of the data lines. The predicted $P_2(\phi) = [\phi - \frac{1}{2}\sin(2\phi)]/\pi$ is subtracted to display small variations clearly. The data from the paths agree with SLE predictions for κ in the range $2.44 < \kappa < 2.40$. Inset: A domain wall of length $S = 9$ in a sample with $L = 4$ rows and $W = 6$ columns.

Conformal predictions for the winding number of the floating domain wall around long cylinders are reproduced by the data with a value of the fractal dimension compatible to the above estimate.

Measurements of the left-passage probability performed by Bauer and Bernard (2006) , were shown to be compatible with the Schramm formula with $\kappa = 2.32(8)$ as shown in fig 4.2 .

The boundary conditions where chosen periodically along one border by fixing the spins to have the same sign and anti-periodic along the other, so that the ending points of the domain wall are therefore not fixed. When the starting point of the interface is fixed by changing a bond on the lower boundary, a slightly larger value $2.85(10)$ is obtained from the Schramm formula.

4.2.2   Shortest path on critical percolation cluster

In a recent paper Posé et al. (2014) , it is numerically shown that the statistical properties of the shortest path on critical percolation clusters are consistent with the ones predicted for SLE curves for $\kappa = 1.04(2)$. An example of such path is shown in fig. 4.3.

The authors relied on the analysis of three observables. The winding angle was shown to be normally distributed with variance proportional to $\log L_y$, from which they were able to extract a coefficient $\kappa_{\text{winding}} = 1.046(4)$. The left passage probability was in accordance with $\kappa_{\text{LPP}} = 1.04(2)$. By mapping the curves back to the origin with discrete conformal maps $g_{\Delta t}$, and thus obtaining a statistics for the Brownian motion, the authors estimated $\kappa_g = 0.9(2)$. These results are in accordance with the fractal dimension of such curves, from which the coefficient is $\kappa_{\text{frac}} = 1.0462(2)$
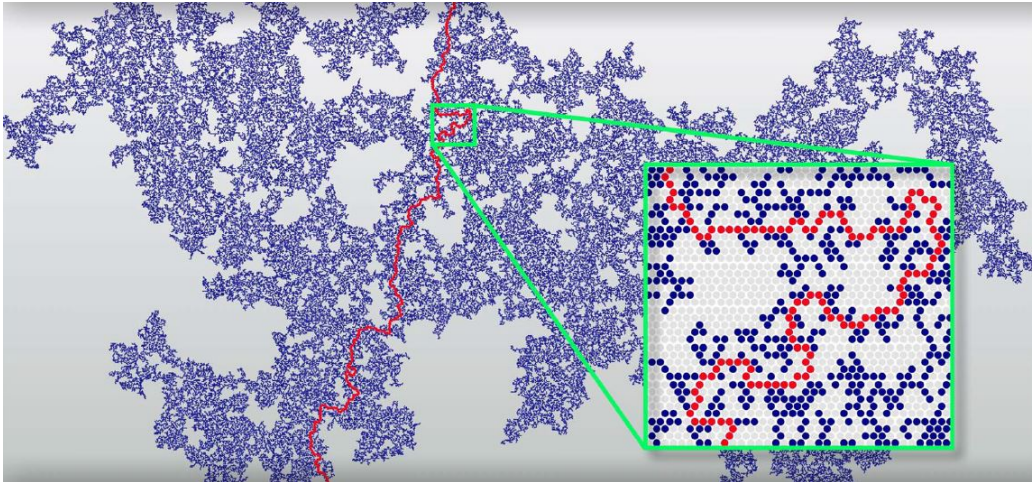
Figure 4.3: From Posé et al. (2014) : A spanning cluster on the triangular lattice in a strip of vertical size $L_y = 5512$. The shortest path is in red and all the other sites belonging to the spanning cluster are in blue.

Random Dimer Models

It may be argued that a natural generalization of the simple random walk on $\mathbb{Z}$ is given by the planar *dimer model*. While the simple random walk and its continuum limit, Brownian motion, are used extensively in all of probability theory, higher dimensional models like the dimer model are much less used or understood. The dimer model is at the moment the most successful two-dimensional random field theory, our aim is to obtain additional information about a special case of said model. For an introduction to the argument and its applications, we recommend the lectures Kenyon (2009). In this chapter, we will perform a numerical study of the effects of quenched disorder on the dimer model, showing how criticality and conformality emerge at its ground state at zero temperature. The results are published for now as preprint Caracciolo et al. (2020).

5.1 Dimer Models

A *dimer covering*, of a graph is a subset of edges which covers every vertex exactly once, that is, every vertex is the endpoint of exactly one edge Lovász and Plummer (2009) (see fig. 5.1). The dimer problem occurs experimentally, for instance, when a diatomic gas is adsorbed onto a crystalline substrate Kasteleyn (1967). Given a lattice, we ask for the number of ways that its vertices can be completely covered by non-overlapping dimers, each occupying two neighbouring vertices.
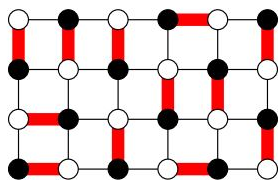
Figure 5.1: A dimer covering of a regular lattice. We can clearly see how its topology gives a bipartite graph.

A graph is bipartite when the vertices can be coloured black and white in such a way that each edge connects vertices of different colours. When the lattice is bipartite, dimer coverings are known in graph theory as *perfect matchings*. A classical example of dimer covering is showed in fig 5.2 with its equivalent *domino tiling* (tiling by 2×1 rectangles). When considering the Honeycomb graph as in fig 5.3 , we can construct the equivalent *lozenge tiling* (by tiling with $60°$ rhombi).

This *random surface* interpretation holds only for bipartite graphs, but there are many open problems involving dimer coverings of both monopartite and bipartite planar graphs.
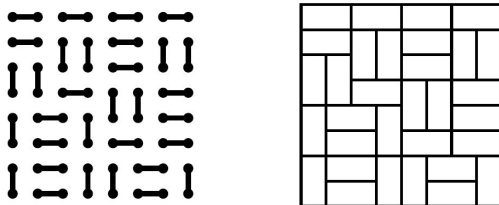
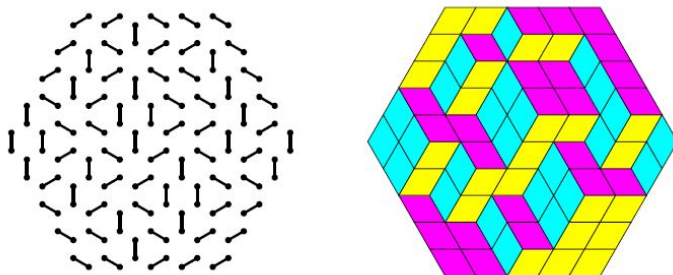**Figure 5.2:** Dimers on a square lattice and the equivalent domino tiling picture

Figure 5.3: Dimers on the hexagonal lattice and the equivalent lozenge tiling giving a 3d picture. Colours are added to trick the eye.

Kasteleyn, Fisher and Temperley showed that the 2d Ising model can be reduced to a generalized dimer problem Kasteleyn (1961), Temperley and Fisher (1961), Kasteleyn (1963).

Dimers have been used more recently to model valence bonds by the so-called *quantum dimer model* Kivelson et al. (1987), Moessner and Sondhi (2001) Kimchi et al. (2018).

Following the groundbreaking work of Kesteleyn, we will show how to obtain the partition function for dimer models. On the square lattice, let's define a positive weight $\pi(e) > 0$ on each edge. To each configuration, we can assign a Boltzmann weight

$$\pi(\mathcal{C}) := \prod_{e \in \mathcal{C}} \pi(e). \tag{5.1}$$

The partition function is then defined as

$$Z_G := \sum_{\mathcal{C}} \pi(\mathcal{C}) = \sum_{\mathcal{C}} \prod_{e \in \mathcal{C}} \pi(e), \tag{5.2}$$

Where the sum runs over all possible dimer configurations on G. In If we set $\pi(e) = 1$ for every edge, then Z_G is simply the number of dimer configurations on G. The topology of the square lattice makes it bipartite, thus we can denote $(w_1, w_2, ..., w_N)$ the half of vertices we will colour in white, and $(b_1, b_2, ..., b_N)$ the other half we will colour in black. Choosing an orientation for each edge, we can define the adjacency matrix called *Kasteleyn matrix* as

$$K_{ij} = \begin{cases} +\pi(w_i, b_j) & \text{if } w_i \rightarrow b_j \\ -\pi(w_i, b_j) & \text{if } w_i \leftarrow b_j \\ 0 & \text{otherwise} \end{cases} \tag{5.3}$$
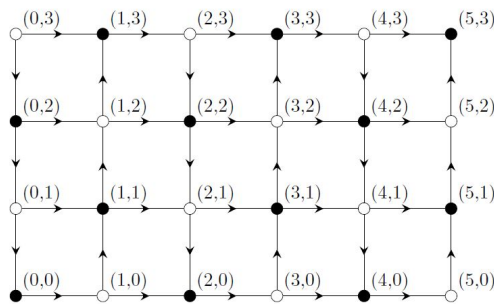
Figure 5.4: A Kasteleyn orientation of the square lattice. The coordinates of black and white vertices are indicated. Courtesy of Jesper Jacobsen.

The determinant of such matrix is

$$\det K = \sum_{\sigma \in \mathcal{S}_N} \text{sgn}(\sigma) K_{1,\sigma(1)} \dots K_{N,\sigma(N)}, \tag{5.4}$$

where $\mathcal{S}_N$ is the group of permutations of N elements. Not all permutations are relevant, in fact, the ones that contribute satisfy the adjacency of w_i to $b_{\sigma(i)}$, thus the determinant counts only dimer configurations:

$$\mathcal{C}(\sigma) := \left\{ \left(w_1, b_{\sigma(1)} \right), \dots, \left(w_N, b_{\sigma(N)} \right) \right\}. \tag{5.5}$$

Every dimer covering $\mathcal{C}(\sigma)$ will contribute with its weight $\pi\left[\mathcal{C}(\sigma)\right]$ up to a sign. In order to give all them the same sign, Kasteleyn proposed an alternating orientation shown in fig. 5.4 In this way, we obtain the partition function

$$Z_G = \left| \det K \right|. \tag{5.6}$$

For a generic graph, the free energy per dimer is defined as

$$f\left(\{z_i\}\right) = \lim_{N \to \infty} \frac{1}{N/2} \ln Z\left(\{z_i\}\right), \tag{5.7}$$

where $\{z_i\}$ is the set of weights we assign for each direction. In a square lattice with equal weight along both vertical and horizontal directions, the free energy is

$$f(1,1) = -\frac{1}{\pi} \sum_{k=0}^{\infty} \frac{(-1)^k}{(2k+1)^2} \equiv -\frac{G}{\pi}. \tag{5.8}$$

G is the so-called Catalan constant $G = 1 - 3^{-2} + 5^{-2} - 7^{-2} + \cdots = 0.915965594\dots$. Analogous results are obtained for Honeycomb, Triangular and more exotic lattices.

As a last classical dimer model, we would like to briefly present one problem that gained much interest in the community: the beautiful *Arctic circle*. Its appearance is easily visualised in the *Aztec diamond* domain, shown in fig. 5.5. A domino tiling of the Aztec diamond yields an interesting figure, which border is named Arctic circle. We are selecting a tiling at random, and we see a deterministic shape appearing. Most domino tilings of the Aztec diamond are frozen outside a disk. We see a surprising behaviour: a deterministic shape occurs inside a random object.

All these models, whatever their emergent disorder may be, are formulated with classical, ordered dimers. Our aim is the study dimer models with quenched disorder, which can be mapped to disordered models.
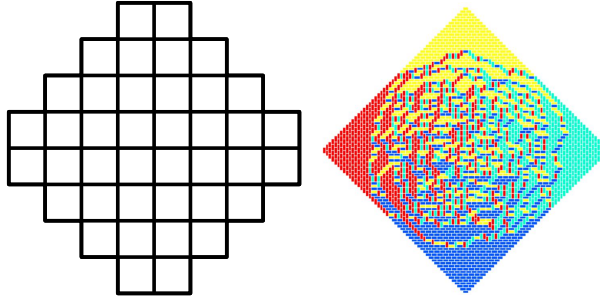
Figure 5.5: Left: the Aztec diamond domain. By tiling it rectangular tiles, we obtain the Arctic circle

5.2   The Random Dimer Model

As we showed in the previous chapter, the introduction of quenched disorder seems to break conformal symmetry and Markovianity. This is what interests us: we would like to study a generalized dimer model on a graph $G(E, V)$ in which we introduce disorder by assigning a weight $w_e \in \mathbb{R}^+$ to each edge $e \in E$. Let's assume that the weights w_e are independently and identically distributed random variables, having a defined probability distribution density $\rho(w)$. In this way, we can assign a cost $E[D]$ to each covering of the lattice:

$$E[D] := \sum_{e \in D} w_e. \tag{5.9}$$

We can introduce now a partition function

$$Z(\beta) := \sum_{D} e^{-\beta E[D]}, \tag{5.10}$$

depending on the fictitious inverse temperature $\beta = T^{-1}$. The number of coverings on the graph is given by $Z(0)$. Such model, we decided to call *Random Dimer Model* (RDM). We say that D^* is an optimal covering if

$$E[D^*] = \min_D E[D] = - \lim_{\beta \to +\infty} \beta^{-1} \ln Z(\beta). \tag{5.11}$$

The optimal configuration is almost surely unique and corresponds, therefore, to the "ground state" of the model. The introduced randomness can be thought as due to noise or it can be viewed as a representation of the system's disorder we are mapping onto our dimer model. In a dimer deposition picture, for example, randomness in edge weights might refer to a noisy, space-dependent binding energy of the diatomic molecules on the substrate.

The RDM is also a simple model for Random Euclidean matching problems (REMPs) Mézard and Parisi (1986) Mézard and Parisi (1988). In a REMP, a set of $2N$ points $\{x_i\}_{i=1}^{2N}$ is given, uniformly and independently generated on a given Euclidean domain (e.g., the unit hypercube). We search then for an optimal permutation of $2N$ elements σ that minimizes the matching cost

$$E[D_\sigma] := \sum_{i=1}^{N} d^p(x_{\sigma(2i)}, x_{\sigma(2i-1)}), \quad p \in \mathbb{R}^+, \tag{5.12}$$

where $d(x, y)$ is the distance between x and y. Each permutation defines a set of N pairs $D_\sigma := \{(\sigma(2i), \sigma(2i-1))\}_{i=1}^{N}$ of points that are matched. The goal is to find the matching $D^* = \arg\min_\sigma E[D_\sigma]$ that minimizes the total cost of the selected pairs. Finding the average cost of the pairing is a challenging task, due to the presence of Euclidean correlations between the pair costs. Euclidean matching problems, on the other hand, are of great interest in the theory of optimal transportation Villani (2008), Bogachev and Kolesnikov (2012), Santambrogio (2015), having a plethora of applications, from particle transportation Chertkov et al. (2010) to data science Peyré and Cuturi (2019).

On the other hand, a bipartite graph is a simplified model for the bipartite REMP, or Random Euclidean Assignment Problem (the very same formulated by Gaspard Monge in 1784), in which we have two sets of N points $\{x_i\}_{i=1}^{N}$, $\{y_i\}_{i=1}^{N}$, uniformly and independently generated on the square. The cost to be minimized will then be

$$E[D_\sigma] := \sum_{i=1}^{N} d^p(x_{\sigma(2i)}, y_{\sigma(2i-1)}), \quad p \in \mathbb{R}^{+}. \tag{5.13}$$

Important results about statistical properties, such as scaling exponents, average optimal cost and correlation functions were recently derived by Caracciolo et al. (2014), Caracciolo and Sicuro (2015b), Caracciolo and Sicuro (2015a). Computing the average optimal cost in the REMP or the REAP is a challenging task, due to the presence of Euclidean correlations between the pair costs Lucibello et al. (2017) Caracciolo et al. (2017).

On the other hand, the RDM in the $\beta \to \infty$ limit on planar graphs showed interesting conformality properties. For example, given two uniformly sampled dimer coverings, their union generates a set of curves and paths. Kenyon predicted the convergence of such curves to a Schramm-Loewner evolution SLE(4) Kenyon and Wilson (2011), and proved the conformality of the loops on bipartite lattices Kenyon (2014) .

As we have said, there is a correspondence between matchings and spin glasses in two dimensions Fisher (1966) . The problem of finding the ground state of the two-dimensional Edwards–Anderson model Edwards and Anderson (1975) can be mapped into a planar matching problem Bieche et al. (1980) Barahona (1982). Notably, the 2d EA model has a glass transition at zero temperature exhibiting scale invariance Bray and Moore (1984) Shirakura and Matsubara (1997) Hartmann and Young (2001) and it has been suggested that conformal invariance holds as well, as we have seen in in the previous chapter Amoruso et al. (2006), Bauer and Bernard (2006) .

These results motivate our search for the presence of criticality and conformality in the RDM on 2d lattices in the $\beta \to \infty$ limit, i.e. on the ground state, and search for correspondences with the REMP, REAP and 2d spin glasses. We will show that similar critical properties appear in the RDM, the REMP and the EA model, suggesting the existence of a unique universality class for these models. Moreover, such properties depend on the nature of the underlying graph over which the problems live.

5.3 Searching for criticality

In order to achieve small, local, perturbations of the optimal dimer cover, there are two possible ways we can modify the weighted graph G: inhibition of an edge or a vertex. Changing a single dimer of the cover will in order force other dimers to rearrange. Let's say we have a hexagonal or honeycomb lattice H, we find the optimal dimer cover D^* for a set of weights and then decide to inhibit an edge in the cover $\hat{e} \in D^*$, obtaining a new lattice $H/\hat{e}$. Now we can find the new optimal cover $D_{\hat{e}}^*$ for the lattice $H/\hat{e}$. Comparing

D^* with $D^*_{\hat{e}}$, we are able to evaluate the perturbation's extent. The set of all affected edges is given by the symmetric difference between the two coverings D^* and $D^*_{\hat{e}}$

$$S_{\hat{e}} = \{e \in E \colon e \in D^* \triangle D^*_{\hat{e}}\}, \tag{5.14}$$

pictorially exemplified in 5.6 . The result is a closed curve since both vertices of $\hat{e}$ have
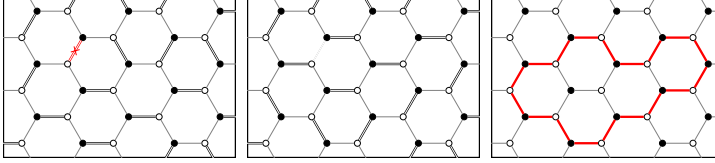

Figure 5.6: The resultant perturbation after prohibiting one edge of the optimal cover for a honeycomb lattice.

to be attached to new neighbours, triggering the rearrangement of other edges and so forth. If the curve weren't close, we would not have a dimer cover.

Another way of perturbing the system is to inhibit vertices. Deleting a vertex will not result in a lattice suitable to be covered by dimers, but deleting two vertices will yield a new cover $D^*_{v1,v2}$ and the resultant symmetric difference $S_{v1,v2}$ will be a curve that starts at $v1$ and ends at $v2$, as portrayed in 5.7. One could argue that this procedure is equivalent to the previous if we apply periodic boundary conditions merging the top and bottom sides. The deleting of vertices is then equivalent to the inhibition of the edge between them.

As we have previously seen, criticality means the divergence of correlation length. If a system is critical, a localized perturbation induces an extensive rearrangement that affects points that are arbitrarily far away from the location where the perturbation is applied. In our cases, the rearrangements form a curve and we will study its properties. Analogous topological defects on lattices were previously studied in the contest of elastic glasses by Zeng et al. (1999); Middleton (2000).
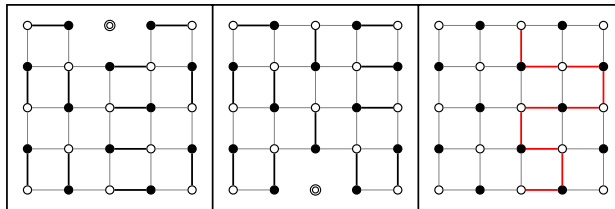

Figure 5.7: The resultant perturbation after deleting two vertices at the upper and lower border respectively.

5.4 The analysis

When we analyse systems of a large but finite size in order to simulate the thermodynamic limit, we need to be aware of the simulation's limitations. In our case, we need to mind the effects of the lattice border since our curves will inevitably hit it. To account for this, one can impose *Periodic Boundary Conditions* (PBC) on both sides, modifying the topology of the square into that of a torus $T^2 = S^1 \times S^1$. We analyse closed curves on three types of lattices: the honeycomb (H) lattice, the triangular (T) lattice, and the square (Q) lattice. Each lattice is obtained considering L rows of L sites, displaced in such a way that the lattice edge length is fixed to 1, so that the total number of sites is $2N = L^2$. We impose periodic boundary conditions in both directions, i.e., we work on the torus. For $L = 4$, for example, see fig. 5.8.
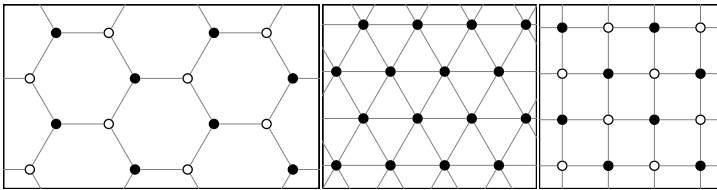
Figure 5.8: the honeycomb (H), triangular (T) and square (Q) lattices

Open curves instead will be best analysed on a square with open boundary conditions, since it is natural to let them spawn from one border to the opposite.

On the square with open boundary conditions, we will analyze the bipartite square lattice H, the monopartite triangular lattice T as well as the monopartite REMP and bipartite REAP.

Finding a perfect minimum-weighted matching is a task that would require the comparison of all possible matchings, an immense number considering that even a small chessboard of 8x8 vertices joined by a square lattice has more than 10^{13} possible dimer covers Kasteleyn (1963). We used a variant of Edmonds' Blossom algorithm Edmonds (1965a,b); Edmonds and Karp (1972), which yields the solution in $O(EV \log V)$, being V and E the number of vertices and edges respectively. In broad strokes, instead of finding all matchings and selecting the best one, it constructs the optimal matching edge by edge in such a way that the resultant complete matching has to be the optimal one. The algorithm is briefly explained in Appendix B, for a review on the subject and its modifications through the years, see Cook and Rohe (1999). The algorithm was implemented in a `C++` code with the use of the *LEMON* library Dezsö et al. (2011), which manages the modelling and optimization in networks, providing also the Blossom algorithm execution. The code run on different machines: one with 64 cores and 256 GB RAM memory, another with 920 cores and a total of 1150 GB RAM.

We numerically evaluated the probability distribution function $Pr[S_{\hat{e}} > s]$ of having a curve of length greater than s for all models considered above. Scaling theory for critical systems suggests that such a probability distribution can be written as

$$Pr[S_{\hat{e}} > s] = s^{-\zeta} \rho \left(s^\lambda L^{-1} \right), \tag{5.15}$$

for some scaling function ρ, such that $0 < \lim_{z \to 0} \rho(z) < +\infty$ and with $\zeta > 0$, just as we saw in eq. 1.20 . The function ρ is homogeneous and its argument is dimensionless. The scaling exponents ζ and λ have to be determined. The scaling ansatz in eq. (5.15) is numerically confirmed for all the analyzed models, including the REMP, see fig. 5.11. It is
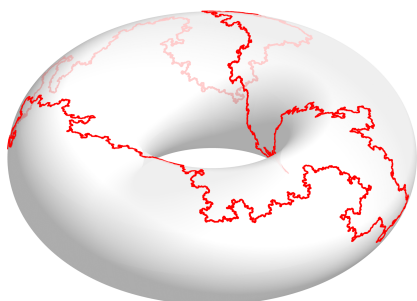
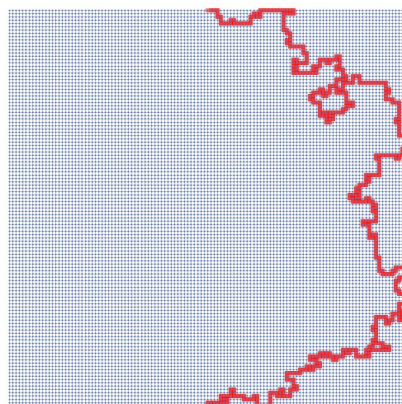**Figure 5.9:** Closed curve on the torus

Figure 5.10: Open curve on a square

evident that, as the size L increases, a power-law tail develops in all considered models. This implies that local perturbations induce extensive rearrangements with finite probability in the thermodynamic limit and the models are indeed on a "critical point". The results in Fig. 5.11 also suggest that the power-law exponent ζ on the torus is the same for the H and the Q model, whereas the T model has an exponent that is very close to the REMP one. On the open square, since curves have a minimum cut-off equal to the size L, the same analysis in less informative. After a rescaling $S \rightarrow (S - \langle S \rangle)/\mathrm{Var}S$ it suggests only that $\zeta = 0$, see fig 5.12
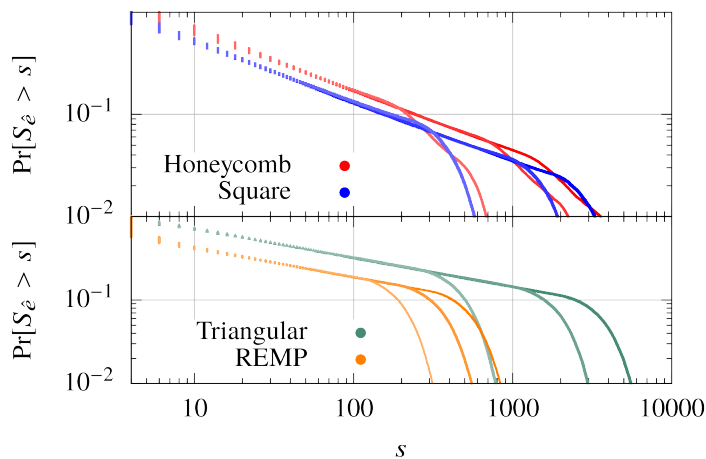
Figure 5.11: Cumulative distribution of the size "s" of the excitation for the different models. The sizes are $L = 100, 300, 500$ (from left to right in each case) for each dimer model. For the Euclidean cases, instead, the represented sizes are $2N = 2000, 5000, 10000$, from left to right
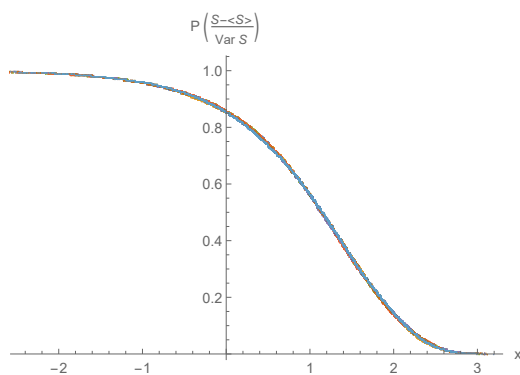

Figure 5.12: Probability $Pr[S'_{\hat{e}} > x]$ of H model on the open square, $S'_{\hat{e}} = (S_{\hat{e}} - \langle S_{\hat{e}} \rangle)/\text{Var } S_{\hat{e}}$. All the curves for different sizes collapse onto one.

5.5   Critical exponents and fractal dimension

Let's now try to evaluate the fractal dimension D_{f} of the curve. Assuming that $< S_{\hat{e}} >\sim L^\alpha$, from Eq. (5.15) we have

$$< S_{\hat{e}} >= \int_0^\infty S_{\hat{e}} Pr[S_{\hat{e}} = s]ds \propto \int_0^\infty s s^{-1-\zeta} \rho(s^\lambda L^{-1}) d(s^\lambda L^{-1}) s^{1-\lambda} L \propto L^{\frac{1-\zeta}{\lambda}} \quad (5.16)$$

$$\alpha = \frac{1-\zeta}{\lambda}. \quad (5.17)$$

The gyration radius of the cycle is defined as

$$R_{\hat{e}}^2 := \frac{1}{2S_{\hat{e}}^2} \sum_{i,j} d^2(r_i, r_j) \quad (5.18)$$

where r_i is the position of the ith node in the cycle and the sum runs over all pairs of vertices of the cycle. The gyration radius satisfies a scaling law of the form [1]

$$\left\langle R_{\hat{e}}^2 \right\rangle_{S_{\hat{e}}=s} = s^{2D_{\mathrm{f}}^{-1}} g\left(s^\lambda L^{-1}\right). \quad (5.19)$$

where g is a scaling function such that $0 < \lim_{z\to 0} g(z) < +\infty$, and the average is conditioned on cycles of length s. Assuming that $\left\langle R_{\hat{e}}^2 \right\rangle \sim L^\gamma$, we obtain

$$\left\langle R_{\hat{e}}^2 \right\rangle = \int_0^\infty \left\langle R_{\hat{e}}^2 \right\rangle_{S_{\hat{e}}=s} Pr[S_{\hat{e}} = s]ds \propto \int_0^\infty s^{2D_{\mathrm{f}}^{-1}} g\left(s^\lambda L^{-1}\right) s^{-1-\zeta} \rho(s^\lambda L^{-1}) d(s^\lambda L^{-1}) s^{1-\lambda} L \propto$$

$$L^{\frac{2D_{\mathrm{f}}^{-1}-\zeta-\lambda}{\lambda}} L = L^\gamma \quad (5.20)$$

$$\gamma = \frac{2D_{\mathrm{f}}^{-1} - \zeta}{\lambda}. \quad (5.21)$$

Taking into account eq. (5.17) a relation between the three exponents α, γ and ζ and the fractal dimension D_{f} is easily found,

$$D_{\mathrm{f}} = 2 - \gamma + \alpha, \quad (5.22a)$$

$$\zeta = \frac{2-\gamma}{2-\gamma+\alpha}. \quad (5.22b)$$

In particular, the fractal dimension and the power-law exponent ζ can be extracted by a careful measurement of α and γ.

A linear fit of $\log \langle O \rangle_L \sim \log L$, where $\langle \bullet \rangle_L$ denote an average at size L, for the length $\mathcal{O} = S_{\hat{e}}$ and gyration radius $\mathcal{O} = R_{\hat{e}}^2$ is certainly a good first approximation. However, finite-size effects must be accounted even if the simulation sizes L may seem great. In other words, our curves are never truly able to extend freely beyond a certain length, being subjected to the constrain of the system's size. To extrapolate the values of exponents α and γ to $L = \infty$, we used the so-called method of ratios Caracciolo et al. (1995). Finite-size scaling predicts that

$$\frac{\mathcal{O}(L)}{\mathcal{O}(\infty)} = f_\mathcal{O}(\xi(\infty)/L) + O(\xi^{-\omega}, L^{-\omega}) \quad (5.23)$$

---

[1]Here a hyperscaling assumption has been made: we assume that, to get a proper $L \to +\infty$ limit, the argument of g in Eq. (5.19) has the same scaling properties of the one of ρ in Eq. (5.15).
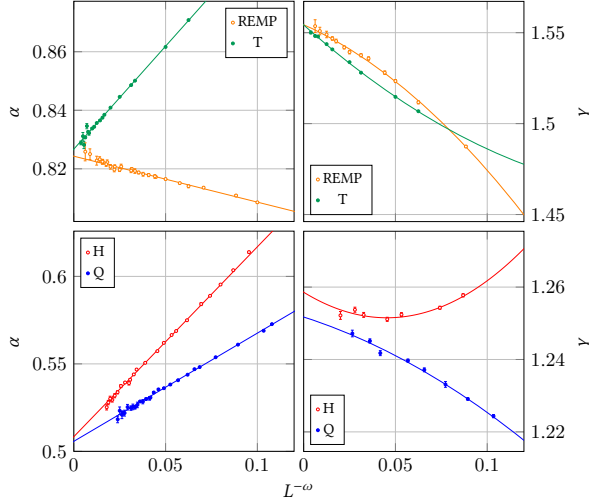
Figure 5.13: Extrapolation of α (left) and γ (right) for the different models. Each point represents the value ratios $\log_2\left(\langle S_{\hat{e}}\rangle_{2L}/\langle S_{\hat{e}}\rangle_L\right)$ (left) and $\log_2\left(\langle R_{\hat{e}}^2\rangle_{2L}/\langle R_{\hat{e}}^2\rangle_L\right)$ (right) for different sizes L, with its respective error. Sizes vary in the range $8 \leq L \leq 512$ for lattice models, and $64 \leq L^2 \leq 51200$ for the REMP. Each value has been averaged over 10^7–10^8 different instances. The value of both exponents in the bipartite models is clearly different from the one obtained for the monopartite ones.

Where $f_{\mathcal{O}}$ is a universal function and ω is a correction-to-scaling exponent. This holds true for any fixed scale factor a: $\mathcal{O}(aL)/\mathcal{O}(L)$. It follows automatically if we consider a first correction to the scaling law $\langle S\rangle_L \sim L^\alpha(1+b/L^\omega)$. Now the ratio will have the form

$$\log_2 \frac{\langle S_{\hat{e}}\rangle_{2L}}{\langle S_{\hat{e}}\rangle_L} = \alpha + \frac{\alpha^{(1)}}{L^\omega} + o\left(\frac{1}{L^\omega}\right). \tag{5.24}$$

Plotting it against the size L, we can fit our data, given in Fig. 5.13, using a function $f(L) = \alpha + \alpha^{(1)}L^{-\omega}$, with α, $\alpha^{(1)}$ and ω free parameters. Similarly for the gyration radius, expanding $\langle R_{\hat{e}}^2\rangle$ to the second order, we have

$$\log_2 \frac{\langle R_{\hat{e}}^2\rangle_{2L}}{\langle R_{\hat{e}}^2\rangle_L} = \gamma + \frac{\gamma^{(1)}}{L^\omega} + \frac{\gamma^{(2)}}{L^{2\omega}} + o\left(\frac{1}{L^{2\omega}}\right). \tag{5.25}$$

In this case, the fit, given in Fig. 5.13, has been obtained using a fitting function $f(L) = \gamma + \gamma^{(1)}L^{-\omega} + \gamma^{(2)}L^{-2\omega}$, with γ, $\gamma^{(1)}$ and $\gamma^{(2)}$ free parameters, whilst for ω was fixed to the same value estimated in the analysis for α. The data points have been obtained averaging over 10^7–10^8 different instances for each value of L. In the case of lattice models, we used $8 \leq L \leq 512$, whereas for the REMP we considered $64 \leq L^2 \leq 51200$. The results are summarized in fig.5.13. Once found α and γ, the fractal dimension of our curves is easily found $D_{\mathrm{f}} = 2 - \gamma + \alpha$

All our results are collected in Table 5.1. We observe that the values of the exponents naturally splits into two groups: the first one including the T model and the REMP, with curves having $D_{\mathrm{f}} = 1.273(2)$, and the second one including the Q and the H models, with curves having $D_{\mathrm{f}} = 1.252(2)$. The fact that the H and Q model share the same exponents, and similarly, the T model shares its exponents with the REMP, suggests that the only

	H	Q	REAP	T	REMP
$\langle \Delta E_{\hat{e}} \rangle$	1.115(1)	0.655(1)	0.637(1)	0.380(1)	0.585(1)
α	0.508(2)	0.506(1)	0.504(1)	0.827(1)	0.824(1)
γ	1.259(1)	1.252(2)	1.257(15)	1.554(1)	1.554(1)
ζ	0.593(1)	0.597(1)	0.596(6)	0.350(1)	0.351(1)
ζ (from fit)	0.593(1)	0.595(1)	0.588(1)	0.354(1)	0.350(1)
D_{f}	1.250(2)	1.253(2)	1.247(15)	1.273(1)	1.270(1)
$\kappa_{\mathrm{winding}}$	2.034(6)	2.003(7)	2.023(4)	2.181(4)	2.195(4)
$1 + \frac{\kappa_{\mathrm{w}}}{8}$	1.254(1)	1.250(1)	1.253(1)	1.273(1)	1.274(1)

Table 5.1: Asymptotic average optimal cost and of the scaling exponents for random dimer covering problems on the torus. $\langle \Delta E_{\hat{e}} \rangle$ is the average cost of the perturbation, i.e. the sum of weights composing the curve.

relevant feature that determines the scaling is the nature of the underlying graph, i.e., the fact of being bipartite or not.

The analysis of models on the square with open boundary conditions showed results compatible with the obtained for the torus, the only difference being that with $\zeta = 0$ $\gamma = 2$ and $D_{\mathrm{f}} = \alpha$. For the REMP we obtained $D_{\mathrm{f}} = 1.25(1)$. For the assignment problem the dimension is $D_{\mathrm{f}} = 1.26(2)$ and for the grid-Poisson we have $D_{\mathrm{f}} = 1.26(2)$.

5.6 Conformal invariance

The presence of criticality suggest the inspection of a stronger invariance, namely conformal invariance.

5.6.1 Winding angle

To this purpose, we computed the winding angle of the curves. Picking a random edge on the curve, we can define the angle θ_e between it and a chosen direction. Denoting the winding angle $\vartheta(e + 1) = \vartheta_e + \mathrm{angle}(e, e + 1)$ as the difference between angles of adjacent edge. On the lattice, we have that, since the curves are closed, $\sum_{e \in \mathcal{S}_{\hat{e}}} \vartheta(e) = 0$. The variance of the angle

$$\langle \vartheta^2 \rangle := \left\langle \frac{1}{S_{\hat{e}}} \sum_{e \in \mathcal{S}_{\hat{e}}} \vartheta^2(e) \right\rangle, \tag{5.26}$$

however, is found to grow linearly with $\log L$ as

$$\langle \vartheta^2 \rangle = a + \frac{\kappa_{\mathrm{winding}}}{4} \ln L, \tag{5.27}$$

see Fig. 5.14. The values of κ are given in Table 5.1. Once again, the T model and the REMP are found to have the same value of κ. This value is different from the value of κ obtained for the Q model and for the H model. As we have seen, this may follow from conformal invariance, see Duplantier and Saleur (1988). Furthermore, such behaviour is a hint of a possible SLE description, with the parameter $\kappa_{\mathrm{winding}}$ appearing in Eq. (5.27) being the parameter of the Schramm–Loewner evolution, see Duplantier and Binder
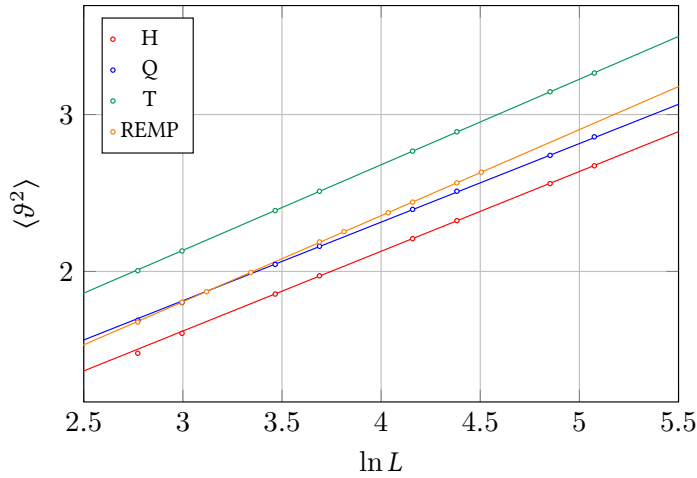
Figure 5.14: The variance of winding angles $\langle \vartheta^2 \rangle$ for the hexagonal (red), square (blue), triangular (green) models and the REMP (yellow). each point represents the winding angle's variance for a size L averaged by 107 iterations. Sizes vary in the range $16 \leq L \leq 128$ for lattice models and $256 \leq L^2 \leq 8100$. The error is smaller than the points' diameters.

(2002); Wieland and Wilson (2003). The quantity a is instead a nonuniversal constant. Moreover, given an SLE_κ, then $D_{\text{f}} = 1 + \frac{\kappa}{8}$ Rohde and Schramm (2005). This relation approximately holds for all the considered models, see Table 5.1, suggesting that the obtained curves are indeed SLE_κ but with different κ.

5.7 SLE observables

As we discussed, the logarithmic behaviour of $\text{Var}\vartheta$ can be explained by the presence of conformal invariance and it's also a result of SLE. The latter is a stronger assumption, its emergence in a system with quenched disorder is not a trivial assumption. We will analyse SLE observables in order to rule out this hypothesis.

5.7.1 Left Passage Probability

For all models on the square with open boundary conditions we can, as shown in the previous chapters, check the Left Passage Probability (LPP). For the SLE_κ the left passage probability is known for the points of the upper half-plane $\mathbb{H}$. Let us fix a point $z = x + iy \in \mathbb{H}$, then the probability that a trace of a SLE_κ, spanning from 0 to $i\infty$, passes to the left of this point is given by the Schramm formula

$$\Pr[\gamma \text{ left of } z] = \frac{1}{2} + \frac{\Gamma\left(\frac{4}{\kappa}\right)}{\sqrt{\pi}\,\Gamma\left(\frac{4}{\kappa} - \frac{1}{2}\right)} \frac{x}{y} F_{2,1}\left(\frac{1}{2}, \frac{4}{\kappa}; \frac{3}{2}; -\frac{x^2}{y^2}\right) \tag{5.28}$$

where $F_{2,1}$ is the hypergeometric function.

To do this check, we should map our grid, with the curve in it, into the upper half complex plane $\mathbb{H}$. The LPP is the probability for a curve to pass on the left of a point z. See Fig. 5.15.
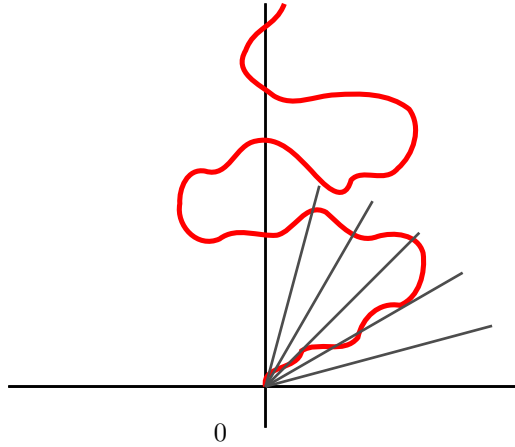
Figure 5.15: The upper half complex plane $\mathbb{H}$ with a curve in it and lines of equal probability level.

In this way, straight lines will indicate probability levels ($\Pr[\gamma \text{ left of } z]$ with $x/y =$ const). What we did was actually the opposite: we conformally mapped the upper half complex plane $\mathbb{H}$ with its level lines into our square and then compared how well the experimental LPP of our curves fitted the predicted one. We used two maps to do this: first, we mapped $\mathbb{H}$ into the unit disk $\mathbb{D}$ with a Möbious map.

$$g(z)_{\mathbb{H} \to \mathbb{D}} = i\frac{1+z}{1-z} \tag{5.29}$$

We then proceeded to map the unit disk to the square $\mathbb{S}$, so that the old axes origin will be mapped at the middle bottom, and the infinity will be at the middle top.

$$f(z)_{\mathbb{H} \to \mathbb{S}} = \frac{i\,F\left(\arcsin\dfrac{1}{\sqrt{i\frac{1-g(z)}{1+g(z)}}}, -1\right)}{\mathrm{Re}(K(2))} \tag{5.30}$$

Where $F(x; k)$ is the incomplete elliptic integral of the first kind

$$F(x; k) := \int_0^x \frac{dt}{\sqrt{(1-t^2)(1-k^2 t^2)}} \tag{5.31}$$

And $K(m)$ is the complete elliptic integral of the first kind

$$K(m) := \int_0^{\frac{\pi}{2}} \frac{d\theta}{\sqrt{1 - m\sin^2\theta}} \tag{5.32}$$

A brief check of the LPP for the above-mentioned percolator-explorator model yields the results are shown in fig. 5.16, where we choose two arbitrary points on the upper and lower borders. We can see that the theoretical probability levels, drawn in red, follow the levels in black obtained from numerical simulations. The theoretical levels are those for $\kappa = 6$, while the fractal dimension obtained by rescaling is equal to $1.79(2)$, thus in agreement with SLE_6
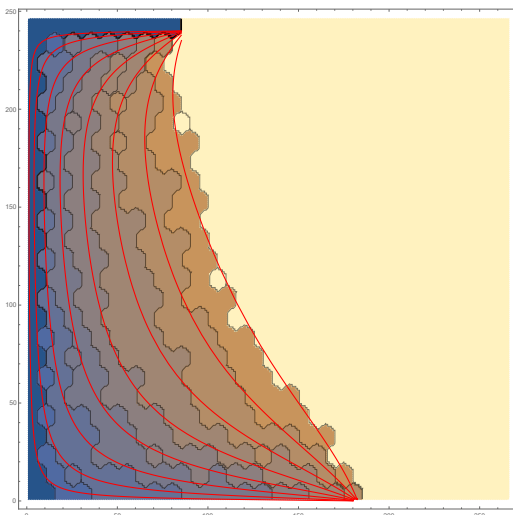
Figure 5.16: A plot of the simulated probability levels of the percolator-explorator on the hexagonal lattice on a square region with red curves being theoretical probability levels mapped from $\mathbb{H}$.

5.7.2 Bipartite models

Since the two categories fell into distinct universality classes, we will test if their SLE observables behave differently. Let's start with the bipartite models, namely the square H and assignment REAP.

For the H model figure 5.17 shows the astonishing agreement between the probability levels for $\kappa = 4.00(4)$ and the simulation ones. The algorithm we used was constructed upon the Mathematica language. The simulations were conducted on squares of sizes $L = 50, 10, 150, 200$, the latter of which is reported here. All sizes gave the same result, meaning that fine-size effects do not diminish sensibly enough. We can test optimal value by analyzing the $\mathcal{L}^2$ distance between curves for different κ, see fig 5.18 .

This may seem a success at first glance, but the fractal dimension obtained in the previous section is in disagreement with this value of κ! Such value implies $D'_{\mathrm{f}} = 1 + \frac{\kappa}{8} = 1.5$ not compatible with our previous $D_{\mathrm{f}} = 1.250(2)$.

The same analysis was performed for the REAP on squares of size $N^2 = L = 50, 100, 150$. The results are incredibly similar, we report the results in fig. 5.19.

Once again this striking accordance for the LPP is in conflict with the previous value of $D_{\mathrm{f}} = 1.253(2)$.

In a previous work, Zarinelli (2008), analysed the so-called *Grid-Poisson Matching Problem*. In it, two sets of N points $x_{i=1}^N$ and $y_{i=1}^N$ are given on a square of side $L = 1$. One of them is uniformly and independently generated, while the other consists of points placed on the vertices of a square grid with spacing $1/\sqrt{N}$. The cost to be minimized is

$$E[D_\sigma] := \sum_{i=1}^N d^2(x_{\sigma(2i)}, y_{\sigma(2i-1)}). \tag{5.33}$$

The analysis showed the same discordance between the best fit for the LPP $\kappa_{\mathrm{LPP}} = 4$, and the fractal dimension of curves, for which $\kappa_{\mathrm{frac}} = 8(d-1) = 2.4(2)$.
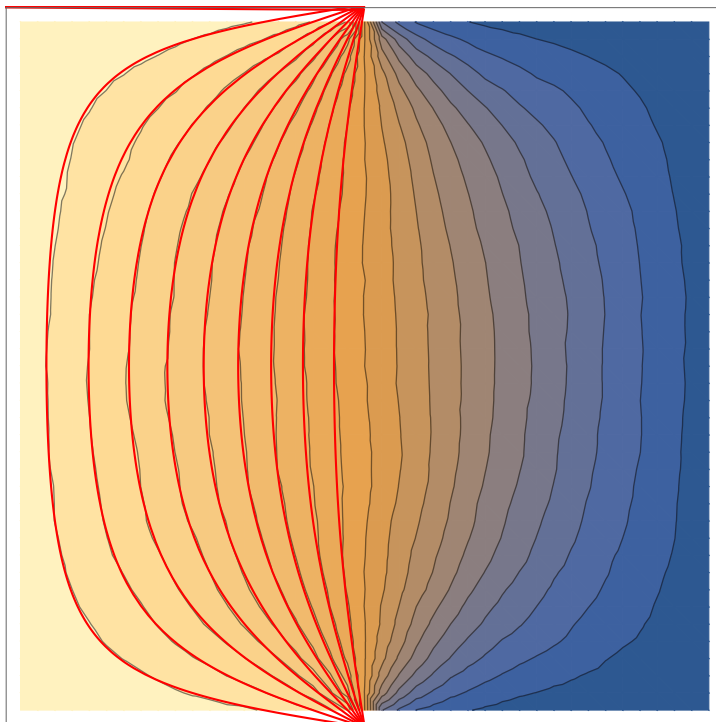
Figure 5.17: LPP for the Square lattice. The red curves are the theoretical probability levels after the conformal mapping. The colour shade indicates the LPP, from light yellow (LPP~ 0) to dark blue (LPP~ 1). Among the shades, we draw in black the same probability levels obtained from numerical simulation
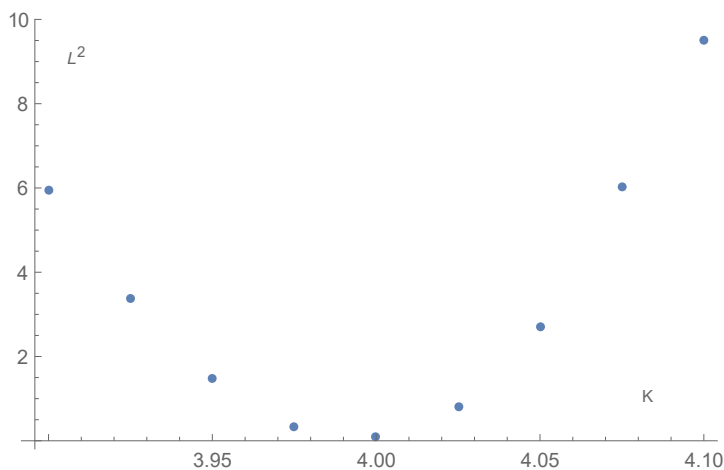

Figure 5.18: The $\mathcal{L}^2$ distance between experimental curves and theoretical values for the LPP of the Square lattice versus the fitted value of κ
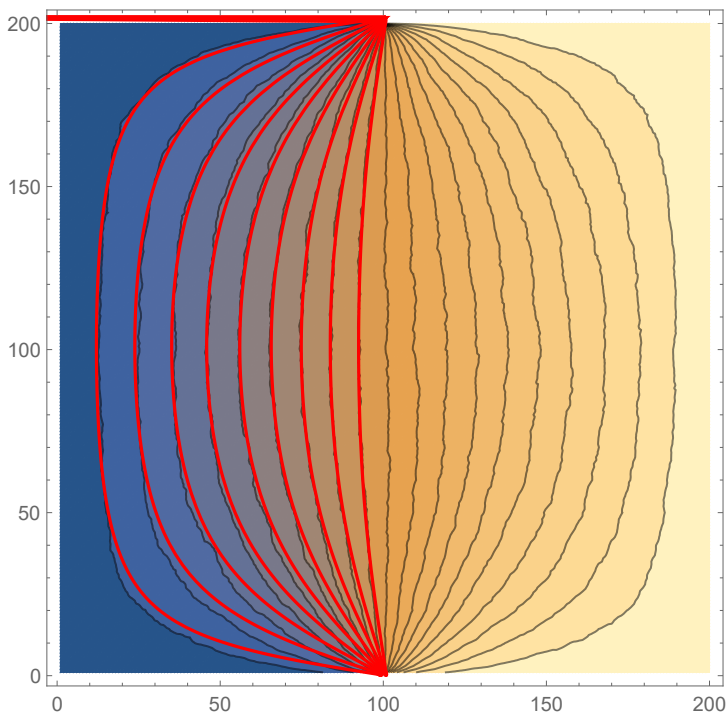
Figure 5.19: LPP for the REAP, for $2N$ points on a square of size $L = \sqrt{2N} = 200$. The theoretical values of probability lines for $\kappa = 4$ are portrayed in red, they lay just above the experimental values.
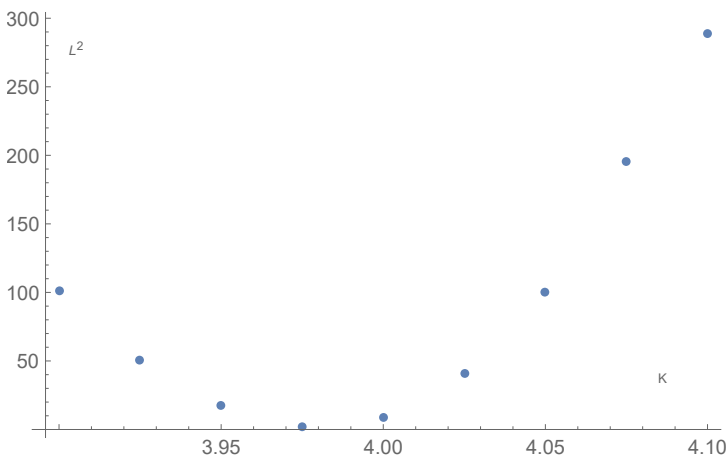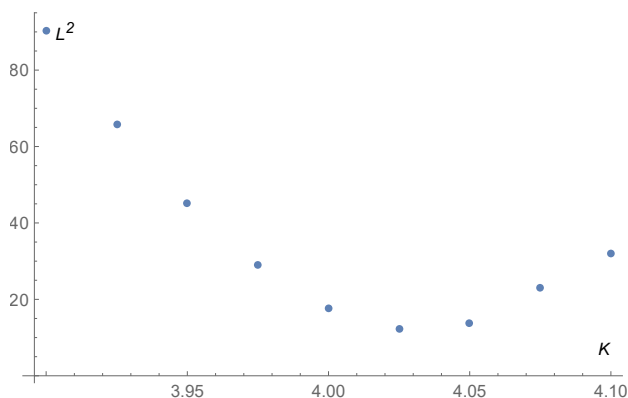

Figure 5.20: The $\mathcal{L}^2$ distance between probability lines of numerical simulations and theoretical curves for the REAP versus the different values κ for the fit.

5.7.3 Monopartite models

The picture changes if we analyse monopartite problems, namely the triangular lattice T and the REMP. For the REMP, the results are reported in fig. 5.21 .
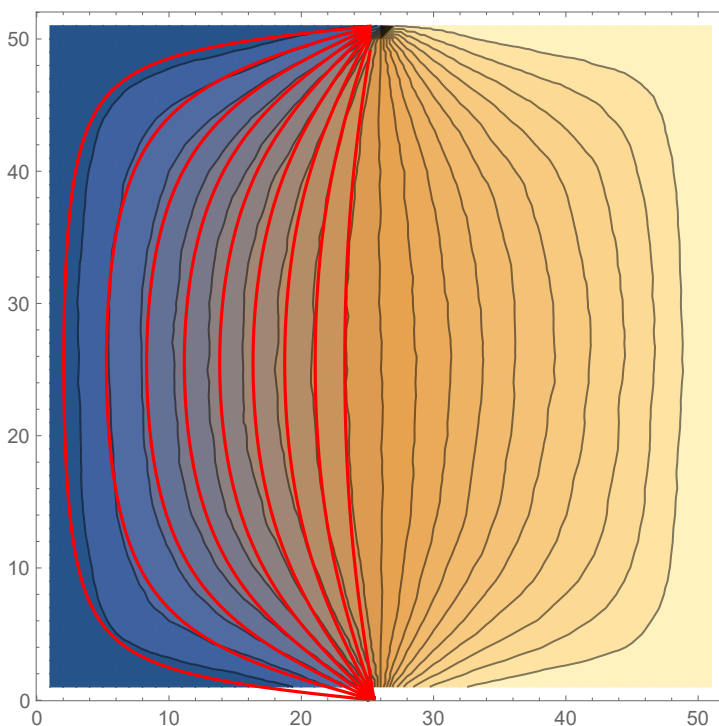
Figure 5.21: LPP for the REMP on a square of size $L = 50$. The red curves are the theoretical probability levels for $\kappa = 4$, which is the best fit.

As we can see, although experimental values are fitted best by SLE_4, there is no value of κ that guarantees a perfect match. This is clearly portrayed in fig 5.22, where $\mathcal{L}^2$ in never quite able to converge to 0.

Figure 5.22: The $\mathcal{L}^2$ distance between probability lines of numerical simulations and theoretical curves for the REMP versus the different values κ for the fit.

The same picture is obtained analysing the "lattice counterpart", i.e. the Triangular lattice. This all seemed suspicious and we decided to perform additional checks in order

to understand if the results are affected by border conditions.

Fig. 5.23 reports the LPP analysis for the REMP with a different choice of the deleted vertices. Choosing them not aligned generates twisted curves that can still be mapped on $\mathbb{H}$ and compared with theoretical values for SLE. The results do not change, $\kappa = 4$ gives still the best fit, but it does not converge properly.
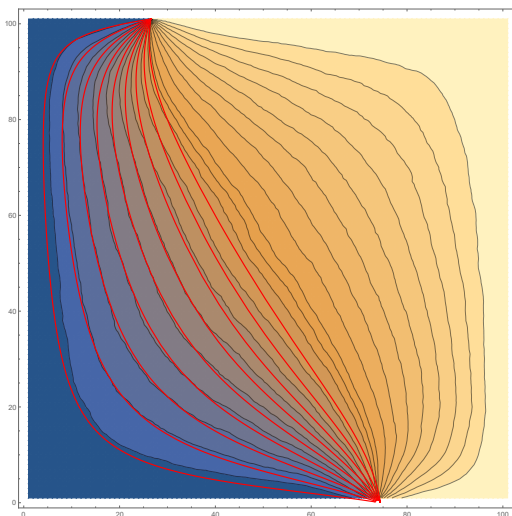

Figure 5.23: Left Passage Probability for the REMP on a square of size $L = \sqrt{N} = 100$ and deleted vertices not aligned. Despite the twist, the best fit is still given by $\kappa = 4$

5.7.4 Domain Markov Property

The conclusions derived from LPP tests were not in accordance with the values of Varϑ, which clearly exhibited a behaviour present in conformal invariant models.

To obtain greater insight about the latter we decided to check a fundamental property, namely the presence of the Domain Markov Property, for which

$$P_D\left(\gamma_2|\gamma_1\right) = P_{D/\gamma_1}\left(\gamma_2\right), \tag{5.34}$$

Meaning that the probability for the curve to be γ_2 when conditioned to γ_1 is the same probability if we consider a "cut" domain D/γ_1, as shown below.
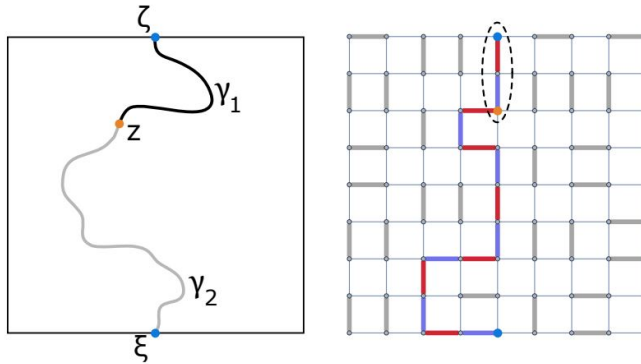
Instead of analysing the probabilities, we can look at observables $\mathcal{O}[\gamma_2]$, which ought to have expectation values given by

$$\int \mathrm{d}P_{D,\zeta,\xi}\left(\gamma_2 \mid \gamma_1\right)\mathcal{O}\left[\gamma_2\right] = \int \mathrm{d}P_{D\setminus\gamma_1,z,\xi}\left(\gamma_2\right)\mathcal{O}\left[\gamma_2\right] \tag{5.35}$$

This means that LPP for conditioned curves and for curves in the cut domain must be the same.

We analysed the square lattice H by simulating curves and keeping only the ones that had $|\gamma_1| = L/4$ horizontal edges. The cut domain was realised as portrayed below
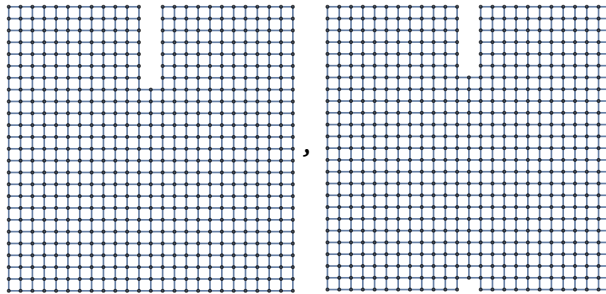
The analysis was performed for sizes L=8,$|\gamma_1| = 2$; L=16,$|\gamma_1| = 4$ and L=24,$|\gamma_1| = 6$. The average values were obtained over 17639 curves for $L = 8$, 2923 for $L = 16$ and 5390 for $L = 24$. In order to quantify the difference between the two distributions we defined
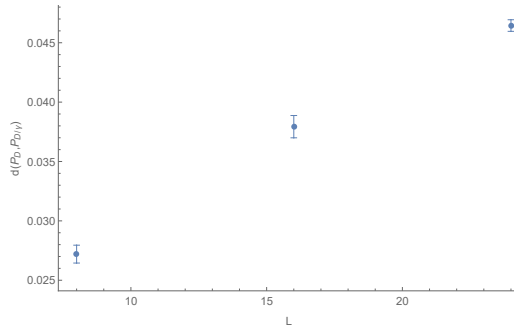
Figure 5.24: Distance between $P_D(\gamma_2|\gamma_1)$ and $P_{D/\gamma_1}(\gamma_2)$ for sizes L= 8,16,24. If fitted linearly, the dependence is given by $d(P_1, P_2) = 0.18(1) + 0.00120(8)L$
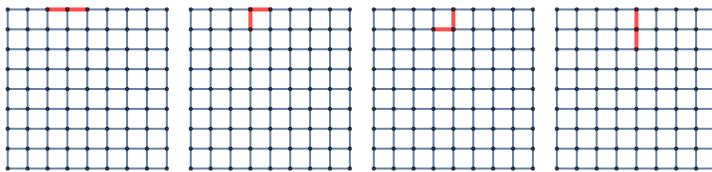

Figure 5.25: The order of the first 4 curves of length 2 (the remaining 3 are specular)

a distance between their two matrices of size $L \times L = N$.

$$d(A, B) = \sqrt{\sum_{i,j}^{L}(a_{ij} - b_{ij})^2/N}, \qquad (5.36)$$

Where a_{ij} (b_{ij}) is the number of times p the curve passes to the left of the point with coordinates (i, j), normalized to obtain $a_{ij} \in [-1, +1]$. The uncertainty was estimated as $\sqrt{p}$. The dependence of $d(P_D(\gamma_2|\gamma_1), P_{D/\gamma_1}(\gamma_2))$ from size L is shown in fig. 5.24 .

One may very well doubt about the typicality of the particular choice of γ_1. The divergence of the distance between probabilities may be an artefact of our conditioning on something increasingly less typical. Driven by such fear, we analysed the frequency with which paths of a given length appear. For instance, for a path of length 2 there are 7 possible realizations, as shown in fig.5.25.

The ordered histogram for sizes $L = 8, 16, 24$ is shown in fig. 5.26.

As we can see, the most frequent paths are the ones laying on the border, while the vertical path loses importance. If we take a large enough square, say of size $L = 24$, we can study the statistics of curves of length $|\gamma| = 4, 5$. As shown from histograms in fig. 5.27, the most frequent paths are still the ones that lay on the border, shown in a red circle (here the order is casual).

We then decided to condition the curve being as it's most frequently encountered, i.e. along the top border (see fig. 5.28). The same analysis for the distance between probabilities shows how in this case they still diverge and, in fact, the effect is even greater, as showed in fig. 5.29
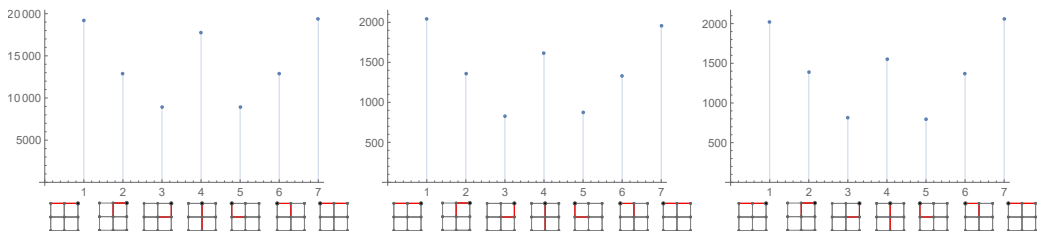
Figure 5.26: Histogram of the 7 paths ordered as in .5.25. For sizes $L = 8$ (left), $L = 16$ (centre) and $L = 16$ (right). The paths numbered 1 and 7 are the ones laying on the upper border (right and left sides), number 4 is the vertical one.
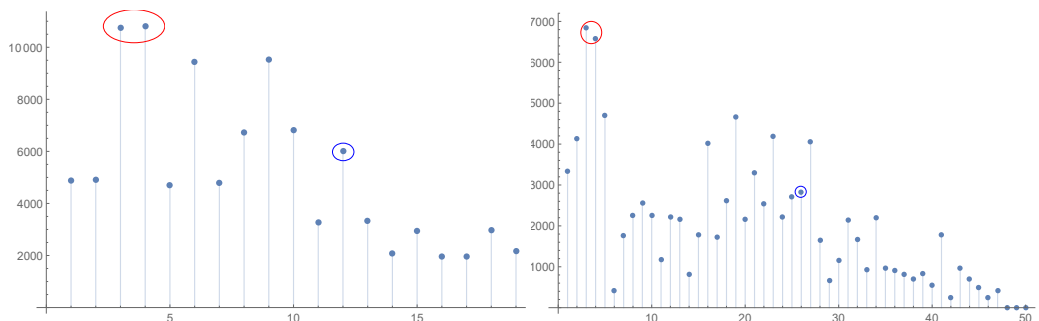

Figure 5.27: Paths of length 4 (left) and 5 (right) in a square of size $L = 24$. The paths laying on the border are shown in a red circle, the vertical path is shown in a blue circle. The order is casual.
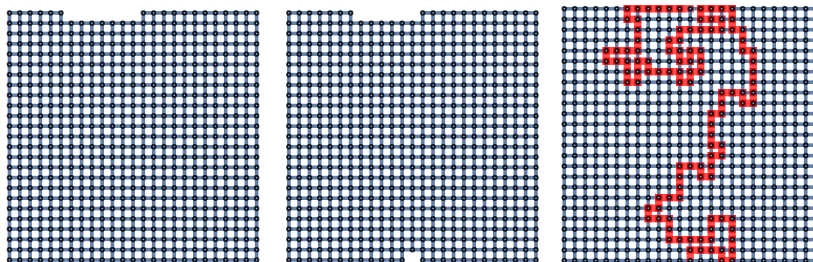

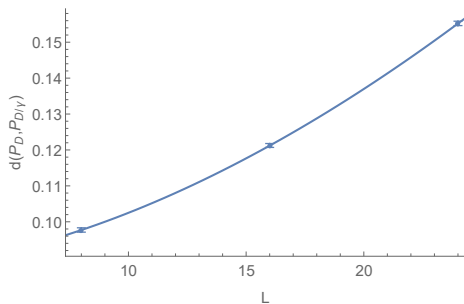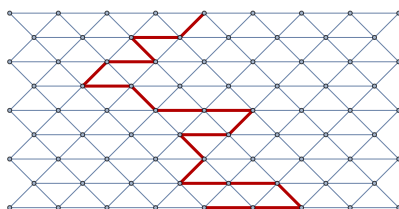**Figure 5.28:** An example of the cut domain and a generated curve in it

Figure 5.29: The distance $d(P_D(\gamma_2|\gamma_1), P_{D/\gamma_1}(\gamma_2))$ fitted with $x^{1.72}$

We performed the same analysis for a monopartite lattice, namely the triangular lattice.

We started analysing the frequency of first paths. In fig.5.30 it's showed the histogram for the first 4 steps of a curve in a square of size $L = 24$. The most frequent are once again the ones laying on the left and right top borders.
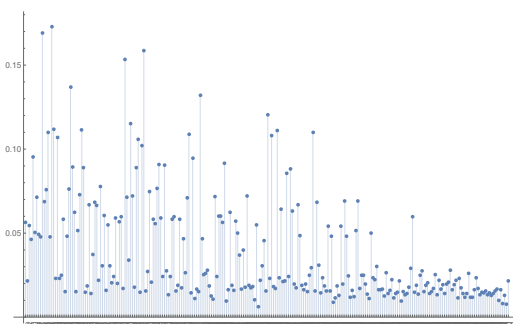

Figure 5.30: Histogram of the first paths of length 4 for a lattice of size $L = 24$

We then conditioned the curves to have the first $|\gamma_1| = L/4$ part on the border, obtaining $LPP_D(\gamma_2|\gamma_1)$. After that, we cut the same part from the domain as portrayed in fig.5.31, obtaining $LPP_{D/\gamma_1}(\gamma_2)$
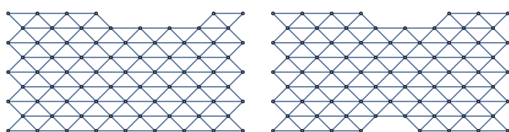

Figure 5.31: The lattices for $LPP_{D/\gamma_1}(\gamma_2)$

As well as before, we can see a difference between the two probabilities: $LPP_D(\gamma_2|\gamma_1) \neq LPP_{D/\gamma_1}(\gamma_2)$. If we obtain the distance 5.36 for sizes $L = 8, L = 16$, we can clearly see it does not tend to zero, as shown in fig 5.32

We conclude that the Domain Markov Property is certainly violated for these sizes of lattices ($L = 8, 16, 24$). Furthermore, the property does not seem to recover increasing the size (at this level). This indicates that most probably it will remain violated in the thermodynamic limit.
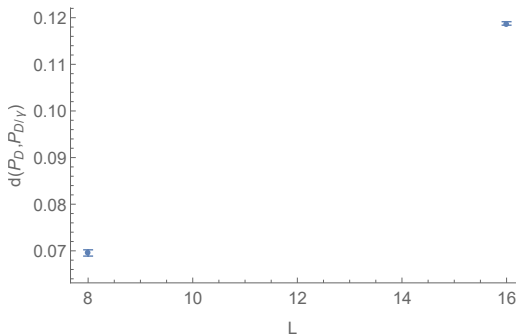
Figure 5.32: Distance between $P_D(\gamma_2|\gamma_1)$ and $P_{D/\gamma_1}(\gamma_2)$ on a triangular lattice for sizes L= 8, 16.

5.7.5   Driving function analysis

All the information we gathered led us towards the conclusion that the curve is influenced by the border too much to simulate its behaviour in the thermodynamic limit. The winding angle proved to be a really local variable, whereas left passage probability is influenced by long-range correlation.

To test the SLE hypothesis we decided to analyse the *driving function* by mapping the curve γ into the real axis at discretised steps, remembering that $\xi_{\Delta t} = g_{\Delta t}(\tau(\Delta t))$ must be normally distributed with variance $\langle \xi_{\Delta t}^2 \rangle = \kappa \Delta t$.

This analysis performed on the curves on the open square leads to discording results as the border is influencing the evolution of the curve. To minimise this effect, we decided to study contractible loops on the torus, performing the thermodynamic limit by considering only a small portion of the curve, after some considered manipulations inspired by Gherardi (2009).

First of all, we unfold the torus as shown in fig. 5.33 . Now that we have a loop on a plane, we brake and deform it in order to use SLE analysis for the chordal geometry. To break the loop and consider the new initial and final points independent, as created by the SLE evolution process in the upper half-plane, we will choose k steps and discard them. We carve a disk between two adjacent points, obtaining an open curve attached to two diametrically opposite points on a circumference. As shown in 5.34, by inversion and subsequent Möbius mapping we can map the curve to $\mathbb{H}$. The exact maps for each described step are

$$f = \sqrt{z+1}\sqrt{z-1} \tag{5.37}$$
$$g = 1/z \tag{5.38}$$
$$h = i\frac{1+z}{1-z} \tag{5.39}$$

$f(z)$ maps only the complement in $\mathbb{C}$ of the real segment $[-1, +1]$ to the complement in $\mathbb{C}$ of the unit disk, so our zeroth step is to rotate and translate each loop in order to have the two vertices of an edge in $(-1, 0)$ and $(+1, 0)$ and then we perform all the above steps. The discard of k points will be obtained simply by absorbing the first k steps into the real axis by conformal transformations once the curve in transformed.

We can now proceed to analyse the resulting curve with the so-called *Zipper algorithm*, the details of which are exposed in Appendix A and more thoroughly in Kennedy (2008); Marshall and Rohde (2007), to extract its driving function as depicted in fig. 5.35
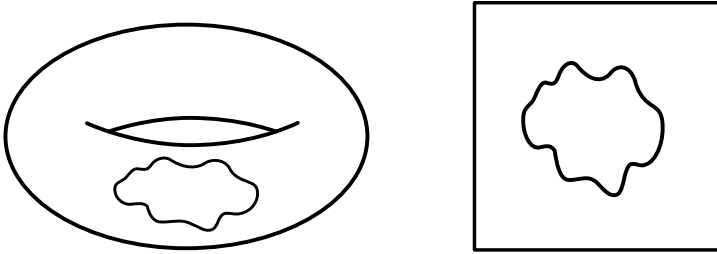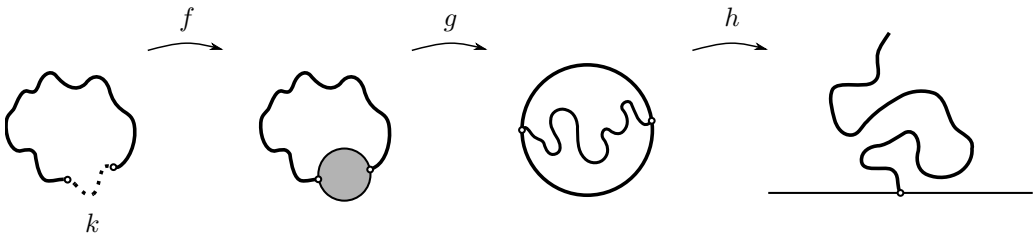
Figure 5.33: Unfolding the torus

Figure 5.34: All the steps used to map the loop to a curve in the upper half-plane $\mathbb{H}$. The picture is simplified since carving a disk with the initial k steps is operationally unwise because the rest of the curve may very well intersect it. To overcome this we actually carve a disk containing just one step and absorb into $\mathbb{H}$ the rest after all maps are performed.

We fix $k = 60, 90, 120$ and consider $L = 200, 400$. We condition the ensemble to $s > s_{min} = k + 10$ so as to ensure that $k < s$ and that there are at least a few points in the remaining curve. However, we did check, that the results do not depend appreciably on the particular choice of s_{min}. For each pair L, k we measure the $s - k$ pairs $(t_i, \xi_{t_i})_{i=0}^{s-k-1}$ as described above, for $\sim 10^5$ independent realizations. We first performed our analysis on the Q model. The leftmost panels in fig. 5.36 show the ensemble-averaged mean square displacement of ξ_t as a function of time. For small times, up to $t_{max} \simeq 0.012 \langle \xi_t^2 \rangle$, is approximately linear in t. While the time t_{max} does not seem to change appreciably with lattice size, the average number of steps needed to reach it, $\langle s(t_{max}) \rangle$, increases with L and k. Note that the quantity $\langle s(t_{max}) \rangle$ is computed without taking into consideration the first k steps of the original curve, which get mapped to the boundary of the domain. For $L = 200$ we find $\langle s(t_{max}) \rangle \simeq 110/157/188$ for $k = 60/90/120$ respectively. For $L = 400$ we find $\langle s(t_{max}) \rangle \simeq 174/268/325$. The ratios between $\langle s(t_{max}) \rangle$ and the average number of steps of the curves are $0.43, 0.49, 0.51$ for $L = 200$ (again for $k = 60, 90, 120$) and $0.46, 0.58, 0.61$ for $L = 400$. To compute κ we performed linear fits of $\langle \xi_t^2 \rangle$ versus t, using only the data at the larger size, $L = 400$. We performed fits in intervals $[0, t_{max}]$ with varying t_{max}. Fit results are shown in fig. 5.36.

Let us first focus on the square lattice. The fitted values for the square lattice stabilize around $t_{max} \simeq 0.01$. The three values of κ that we considered yield compatible estimates at the plateau. We estimate $\kappa = 2.07(8)$. Besides the scaling of the mean squared displacement, SLE predicts that the normalized process $\xi_t/\sqrt{t}$ is distributed normally with mean 0 and variance κ. To obtain sufficient statistics, we considered the data for $k = 60, 90, 120$ combined, and all times from $t_{min} = 0.001$ and $t_{max} = 0.012$ (for smaller values of t_{min} lattice artefacts become apparent, affecting the tails of the distribution). Fig. 5.36 shows that the normalised process is approximately Gaussian as expected. The

small discrepancies, especially apparent in linear scale for $L = 200$, are reduced by increasing the size. Repeating the same procedure for the T model we obtain $\kappa = 2.16(13)$, see also fig. 5.37. However, notice that, in the T model, the three values of κ give slightly inconsistent estimates, see fig. 5.38 .The values for $k = 60$ do not reach a well-defined plateau. Excluding them from the overall estimate, we get $\kappa = 2.20(8)$.

All the above results are in perfect agreement with the fractal dimension of the curves $D_f = 1 + k/8 \simeq 1.25/1.27$. We conclude that in the thermodynamic limit, curves generated by excitation of the Random Dimer Model, are critical, conformal and are described by SLE. We claim that the monopartite models are in the same universality class as 2d Edwards-Anderson spin glasses Melchert and Hartmann (2009); Wang et al. (2017); Corberi et al. (2019). Excitations produced in bipartite lattices, instead, are compatible with a loop-erased self-avoiding random walk process Majumdar (1992); Middleton (2000); 't Hooft and Veltman (1972).
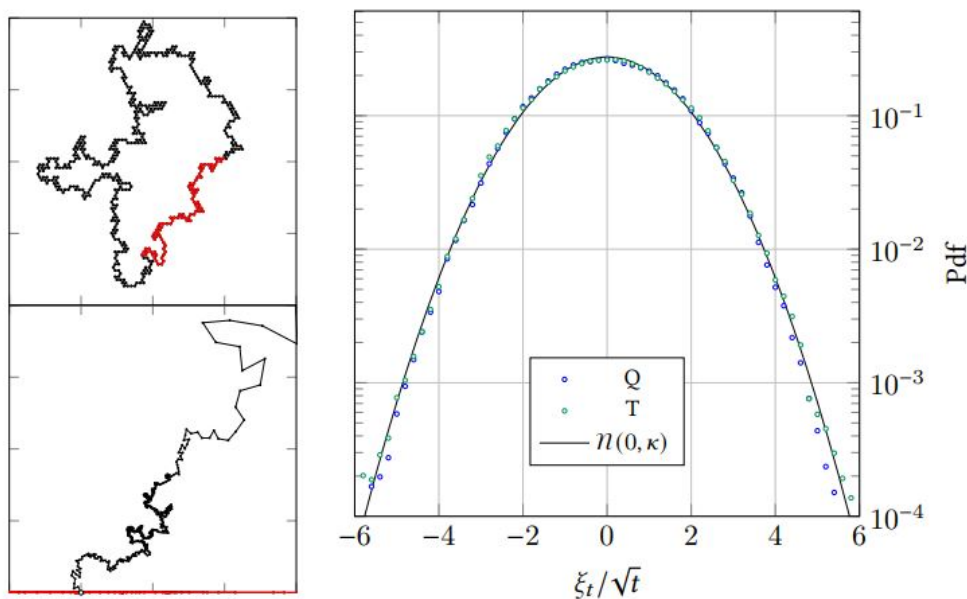

Figure 5.35: *Left*. A contractible loop with $s = 522$ in the T model with $L = 400$ (top) is split into two parts (red, of $k = 90$ steps, and black, of $s - k$ steps). By a conformal transformation, the black part is mapped into a curve in the upper half-plane stemming from the origin (bottom). *Right*. Probability distribution function of the driving function for $L = 400$ on the Q lattice and on the T lattice. The numerical results have been obtained averaging over a wide range of time t and are compared with a normal distribution $N(0, \kappa)$ having zero mean and variance $\kappa = 2.1$.
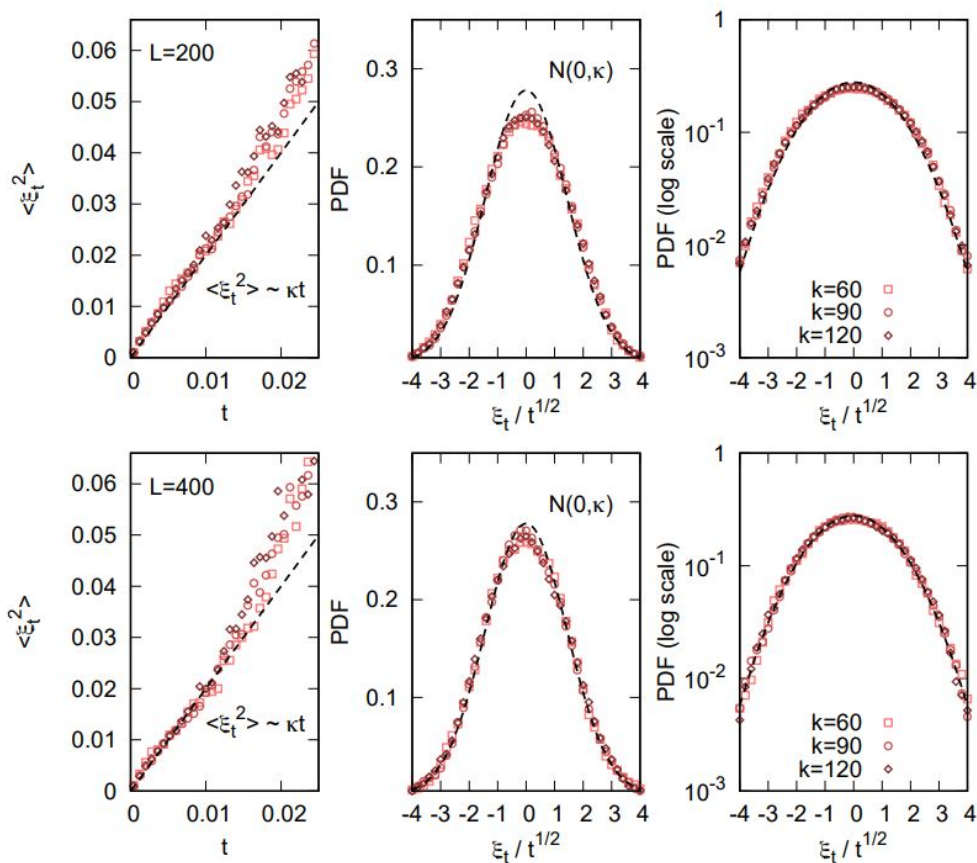
Figure 5.36: Driving function analysis on the Q model. Leftmost panels. Mean square displacement as a function of time, binned in intervals $\delta t = 0.0008$. The three symbols correspond to three values of k (the number of steps of the walks that get mapped to the boundary of $\mathbb{H}$): $k = 60$ (squares), $k = 90$ (circles), $k = 120$ (diamonds). Dashed lines are the SLE prediction for $\kappa = 2.07$. Central and rightmost panels. Empirical probability distribution function of the rescaled process $\xi_t / \sqrt{\kappa t}$ in linear and logarithmic scale (center and right, respectively) for times in range $0.001 < t < 0.012$. Dashed lines are the SLE prediction for $\kappa = 2.07$, i.e., Gaussian distributions with mean 0 and variance κ.
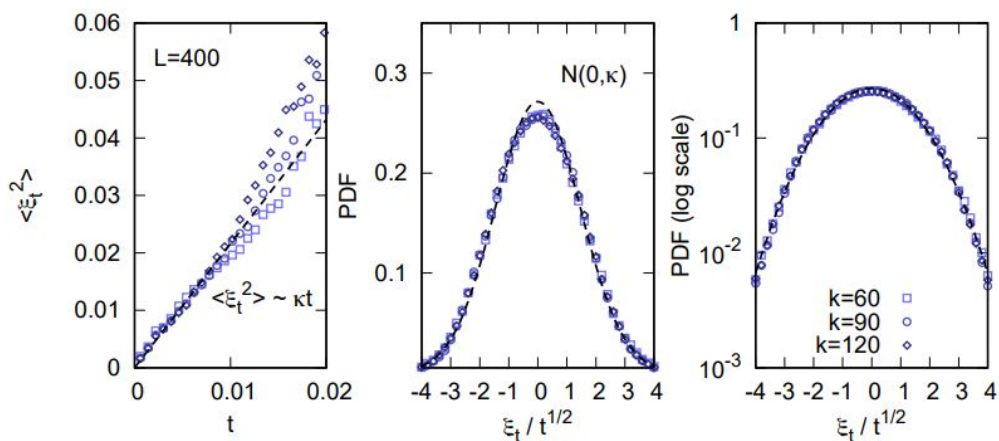
Figure 5.37: Driving function analysis of the T model. Leftmost panels. Mean square displacement as a function of time, binned in intervals $\delta t = 0.0008$. The three symbols correspond to three values of k (the number of steps of the walks that get mapped to the boundary of $\mathbb{H}$): $k = 60$ (squares), $k = 90$ (circles), $k = 120$ (diamonds). Dashed lines are the SLE prediction for $\kappa = 2.07$. Central and rightmost panels. Empirical probability distribution function of the rescaled process $\xi_t / \sqrt{\kappa t}$ in linear and logarithmic scale (center and right, respectively) for times in range $0.001 < t < 0.012$. Dashed lines are the SLE prediction for $\kappa = 2.16$, i.e., Gaussian distributions with mean 0 and variance κ
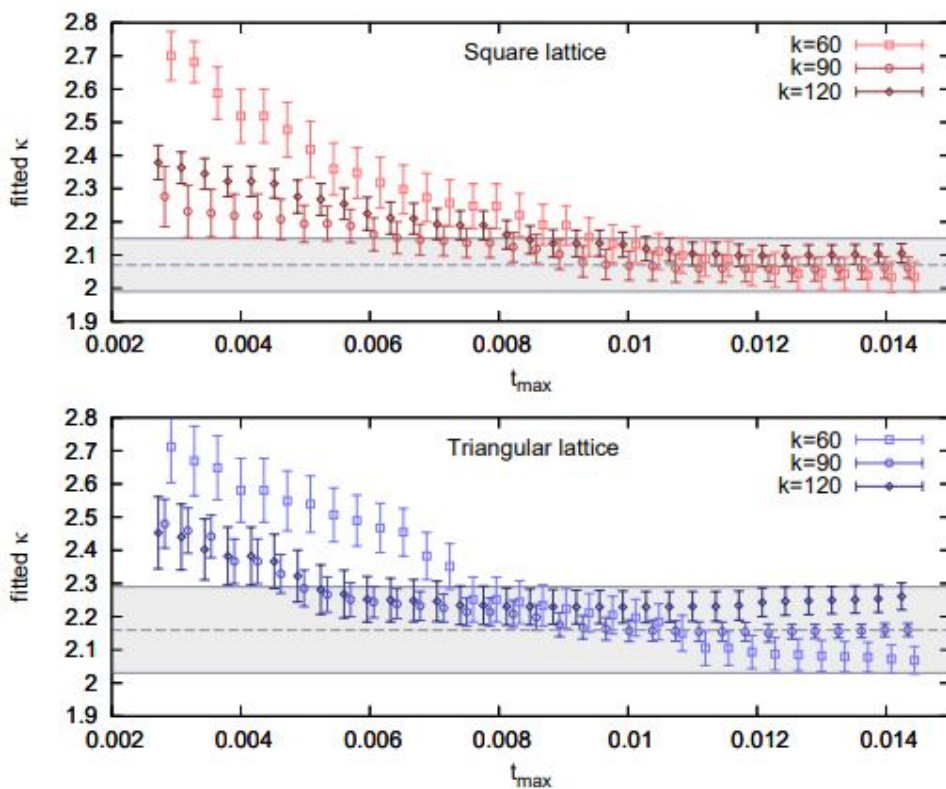
Figure 5.38: Fitted values of κ from simulations on the square lattice (top) and triangular lattice (bottom) as functions of the upper cutoff t_{max}. The three symbols refer to the three values of κ considered. Shaded bands indicate our final estimates (dashed line) and their variability.

5.8 Summary

Rigorously proving that a discrete system exhibits critical behaviour in the thermodynamic limit is no easy task. When the system is imbued with quenched disorder, this task becomes even harder. As of today, there is no rigorous proof that a single disordered system exhibits SLE-compatible excitations. This thesis, albeit not providing any such proof, analyses numerically and extensively shows under which conditions such behaviour can be observed in a system with quenched disorder, namely the *Random Dimer Model*.

It is shown that topological modification of a lattice induces, in the ground state of RDMs, excitations in the form of fractal curves which are compatible with excitations of a critical system, namely their correlation length diverges and observables behave like power-laws. By numerically evaluating critical exponents, we are able to determine the universality class of various RDM. As it turns out, the latter depends on the topology of the graph. Bipartite graphs exhibit exponents compatible with loop-erased random walks, in particular, the fractal dimension of curves in both models is $D_\mathrm{f} = 1.250(3)$. Non-bipartite graphs are compatible with the Edwards-Anderson Ising model and the fractal dimension of curves is compatible with the dimension of domain walls of the EA at zero temperature, namely $D_\mathrm{f} = 1.272(2)$.

In addition to this, our work inquires the possibility of a conformal description of said curves at the thermodynamic limit. As it is known, conformal curves generated by a random process can be described by SLE. The winding angle ϑ of excitation curves was numerically evaluated to behave as in the case of conformal curves: $\langle \vartheta^2 \rangle \sim \frac{D_\mathrm{f}-1}{2} \log L$ just as predicted, for instance, by the Coulomb gas method. Furthermore, another important observable is studied: the Left Passage Probability, for which SLE predicts a peculiar behaviour. Our study shows how this observable is affected by border conditions and thus can yield misleading values even at sizes for which other observables behave as in the thermodynamic limit. Namely, we show how the LPP of curves on the open square does not behave as expected, though it is compatible with some different SLE (mostly with $\kappa = 4$). Moreover, we show that in the open square, even Domain Markov Property seems violated, thus preventing any form of LPP analysis. Nonetheless, we overcome these difficulties by recreating the thermodynamic limit considering short portions of curves on the torus. We were able to conformally map such portions to the complex half-plane $\mathbb{H}$ and subsequently absorb them into the real axis by other conformal mappings. In this way, we extracted information about the driving function of the possible SLE, showing that it is indeed a Brownian walk with Normally distributed steps around the mean value $\kappa = \frac{D_\mathrm{f}-1}{2}$ for each model.

The accordance of κ, ϑ and D_f strongly suggests that the RDM at zero temperature is critical, conformal and SLE-compatible, a result that casts light on the yet vastly unexplored question of conformal behaviour for disordered models at critical temperature in the thermodynamic limit.

Appendices

The Zipper algorithm

A.1 Conformal mapping algorithms

Conformal maps have useful applications in mathematics, physics and engineering, aiding in the solution of problems from electrostatics to fluid dynamics Schinzinger and Laura (2012). Although it's a well-known fact that any two compact subsets of $\mathbb{C}$ can be mapped conformally into each other, there is no general procedure to find such mapping. This problem affects us since we would like to map the upper half-plane $\mathbb{H}$ into the complicated region drawn by the Schramm-Loewner evolution of a curve and vice-versa, in order to extract information about the Brownian motion of $\xi(t)$ in

$$\frac{\partial g_t(z)}{\partial t} = \frac{2}{g_t(z) - \xi(t)}. \tag{A.1}$$

Approximating the curve by a series of straight segments as we saw in chapter 3, is surely a first step towards a general algorithm. In the early 1980s, Kühnau and Marshall proposed a fast and accurate algorithm for finding both the conformal map and it inverse, that can be viewed as a discretisation of the Loewner differential equation. Here we aim to briefly introduce the argument, for a more detailed explanation the reader is invited to consult Marshall and Rohde (2007); Kennedy (2008) .

A.1.1 The Geodesic algorithm

The most elementary version of the conformal mapping algorithms is based on the subdivision of the curve in subsequent arcs perpendicular to $\mathbb{R}$ at 0. Each arc will be mapped to $\mathbb{R}$ by $f_a : \mathbb{H}/\gamma \to \mathbb{H}$, as shown in fig. A.1. This can be done by the composition of a linear fractional transformation, the square and the square root map as in fig A.1. The orthogonal circle also meets $\mathbb{R}$ orthogonally at point $b = |a|^2/\mathrm{Re}a$, whereas $c = |a|^2/\mathrm{Im}a$. The inverse f_a^{-1} can be easily found by composing the inverses of these elementary maps in the reverse order.

A.1.2 The Slit algorithm

We can improve the previous approximation by using straight lines instead of orthogonal arcs. In this case, instead of having the previous f_a^{-1}, we will have the maps $g_a : \mathbb{H} \to \mathbb{H}/L$, where L is a segment from 0 to a, as shown in fig. A.2. The mapping is

$$g_a(z) = C(z - p)^p(z + 1 - p)^{1-p}, \tag{A.2}$$

where $p = \arg a/\pi$ and $C = |a|/p^p(1 - p)^{1-p}$. As in the maps of the geodesic algorithm,
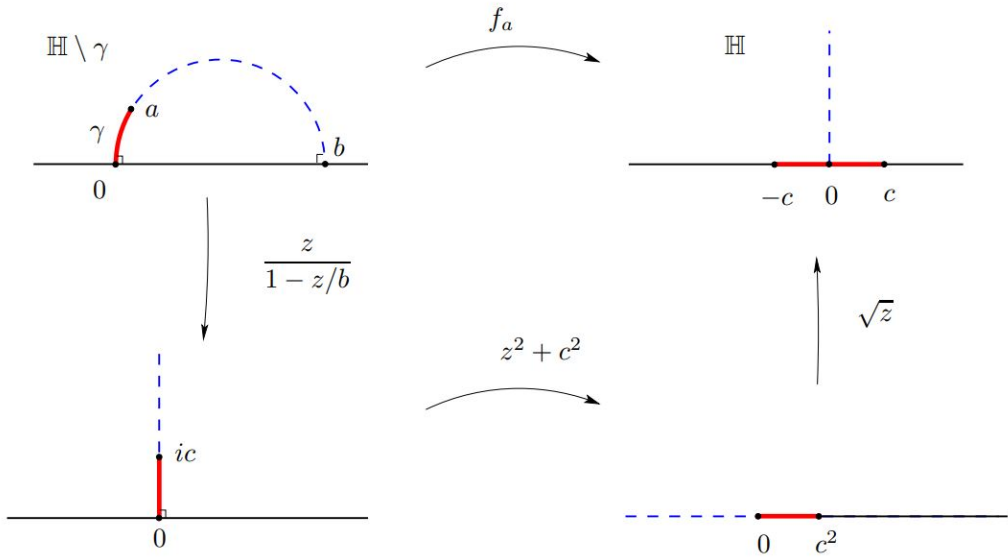
Figure A.1: The geodesic algorithm mapping. f_a is the composition of a linear fractional transformation, the square and the square root map. $b = |a|^2/\mathrm{Re}\,a$, $c = |a|^2/\mathrm{Im}\,a$.
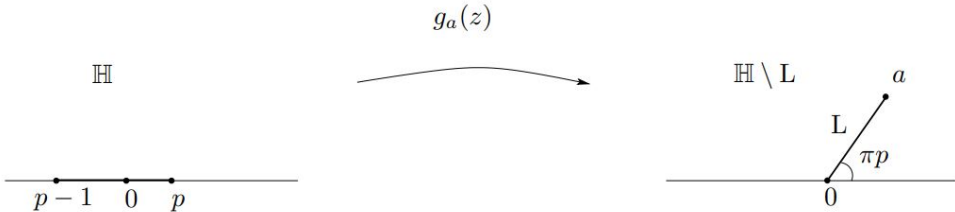

Figure A.2: The Slit algorithm. g_a maps the segment $[p-1, p] \in \mathbb{R}$ to the oblique slit L.

the line segment from 0 to a is opened to two adjacent intervals on $\mathbb{R}$ by $f_a = g_a^{-1}$ with $f_a(a) = 0$ and $f_a(\infty) = \infty$. The new map f_a cannot be written in terms of elementary functions, but can quickly be found by iterations using Newton's method, as described in Marshall and Rohde (2007).

A.1.3   The Zipper algorithm

Since our curves are constructed on lattices and are thus composed of straight segments, the Slit algorithm is the natural best choice to perform the conformal mappings.

However, a last improvement for smooth curves was devised and bears the name Zipper algorithm. We can further improve the approximation by replacing the linear slits with arcs of (nonorthogonal) circles. By a linear fractional transformation l_a this arc is mapped to a line segment (assuming the arc is not tangent to $\mathbb{R}$ at 0), as shown in fig. A.3.

The complement of this segment in $\mathbb{H}$ can then be mapped to $\mathbb{H}$ as described in the slit algorithm, using g_d^{-1}, where $d = a/(1 - a/b)$. Thus, as the authors say, at each stage we
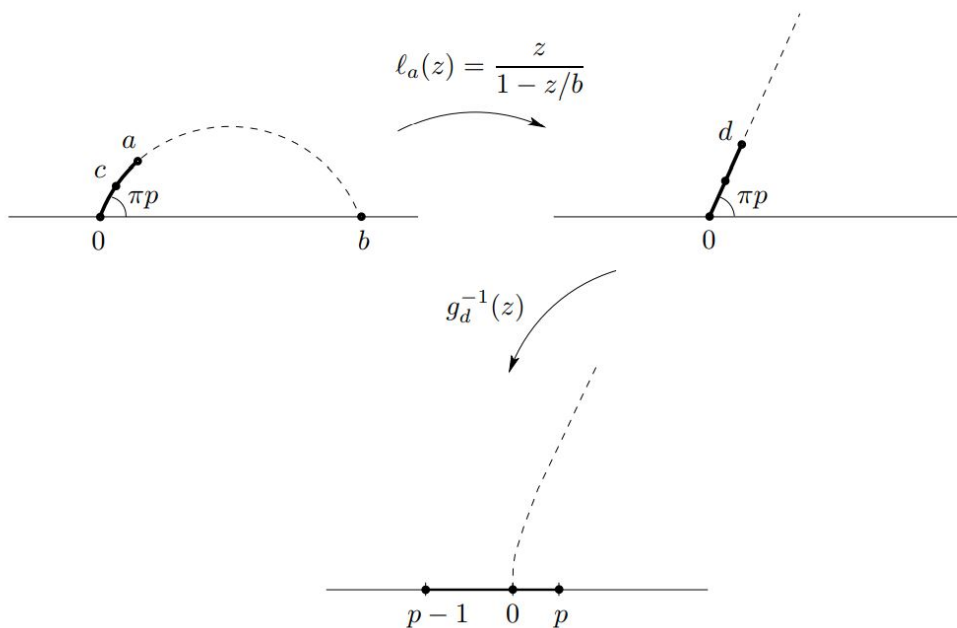
$$\ell_a(z) = \frac{z}{1 - z/b}$$

Figure A.3: The Zipper algorithm. $l_a \circ g_d^{-1}$ maps the arc $[0, a]$ to the segment $[p - 1, p] \in \mathbb{R}$.

are giving a "quadratic approximation" instead of a linear approximation to the (image of) the boundary.

Whichever is our choice of approximation, after mapping the n portions of the curve to the real axis by the composition

$$\phi = \phi_n \circ \phi_{n-1} \circ \phi_{n-2} \cdots \circ \phi_2 \circ \phi_1, \tag{A.3}$$

we can recover statistics for the points p, which ought to be normally distributed with variance κ if the process is a Schramm-Loewner evolution.

Edmond's Blossom algorithm

B.1   Perfect matchings on graphs

When presented a graph G(V,E), consisting of a set of vertices V connected by edges E, the task of finding a perfect matching in not a quickly solvable one. By matching vertices to random adjacent ones, one can easily incur in lone vertices that can not be matched since all the adjacent are taken by one's previous random matching. Intuitively, such a search may require a complete enumeration of all the possible subgraphs, thus rendering the problem intractable. Luckily, in 1961 Jack Edmonds developed an algorithm capable of solving the task in polynomial time $O\left(|E||V|^2\right)$, where $|E|$ is the number of edges, and $|V|$ is the number of vertices Edmonds (1965b).

The core idea is that a matching M should be found by starting from a minimal matching of two vertices and augmenting the "matched subset" adding vertices and modifying matching edges, following a set of rules that prevents the inconvenient scenario of obtaining an isolated unmatchable vertex. In this way, no extensive enumeration is required, since the final matching is found by growth.

The algorithm, following the botanic naming tradition, was called by Edmonds "Paths, trees and flowers" and today is known as Edmond's *Blossom algorithm*. In it, a fundamental role is found in the contraction of odd cycles called blossoms, hence the name.
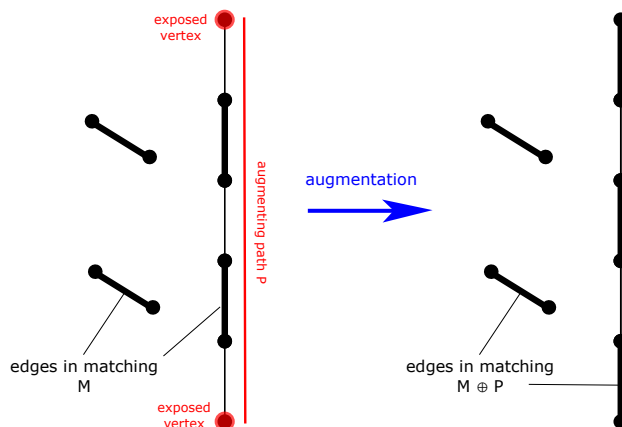

Figure B.1: An example of augmenting path. Courtesy of Wikipedia

The basic idea, as said, is to start with a randomly chosen matching M and find an *augmentation path* P, which starts and ends with two unmatched vertices. This way,
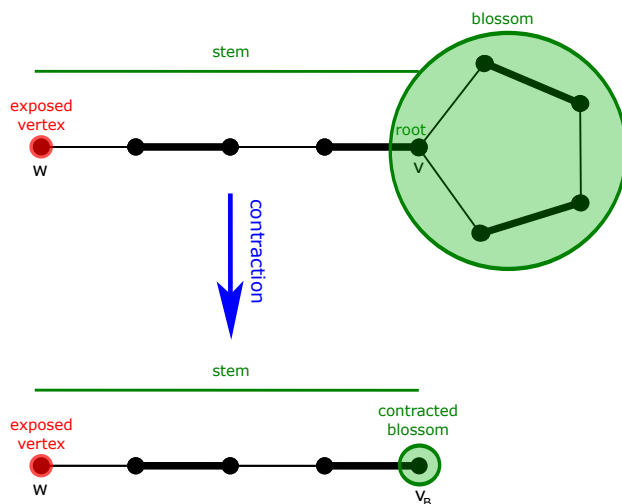
Figure B.2: The contracting of a blossom. Courtesy of Wikipedia

the initial matching M can be augmented by the inclusion of the new vertices and a subsequent rearrangement of the edges in M⊕P, as shown in fig. B.1. In the simplest scenario, this can be enough to find the perfect matching. However, the augmentation path P is not always so trivially constructed. Starting from an unmatched vertex, the algorithm will explore along the graph, until it reaches another unmatched vertex in order to perform the augmentation. The biggest enemy of such a blind exploration, are loops. Nonetheless, by alternating numeration along the explored edges, we are able to spot contractible cycles of length $2k + 1$ and deal with them simply by contracting them as shown in fig. B.2.

In this way, despite the fast blind search for an augmentation path, we will end up with an augmentation path as in fig. B.1.

Now, since we are dealing with weighted graphs and our desire is to find the optimal dimer cover, i.e. the matching with minimal (maximal) total weight, we also need a polynomial-time algorithm for this last search. Luckily, Edmond also solved this problem. Instead of obtaining and then comparing all matchings, one can augment paths in such a way, that the new matching is always optimal and therefore the minimal-weighted matching is constructed.

In order to find which edges can be used to augment paths, the algorithm solves a constrained minimum problem for a vector x_e:

$$\sum_{e \in \delta(u)} x_e = 1 \quad , \forall u \in V \tag{B.1a}$$

$$\sum_{e \in \gamma(B)} x_e \geq 0 \quad , \forall B \in \mathcal{O} \tag{B.1b}$$

$$x_e \geq 0 \quad , \vee e \in E \tag{B.1c}$$

where $\delta(X)$ is the set of edges incident to a vertex in X, $\gamma(X)$ is the set of edges with both endpoints in X and $\mathcal{O}$ is the set of odd cardinality subsets of the nodes. In *Linear Programming* a theorem states that for any constrained-minimum problem, there is a *dual problem* in which dual variables are maximised. In our case, the algorithm solves both the

original and the dual problem to find so-called *tight edges*, for which the original weight w_e is equal to the newly found dual.

The optimal solution will be a solution of both the original and the dual problem, by assuring that paths are augmented only via tight edges, at the end one obtains a perfect matching which satisfies the constrained maximum problem, and thus, is the minimal.

More on the subject and also a nice review of the algorithm's speed evolution through the years can be found in Cook and Rohe (1999).

Bibliography

Amoruso, C., Hartmann, A. K., Hastings, M. B., and Moore, M. A. (2006). Conformal invariance and stochastic loewner evolution processes in two-dimensional ising spin glasses. *Phys. Rev. Lett.*, 97:267202.

Andrews, T. (1869). The bakerian lecture.—on the continuity of the gaseous and liquid states of the gaseous and liquid states of matter.

Barahona, F. (1982). On the computational complexity of ising spin glass models. *Journal of Physics A: Mathematical and General*, 15(10):3241.

Bauer, M. and Bernard, D. (2006). 2d growth processes: Sle and loewner chains. *Physics reports*, 432(3-4):115–221.

Bieche, L., Uhry, J., Maynard, R., and Rammal, R. (1980). On the ground states of the frustration model of a spin glass by a matching method of graph theory. *Journal of Physics A: Mathematical and General*, 13(8):2553.

Bogachev, V. I. and Kolesnikov, A. V. (2012). The monge-kantorovich problem: achievements, connections, and perspectives. *Russian Mathematical Surveys*, 67(5):785.

Bray, A. and Moore, M. (1984). Lower critical dimension of ising spin glasses: a numerical study. *Journal of Physics C: Solid State Physics*, 17(18):L463.

Caracciolo, S., D'Achille, M., and Sicuro, G. (2017). Random euclidean matching problems in one dimension. *Physical Review E*, 96(4):042102.

Caracciolo, S., Edwards, R. G., Ferreira, S. J., Pelissetto, A., and Sokal, A. D. (1995). Extrapolating monte carlo simulations to infinite volume: Finite-size scaling at $\xi/l \gg 1$. *Phys. Rev. Lett.*, 74:2969–2972.

Caracciolo, S., Fabbricatore, R., Gherardi, M., Marino, R., Parisi, G., and Sicuro, G. (2020). Criticality and conformality in the random dimer model. *arXiv preprint arXiv:2012.13956*.

Caracciolo, S., Lucibello, C., Parisi, G., and Sicuro, G. (2014). Scaling hypothesis for the euclidean bipartite matching problem. *Physical Review E*, 90(1):012118.

Caracciolo, S. and Sicuro, G. (2015a). Quadratic stochastic euclidean bipartite matching problem. *Physical review letters*, 115(23):230601.

Caracciolo, S. and Sicuro, G. (2015b). Scaling hypothesis for the euclidean bipartite matching problem. ii. correlation functions. *Physical Review E*, 91(6):062125.

Cardy, J. (2005). Sle for theoretical physicists. *Annals of Physics*, 318(1):81–118.

Cardy, J. (2006). Lectures on stochastic loewner evolution and other growth processes in two dimensions. *Lectures given at the school on Non-Equilibrium Dynamics of Interacting Particle Systems*.

Chelkak, D. and Smirnov, S. (2012). Universality in the 2d ising model and conformal invariance of fermionic observables. *Inventiones mathematicae*, 189(3):515–580.

Chertkov, M., Kroc, L., Krzakala, F., Vergassola, M., and Zdeborová, L. (2010). Inference in particle tracking experiments by passing messages between images. *Proc. Natl. Acad. Sci.*, 107(17):7663–7668.

Cook, W. and Rohe, A. (1999). Computing Minimum-Weight Perfect Matchings. *Informs Journal on Computing*, 11(2):138–148.

Corberi, F., Cugliandolo, L. F., Insalata, F., and Picco, M. (2019). Fractal character of the phase ordering kinetics of a diluted ferromagnet. *Journal of Statistical Mechanics: Theory and Experiment*, 2019(4):043203.

Curie, P. (1895). Magnetic properties of materials at various temperatures. *Ann. Chim. Phys.*, 5:289–405.

Dezsö, B., Jüttner, A., and Kovács, P. (2011). LEMON – an Open Source C++ Graph Template Library. *Electron. Notes Theor. Comput. Sci*, 264(5):23–45.

Di Francesco, P., Mathieu, P., and Senechal, D. (1997). *Conformal Field Theory*. Graduate Texts in Contemporary Physics. Springer-Verlag, New York.

Duplantier, B. and Binder, I. A. (2002). Harmonic measure and winding of conformally invariant curves. *Phys. Rev. Lett.*, 89(26):264101.

Duplantier, B. and Saleur, H. (1988). Winding-angle distributions of two-dimensional self-avoiding walks from conformal invariance. *Phys. Rev. Lett.*, 60(23):2343.

Edmonds, J. (1965a). Maximum Matching and a Polyhedron with 0,1-Vertices. *Journal of Research of the National Bureau of Standards*, (69B):125–130.

Edmonds, J. (1965b). Paths, Trees and Flowers. *Canadian Journal of Mathematics*, (17):449—-467.

Edmonds, J. and Karp, R. M. (1972). Theoretical improvements in algorithmic efficiency for network flow problems. *ACM*, 19(2):248–264.

Edwards, S. F. and Anderson, P. W. (1975). Theory of spin glasses. *Journal of Physics F: Metal Physics*, 5(5):965.

Einstein, A. (1910). The theory of the opalescence of homogeneous fluids and liquid mixtures near the critical state. *Annalen der Physik*, 33:1275—-1298.

Fisher, M. E. (1966). On the dimer solution of planar ising models. *Journal of Mathematical Physics*, 7(10):1776–1781.

Fisher, M. E. (1983). Scaling, universality and renormalization group theory. pages 1–139.

Gherardi, M. (2009). *Conformal walks in two dimensions*. Phd, Università di Milano.

Hartmann, A. K. and Young, A. (2001). Lower critical dimension of ising spin glasses. *Physical Review B*, 64(18):180404.

Henkel, M. (1999). *Conformal invariance and critical phenomena*.

Kager, W. and Nienhuis, B. (2004). A guide to stochastic löwner evolution and its applications. *Journal of statistical physics*, 115(5-6):1149–1229.

Kasteleyn, P. (1967). Graph theory and crystal physics. *Graph theory and theoretical physics*, pages 43–110.

Kasteleyn, P. W. (1961). The statistics of dimers on a lattice: I. the number of dimer arrangements on a quadratic lattice. *Physica*, 27(12):1209–1225.

Kasteleyn, P. W. (1963). Dimer statistics and phase transitions. *Journal of Mathematical Physics*, 4(2):287–293.

Kennedy, T. (2008). Computing the loewner driving process of random curves in the half plane. *Journal of Statistical Physics*, 131(5):803–819.

Kenyon, R. (2009). Lectures on dimers. *arXiv preprint arXiv:0910.3129*.

Kenyon, R. (2014). Conformal invariance of loops in the double-dimer model. *Communications in Mathematical Physics*, 326(2):477–497.

Kenyon, R. and Wilson, D. (2011). Boundary partitions in trees and dimers. *Transactions of the American Mathematical Society*, 363(3):1325–1364.

Kimchi, I., Nahum, A., and Senthil, T. (2018). Valence bonds in random quantum magnets: theory and application to ybmggao 4. *Physical Review X*, 8(3):031028.

Kivelson, S. A., Rokhsar, D. S., and Sethna, J. P. (1987). Topology of the resonating valence-bond state: Solitons and high-t c superconductivity. *Physical Review B*, 35(16):8865.

Landau, L. D., Lifshitz, E. M., and Pitaevskii, L. (1980). *Statistical physics: theory of the condensed state*, volume 9. Butterworth-Heinemann.

Lawler, G. F., Schramm, O., and Werner, W. (2011). Conformal invariance of planar loop-erased random walks and uniform spanning trees. In *Selected Works of Oded Schramm*, pages 931–987. Springer.

Lovász, L. and Plummer, D. (2009). *Matching Theory*. AMS Chelsea Publishing Series.

Lucibello, C., Parisi, G., and Sicuro, G. (2017). One-loop diagrams in the random euclidean matching problem. *Physical Review E*, 95(1):012302.

Majumdar, S. N. (1992). Exact fractal dimension of the loop-erased self-avoiding walk in two dimensions. *Phys. Rev. Lett.*, 68:2329–2331.

Marshall, D. E. and Rohde, S. (2007). Convergence of a variant of the zipper algorithm for conformal mapping. *SIAM Journal on Numerical Analysis*, 45(6):2577–2609.

Melchert, O. and Hartmann, A. (2009). Scaling behavior of domain walls at the t= 0 ferromagnet to spin-glass transition. *Physical Review B*, 79(18):184402.

Mézard, M. and Parisi, G. (1986). Mean-field equations for the matching and the travelling salesman problems. *EPL (Europhysics Letters)*, 2(12):913.

Mézard, M. and Parisi, G. (1988). The euclidean matching problem. *Journal de Physique*, 49(12):2019–2025.

Middleton, A. A. (2000). Disorder-induced topological defects in a $d = 2$ elastic medium at zero temperature. *Phys. Rev. B*, 61:14787–14790.

Moessner, R. and Sondhi, S. L. (2001). Resonating valence bond phase in the triangular lattice quantum dimer model. *Physical Review Letters*, 86(9):1881.

Peyré, G. and Cuturi, M. (2019). *Computational Optimal Transport: With Applications to Data Science*. Foundations and Trends in Machine Learning Series. Now Publishers.

Pfeuty, P. and Toulouse, G. (1976). *Introduction to the Renormalization Group and to Critical Phenomena*. John Wiley Sons.

Posé, N., Schrenk, K. J., Araújo, N. A., and Herrmann, H. J. (2014). Shortest path and schramm-loewner evolution. *Scientific reports*, 4(1):1–5.

Rohde, S. and Schramm, O. (2005). Basic properties of SLE. *Ann. Math.*, 161:883–924.

Santambrogio, F. (2015). *Optimal Transport for Applied Mathematicians: Calculus of Variations, PDEs, and Modeling*. Progress in Nonlinear Differential Equations and Their Applications. Springer International Publishing.

Schinzinger, R. and Laura, P. A. (2012). *Conformal mapping: methods and applications*. Courier Corporation.

Schramm, O. et al. (2001). A percolation formula. *Electronic Communications in Probability*, 6:115–120.

Schramm, O. and Sheffield, S. (2003). The harmonic explorer and its convergence to sle(4). *Annals Probab.*, 33:2127–2148.

Shirakura, T. and Matsubara, F. (1997). Low temperature phase of asymmetric spin glass

model in two dimensions. *Physical review letters*, 79(15):2887.

Smirnov, S. (2001). Critical percolation in the plane: conformal invariance, cardy's formula, scaling limits. *Comptes Rendus de l'Académie des Sciences-Series I-Mathematics*, 333(3):239–244.

Stanley, H. E. (1987). *Introduction to Phase Transitions and Critical Phenomena*. Oxford University Press.

't Hooft, G. and Veltman, M. (1972). Regularization and renormalization of gauge fields. *Nuclear Physics B*, 44:189–213.

Temperley, H. N. and Fisher, M. E. (1961). Dimer problem in statistical mechanics-an exact result. *Philosophical Magazine*, 6(68):1061–1063.

Uzunov, D. (1993). *Introduction to the theory of critical phenomena: Mean field, fluctuations and renormalization*.

van der Waals, J. (1873). *On the Continuity of the Gas and Liquid State*. PhD thesis.

Villani, C. (2008). *Optimal transport: old and new*, volume 338. Springer Science & Business Media.

Wang, W., Moore, M. A., and Katzgraber, H. G. (2017). Fractal dimension of interfaces in edwards-anderson and long-range ising spin glasses: Determining the applicability of different theoretical descriptions. *Phys. Rev. Lett.*, 119:100602.

Wieland, B. and Wilson, D. B. (2003). Winding angle variance of fortuin-kasteleyn contours. *Phys. Rev. E*, 68(5):056101.

Wilson, K. G. (1975). The renormalization group: critical phenomena and the Kondo problem. *Reviews of Modern Physics*, 47(4).

Zarinelli, E. (2008). *Statistical properties of the random 2-dimensional euclidean Grid-Poisson Marriage problem*. Master thesis, Università di Milano.

Zeng, C., Leath, P. L., and Fisher, D. S. (1999). Absence of two-dimensional bragg glasses. *Phys. Rev. Lett.*, 82:1935–1938.